

THE UNIVERSITY OF CHICAGO

SOLUTION AND SUBSTRATE ASSEMBLY OF NOBLE METAL NANOPARTICLES

A DISSERTATION SUBMITTED TO  
THE FACULTY OF THE DIVISION OF THE PHYSICAL SCIENCES  
IN CANDIDACY FOR THE DEGREE OF  
DOCTOR OF PHILOSOPHY

DEPARTMENT OF CHEMISTRY

BY

EDWARD W. MALACHOSKY

CHICAGO, ILLINOIS

MARCH 2017

Copyright © Edward W. Malachosky 2017

All rights reserved

# TABLE OF CONTENTS

LIST OF TABLES.....	vi
LIST OF FIGURES.....	vii
PREFACE.....	xiv
ABSTRACT.....	xvii
CHAPTER 1. INTRODUCTION.....	1
1.1 The Plasmon Phenomenon.....	3
1.2 Gold Nanorods and Gold Bipyrramids.....	7
CHAPTER 2. GOLD BIPYRAMID NANOPARTICLE DIMERS.....	9
2.1 Introduction.....	9
2.2 Experimental Methods.....	10
<i>Materials</i> .....	10
<i>Instrumentation</i> .....	11
<i>Gold Bipyrramid Nanoparticle Dimer Synthesis</i> .....	11
2.3 Results and Discussion.....	13
2.4 Conclusion.....	31
2.5 Post-Publication Notes.....	31
CHAPTER 3. END-TO-END ALIGNMENT OF GOLD NANORODS ON TOPOGRAPHICALLY ENHANCED, CYLINDER FORMING DIBLOCK COPOLYMER TEMPLATES AND THEIR SURFACE ENHANCED RAMAN SCATTERING PROPERTIES.....	33
3.1 Introduction.....	34

3.2 Experimental Methods.....	36
3.3 Results and Discussion.....	40
3.4 Conclusion.....	49
3.5 Post-Publication Notes.....	51
 CHAPTER 4. SURFACE MORPHOLOGY DEVELOPMENT IN DIBLOCK COPOLYMER THIN FILMS THROUGH SEQUENTIAL SOLVENT EXPOSURE.....	
4.1 Introduction.....	52
4.2 Experimental Methods.....	54
<i>New Materials</i> .....	54
<i>New Instrumentation</i> .....	54
<i>New Methods</i> .....	54
4.3 Results and Discussion.....	57
<i>Morphology Development</i> .....	57
<i>THF Effect</i> .....	63
<i>Selective Solvent Effect</i> .....	76
<i>Gold Nanoparticle Alignment</i> .....	82
4.4 Conclusion.....	83
4.5 Pertinent Background Results.....	86
 CHAPTER 5. ON-GOING PROJECTS.....	
5.1 Polymer Templated Gold-Bipyramid – Silver Nanosphere Heterostructures with Large Second Harmonic Generation Response.....	90
5.1.1 <i>Experimental Methods</i> .....	91
New Materials.....	91

New Methods.....	91
5.1.2 <i>Nanoparticle Synthesis Considerations</i> .....	93
5.1.3 <i>Dark Field Optical Characterization</i> .....	99
5.1.4 <i>Second Harmonic Generation</i> .....	100
5.1.5 <i>Conclusion</i> .....	102
5.2 Gold Bipyramid – Quantum Dot Heterostructures with Enhanced Photoluminescence Properties.....	103
5.2.1 <i>Experimental Methods</i> .....	105
New Materials.....	105
New Instrumentation.....	107
New Methods.....	107
5.2.2 <i>Synthetic Considerations</i> .....	113
5.2.3 <i>AuBP – QD Hybrids with Polymer Protected AuBPs and DNA</i> .....	116
5.2.4 <i>Liquid Cell AuBP – QD Systems for Enhanced Fluorescence Investigations</i> .....	117
5.2.5 <i>Amide Bond Based AuBP – QD Hybrid Systems</i> .....	119
5.2.6 <i>Conclusion</i> .....	120
CHAPTER 6. COLLABORATIONS.....	123
6.1 Viscoelastic Flows in Simple Liquids Generated by Vibrating Nanostructures.....	123
6.2 Scalable Ligand-Mediated Transport Synthesis of Perovskite Nanocrystals with Resolved Ultrafast Intraband Relaxation and Exciton Coherences.....	125
CHAPTER 7. CONCLUSION AND OUTLOOK.....	128
REFERENCES.....	132

# LIST OF TABLES

<b>Table 2.3.1</b> Complete gold bipyramid dimer aliquot particle count.....	21
<b>Table 2.3.2</b> Gold bipyramid dimer type analysis.....	22
<b>Table 2.3.3</b> Gold bipyramid dimer dark field and UV/Vis spectral matching .....	28
<b>Table 4.3.1</b> Analysis of Figure 4.3.1 film topographies.....	58
<b>Table 4.3.2</b> Analysis of Figure 4.3.5 mushroom topographies.....	60
<b>Table 4.3.3</b> Analysis of Figure 4.3.5 cylinder topographies.....	62
<b>Table 4.3.4</b> Flory-Huggins interaction parameters for diblock copolymer domains with the solvents used in chapter 4.....	74
<b>Table 4.3.5</b> pH and pKa values of materials used in chapter 4.....	75

# LIST OF FIGURES

<b>Figure 1.1.1</b> UV/Vis spectra, TEM images, and theoretical electromagnetic field enhancements of anisotropic gold nanoparticles.....	7
<b>Figure 2.2.1</b> Home-built dark-field microscope.....	12
<b>Figure 2.2.2</b> Characteristic gold bipyramid UV/Vis spectrum and TEM image.....	13
<b>Figure 2.2.3</b> UV/Vis spectra demonstrating gold bipyramid dimer reaction solution stability without linker molecule.....	14
<b>Figure 2.3.1</b> Gold bipyramid dimer reaction UV/Vis spectra demonstrating early irreproducibility.....	15
<b>Figure 2.3.2</b> Glutathione linking agent gold bipyramid dimer reaction UV/Vis spectra demonstrating stabilization solution effect.....	16
<b>Figure 2.3.3</b> Gold bipyramid dimer reaction UV/Vis spectra comparing glutathione and cysteine as linking agents, and demonstrating stabilization solution effect.....	17
<b>Figure 2.3.4</b> UV/Vis spectra comparing different thiol molecule linking agents.....	19
<b>Figure 2.3.5</b> Gold bipyramid bowtie structure analyses.....	22
<b>Figure 2.3.6</b> Gold bipyramid longitudinal edge-edge and V-shape structure analyses.....	23
<b>Figure 2.3.7</b> Outline of the dark field and SEM optical and structure matching process.....	24
<b>Figure 2.3.8</b> Gold bipyramid dimer polarization dependence and full-width half-maxima.....	25
<b>Figure 2.3.9</b> Gold bipyramid dimer TEM images demonstrating tip overlap effects.....	25
<b>Figure 2.3.10</b> Comparison of gold bipyramid dimer resonances as a function of center-to-center spacing.....	26
<b>Figure 2.3.11</b> Gold bipyramid dimer UV/Vis reaction solution peak fitting explanation.....	28

<b>Figure 2.3.12</b> Gold bipyramid dimer solution UV/Vis and dark field peak matching, dimer reaction kinetics, and cartoon demonstration of the kinetics explanation in the text.....	28
<b>Figure 2.3.13</b> Gold bipyramid dimer reaction kinetic fits.....	30
<b>Figure 2.5.1</b> TEM data demonstrating occasional gold bipyramid sample preparation issues.....	32
<b>Figure 3.2.1</b> Characterization of diblock copolymer used in chapter 2.....	38
<b>Figure 3.2.2</b> Characterization of gold nanorods used in chapter 2.....	39
<b>Figure 3.3.1</b> Placement, alignment, and surface density control of aspect ratio 3 gold nanorods...	42
<b>Figure 3.3.2</b> Placement and alignment control of multiple aspect ratio gold nanorods.....	42
<b>Figure 3.3.3</b> Schematic of gold nanorod deposition on polymer surface.....	44
<b>Figure 3.3.4</b> Raman spectra of increasing surface density, unaligned gold nanorods.....	47
<b>Figure 3.3.5</b> Demonstration of macroscopic gold nanorod alignment due to aligned diblock copolymer film.....	47
<b>Figure 3.3.6</b> Optical images and representative Raman spectra of gold nanorod trenches aligned with, and against, the incident laser polarization.....	49
<b>Figure 3.3.7</b> AFM image and Raman spectra demonstrating Raman signal matching and localization from macroscopically aligned gold nanorods.....	50
<b>Figure 4.2.1</b> Pictures of alignment and solvent vapor exposure systems.....	56
<b>Figure 4.2.2</b> AFM images showing polystyrene-poly(2-vinylpyridine) thin film dissolution upon soaking in propionic and butyric acids.....	56
<b>Figure 4.3.1</b> AFM images of polystyrene-poly(2-vinylpyridine) thin films after poly(2-vinylpyridine) selective solvent exposures.....	58
<b>Figure 4.3.2</b> Height profiles of polystyrene-poly(2-vinylpyridine) thin films exposed to tetrahydrofuran, acetic acid, and propionic acid.....	59

<b>Figure 4.3.3</b> AFM height and phase micrographs, water contact angles, and XPS spectra comparing polystyrene-poly(2-vinylpyridine) thin films after annealing and after tetrahydrofuran vapor exposure.....	59
<b>Figure 4.3.4</b> AFM image and height profile of polystyrene-poly(2-vinylpyridine) thin film after long tetrahydrofuran exposure.....	60
<b>Figure 4.3.5</b> AFM images of polystyrene-poly(2-vinylpyridine) thin films after sequential tetrahydrofuran vapor and poly(2-vinylpyridine) selective solvent exposures.....	60
<b>Figure 4.3.6</b> Height profiles of polystyrene-poly(2-vinylpyridine) thin films after tetrahydrofuran vapor exposure, then acetic, propionic, or butyric acid exposure.....	62
<b>Figure 4.3.7</b> AFM height image, water contact angles, and XPS spectra comparing polystyrene-poly(2-vinylpyridine) thin films after tetrahydrofuran vapor exposure, then propionic acid or ethanol exposure.....	63
<b>Figure 4.3.8</b> SEM and AFM images of polystyrene-poly(2-vinylpyridine) thin films after tetrahydrofuran vapor exposure, then 1% hydrochloric, formic, or propionic acid exposures, followed by a short soak in negatively charged gold nanoparticles.....	64
<b>Figure 4.3.9</b> SEM images of polystyrene-poly(2-vinylpyridine) thin films after tetrahydrofuran vapor exposure, then 1% hydrochloric acid, propionic acid, or ethanol exposures, followed by a long soak in negatively charged gold nanoparticles.....	65
<b>Figure 4.3.10</b> Schematic depiction of polystyrene-poly(2-vinylpyridine) thin film swelling.....	66
<b>Figure 4.3.11</b> AFM height micrographs of Figure 4.3.1 polystyrene-poly(2-vinylpyridine) thin films after another tetrahydrofuran vapor and respective poly(2-vinylpyridine) selective solvent exposures.....	67
<b>Figure 4.3.12</b> AFM height micrographs of Figure 4.3.5 polystyrene-poly(2-vinylpyridine) thin	

films after another tetrahydrofuran vapor and respective poly(2-vinylpyridine) selective solvent exposures.....	68
<b>Figure 4.3.13</b> AFM height and phase micrographs, water contact angles, and XPS spectra of a polystyrene-poly(2-vinylpyridine) thin film after tetrahydrofuran, propionic acid, and tetrahydrofuran vapor exposures.....	69
<b>Figure 4.3.14</b> AFM height and phase micrographs, water contact angles, and XPS spectra of a polystyrene-poly(2-vinylpyridine) thin film after tetrahydrofuran, propionic acid, tetrahydrofuran, and propionic acid vapor exposures.....	69
<b>Figure 4.3.15</b> AFM images of Figure 4.3.5a substrate after subsequent tetrahydrofuran and 10% hydrochloric acid exposures.....	70
<b>Figure 4.3.16</b> AFM images of Figure 4.3.5b substrate after subsequent tetrahydrofuran and 1% hydrochloric acid exposures.....	70
<b>Figure 4.3.17</b> AFM images of Figure 4.3.5c substrate after subsequent tetrahydrofuran and formic acid exposures.....	71
<b>Figure 4.3.18</b> AFM images of Figure 4.3.5d substrate after subsequent tetrahydrofuran and acetic acid exposures.....	71
<b>Figure 4.3.19</b> AFM images of Figure 4.3.5e substrate after subsequent tetrahydrofuran and propionic acid exposures.....	72
<b>Figure 4.3.20</b> AFM images of Figure 4.3.5f substrate after subsequent tetrahydrofuran and butyric acid exposures.....	73
<b>Figure 4.3.21</b> AFM height and phase micrographs of Figure 4.3.5g substrate after subsequent tetrahydrofuran and ethanol exposures.....	74
<b>Figure 4.3.22</b> AFM height profile development of polystyrene-poly(2-vinylpyridine) thin film	

after annealing, tetrahydrofuran exposure, and long, low temperature baking.....	75
<b>Figure 4.3.23</b> AFM height profile development of polystyrene-poly(2-vinylpyridine) thin film after annealing, tetrahydrofuran and propionic acid vapor exposures, and long, low temperature baking.....	75
<b>Figure 4.3.24</b> Cut-away schematic depicting proposed tetrahydrofuran swelling of polystyrene..	76
<b>Figure 4.3.25</b> AFM images of polystyrene-poly(2-vinylpyridine) thin films after tetrahydrofuran treatment, followed by short soaks in poly(2-vinylpyridine) selective solvents....	78
<b>Figure 4.3.26</b> AFM height micrographs of polystyrene-poly(2-vinylpyridine) thin films after tetrahydrofuran exposure, followed by longer soaks in selected poly(2-vinylpyridine) selective solvents.....	78
<b>Figure 4.3.27</b> AFM height micrographs of polystyrene-poly(2-vinylpyridine) thin films after exposure to tetrahydrofuran vapors, then vapors of formic acid, acetic acid, or ethanol for 48 hours.....	79
<b>Figure 4.3.28</b> AFM images, and selected water contact angles and height profiles of polystyrene-poly(2-vinylpyridine) thin films after tetrahydrofuran exposure, then increasing propionic acid vapor exposures.....	79
<b>Figure 4.3.29</b> AFM images of polystyrene-poly(2-vinylpyridine) thin films after tetrahydrofuran treatment, then 1% hydrochloric acid, formic acid, ethanol, or propionic acid exposure, then a propionic acid treatment.....	81
<b>Figure 4.3.30</b> AFM images of polystyrene-poly(2-vinylpyridine) thin films after tetrahydrofuran treatment, then a propionic acid, tetrahydrofuran, then formic acid exposure, or a formic acid, tetrahydrofuran, then propionic acid exposure.....	81
<b>Figure 4.3.31</b> AFM images of polystyrene-poly(2-vinylpyridine) thin film after a tetrahydrofuran	

treatment, then two subsequent formic acid exposures.....	82
<b>Figure 4.3.32</b> AFM images of polystyrene-poly(2-vinylpyridine) thin films after a tetrahydrofuran treatment, then soaked in formic acid and ethanol, or soaked in ethanol and formic acid...	82
<b>Figure 4.3.33</b> AFM images of polystyrene-poly(2-vinylpyridine) thin film after alignment, a tetrahydrofuran vapor exposure, and a propionic acid vapor exposure.....	84
<b>Figure 4.3.34</b> SEM images and polarized UV/Vis absorption spectra of Figure 4.3.33 substrate after a long gold nanoparticle soak and short gold overgrowth.....	84
<b>Figure 4.3.35</b> UV/Vis polarized reflectance results of Figure 4.3.34 substrate.....	85
<b>Figure 4.5.1</b> AFM height and phase micrographs demonstrating the issue encountered trying to align the polystyrene- <i>block</i> -poly(methylmethacrylate) thin films of chapter 3.....	88
<b>Figure 4.5.2</b> SEM images demonstrating the issues encountered while trying to align gold nanorods with the polystyrene-poly(2-vinylpyridine) thin films, as well as the partial success achieved in making thin gold ridges.....	88
<b>Figure 5.1.2.1</b> UV/Vis spectra, and TEM and optical images demonstrating the gold bipyramid purification process.....	95
<b>Figure 5.1.2.2</b> UV/Vis spectra, and SEM, TEM, and optical images demonstrating the problems encountered when trying to use negatively charged silver nanospheres.....	97
<b>Figure 5.1.2.3</b> UV/Vis spectra and TEM and optical images of the silver overgrowth onto the gold bipyramid colloid.....	98
<b>Figure 5.1.3.1</b> Optical images of the xenon lamp induced, dark field oil fluorescence.....	100
<b>Figure 5.1.3.2</b> Dark field and SEM characterizations of gold bipyramid – silver nanosphere heterostructures.....	101
<b>Figure 5.1.3.3</b> Theoretical scattering cross sections of gold bipyramid – silver nanosphere	

heterostructures with varying interparticle separations.....	102
<b>Figure 5.1.4.1</b> Home-built dark field and second harmonic generation microscope picture.....	103
<b>Figure 5.2.1.1</b> Gold bipyramid, DNA linker, and water soluble quantum dot schematic.....	106
<b>Figure 5.2.1.2</b> UV/Vis and photoluminescence spectra comparing the core and core-shell quantum dots, and a TEM image of the core-shell particles.....	109
<b>Figure 5.2.1.3</b> Pictures depicting the quantum dot water solubility process, and confirming that the water soluble dots have the same optical properties as before.....	111
<b>Figure 5.2.2.1</b> UV/Vis and photoluminescence spectra demonstrating independent nucleation during shell growth, and cartoon and UV/Vis and photoluminescence spectra demonstrating increased quantum dot photoluminescence with decanethiol treatment...	114
<b>Figure 5.2.3.1</b> UV/Vis spectra, and photoluminescence spectra, and cryo-TEM images demonstrating our inability to make gold bipyramid – quantum dot hybrids with DNA...	118
<b>Figure 5.2.4.1</b> Dark field scattering, laser scattering, and possible photoluminescence images, demonstrating the issues encountered while trying to make gold bipyramid – quantum dot liquid cells.....	120
<b>Figure 5.2.5.1</b> UV/Vis spectra, photoluminescence spectra, and cryo-TEM image depicting the lack of reproducibility in making gold bipyramid – quantum dot hybrids using amide bond chemistry.....	121
<b>Figure 6.1.1</b> UV/Vis spectra and TEM images of polymer protected gold bipyramids in water and ethylene glycol.....	125
<b>Figure 6.2.1</b> TEM images and EDX spectra of perovskite nanoparticles with different compositions synthesized by the Engel lab.....	127

# PREFACE

In rejecting my NSF GRFP application, a reviewer wrote the following:

‘He briefly described three interesting undergraduate research projects, but none of them panned out to provide useful data. Would the applicant have been better served to work on one project and take it further ,(sic) overcoming the experimental difficulties?’

While writing this thesis and reflecting on my graduate school experience, I think it is safe to say that I did not take the reviewer’s advice. The field of nanomaterials is so vast that it requires one to gain knowledge and experience in many different, and usually disparate, disciplines. Thus, instead of focusing on one technique, synthesis, or methodology, I have been forced to develop expertise in several. I am grateful for this opportunity, since it forced me out of my comfort zone and made me handle problems across almost every aspect of Chemistry. To say I am a better scientist because of this would be an understatement.

And if it hadn’t been for Philippe, none of this could have happened. I am incredibly grateful to have been able to work with him over the course of the past five years. Philippe’s enjoyment of, and dedication to, scientific research has served as an inspiration and a driving force for my own work. His ability to seek out and understand the fundamental aspects of any problem is something I hope to emulate as I move forward with my career. I want to thank Philippe for his mentorship, the opportunity to learn and grow under his guidance, and for showing me how fun and important making your own instrument can be.

When I came to the University of Chicago, I was pretty set on joining the PGS group. I was really excited about the research, and looked forward to contributing to the cutting edge of technology science. What truly sold me on the group, however, were the people who were part of

it. I distinctly miss Dr. Pavlo Zolotavin, to whom I will forever be grateful for starting me in Judo, and for being a mentor and friend when times were hard. I look forward to seeing Dr. Sean Keuleyan again, as I begin my job in the Pacific Northwest, and anticipate many more sessions talking about science. I want to thank Dr. Heng Liu and Dr. Wei Qin for being excellent lab mates, sounding boards for ideas, and for never making too much fun of my horrible Chinese. I want to thank Dr. Yuval Yifat and Dr. Xiaoying Liu for working with me on a fun, and unexpectedly challenging, collaboration. Finally, I want to thank Prof. Emmanuel Lhuiller, Prof. Kwang Seob Jeong, Dr. Zhiyou Deng, Guohua Shen, Menglu Chen, and Matt Ackerman, as they move forward with their careers. We learned a lot together, and I wish you all the best of luck.

I want to thank my committee members, Prof. Paul Nealey, Prof. Steve Sibener, and Prof. Yossi Weizmann, for not only agreeing to be on my defense committee, but for also collaborating with me on several of the projects in this thesis. The broad scientific background I've gained came about by working with, and learning about, the expertise of your labs. I also want to thank the JFI and the University of Chicago Chemistry department for fostering and maintaining a collegial working environment. I want to thank Prof. Tom Witten for inviting me to give MRSEC brownbag lunch talks, Prof. Greg Engel, Prof. Norbert Scherer, Prof. Heinrich Jaeger, and Prof. Dmitri Talapin for letting me borrow equipment and always being willing to talk about science, and Prof. Rich Jordan, Prof. Mike Hopkins, and Prof. Bozhi Tian for always being friendly faces. I want to thank the rest of my collaborators, Prof. John Sader, Dr. Debadi Chakraborty, Dr. Qianqian Tong, Dr. Alexander Filatov, Jonathan Raybin, Lili Wang, Nicholas E. Williams, John P. Otto, Dugan Hayes, Ryan Wood, Kyle Gibson, and especially Prof. Matt Pelton, as well. I want to thank Dr. Pete Dahlberg, Sara Massey, and Igor Fedin for letting me borrow equipment from their labs, and for teaching me how to properly use it. I want to thank Qiti Guo, Joe Austin, and Pedro Rodriguez

for teaching me how to use the many shared instrument facilities, without which I could never have performed my research, and for helping me with various aspects and/or data collection for my projects. I want to thank Justin Jureller for the same thing, and for being a source of help and advice for many general, ‘can we do this’ experimental questions. I have greatly valued his opinion on a number of issues. I also want to thank Dr. Vera Dragisich and Melinda Moore for helping me with the various administrative issues that cropped up over the course of my PhD.

I want to thank my undergraduate professors, Prof. Erich Uffelman, Prof. Matt Tuchler, Prof. Steve Desjardins, Prof. Lisa Alty, Prof. Marcia France, Prof. Fred LaRiviere, Dr. Christine Winschel, Dr. Andrea Abry, Prof. Michael Pleva, Prof. Dan Mazilu, Prof. Joel Kuehner, Prof. David Bello, as well as Pr. Mark Schroeder, Phil Schoner, and John White, for mentoring me and fostering in me a love of learning that lead me to pursue a PhD.

I want to thank the rest of my friends who have supported me throughout my time here at the University of Chicago. Without Alex Linkin, Dr. Johnny Zimmerman, Grant Langlois, Traci Beilharz, Dr. Chad Heaps, Clare Heaps, John Jumper, Carolyn Jumper, Mark Whitfield, Dr. Kartik Prabhu, Dr. Matt Kurley, Dr. Dan O’Hanlon, Dr. Julian Freed-Brown, Dr. Landon Durak, Dr. Dmitry Dolzhenkov, Nicole James, Dr. Ken Ellis-Guardiola, Mary Andorfer, Judith Kamm, Rhys Povey, Greg Lennon, Will Richardson, Anne Parlato, Chris Browning, Mary Browning, Ben Denton, Charles, Mike Kuntz, Nick Lanoue, Zach Henderson, Pr. Jacob Gaughert, Pr. John Henry III, Victor, Jay, and Hector, the UChicago Judo Club, Tohkon Judo Academy, and many more, my graduate school career could not have been as great. I appreciate everything y’all did with, and for, me. I especially want to thank my family, Ed, June, and Chris Malachosky, and Marie Dare, for their loving support for me over these past years. It has meant a great deal.

Finally, I want to thank Sarah Brown, whose support made this past year possible.

# ABSTRACT

The plasmon phenomenon is the driving force behind noble metal nanoparticle research. While some work synthesizing new kinds of particles is still performed, a wider range of opportunities is available if these nanoparticles' self-assembly in solution and on substrates can be controlled. This text presents several such methodologies, describing each assembly process and characterizing the resulting structures. The selective, aqueous dimerization of gold bipyramids is the first study. These novel antennae are created by stabilizing the gold bipyramid's ligand shell, then linking the particles with amino acids. Because of the gold bipyramids' monodispersity and the precision of the reaction, the assembly can be monitored to ensure high dimer yield. Gold nanorod alignment on, and by, a shallowly corrugated diblock copolymer thin film demonstrates the power of template assisted assembly. Controlling the alignment of the underlying film controls the gold nanorods' alignment, yielding mesoscale structures with orientation dependent optical properties. With intentional design, other polymer substrates are used to construct gold bipyramid – silver nanosphere plasmonic heterostructures. With proper ligand-polymer interaction tailoring, this result demonstrates how this technique can rationally create almost any noble metal nanoparticle based structure. The nonlinear optical properties of these heterostructures are currently being investigated.

These assemblies are all unique, and barely represent a fraction of what plasmonic nanoparticle assembly research can entail. Given polymer templates' efficacy in controlling these particle's deposition and alignment, a study of a diblock copolymer thin film's swelling behavior is also contained in this work. By understanding and controlling the film's surface morphologies, its efficacy for noble metal nanoparticle alignment can be determined. Gold nanoparticles are used

to probe the chemical nature of diblock's swollen surface, and concurrently demonstrate that it can align small, highly charged, plasmonic nanoparticles. Several attempts to synthesize solution-based plasmonic antennae and fluorophore hybrids are also described, resulting in an introduction to the realm of semiconductor nanocrystal synthesis. Although these gold bipyramid – water soluble quantum dot systems have not yet been achieved, with some refinement, such systems should be possible. Finally, following the theme of unexpected research directions, two collaborations are presented that utilized the nanoparticle synthesis and characterization skills required to perform the rest of this research.

# Chapter 1. Introduction

Gold nanoparticles (AuNPs) are the oldest of all colloidal nanomaterials. Used in the Lycurgus cup, red stained glass,<sup>1</sup> and accidentally made by Faraday,<sup>2</sup> their usefulness was long limited due to the inability to control their optical properties. This changed with the first syntheses of anisotropic gold particles in the early 2000s.<sup>3-5</sup> Since then, an explosion of research into AuNPs has occurred, yielding a wide range of particle shapes<sup>6-11</sup> and compositions.<sup>10-13</sup> Gold nanorods (AuNRs) and gold bipyramids (AuBPs) have attracted significant attention due to their simple syntheses, shape control, tunable optical properties, and significant enhancements of applied electric fields.<sup>6,11,14,15</sup> These particles have already found biomedical, sensor,<sup>11,16-18</sup> and even catalytic<sup>11</sup> applications.

More opportunities present themselves if the aggregation of these NPs can be controlled.<sup>19</sup> Whether in solution<sup>20,21</sup> or on a substrate,<sup>22,23</sup> rationally designed electromagnetic hot-spots<sup>22-26</sup> and extended optical tuning<sup>20,21,25,27-29</sup> can be achieved by self-assembling AuNRs and AuBPs. The promise of new uses for these NPs,<sup>30</sup> combined with the interesting synthetic challenges and exciting optical properties, motivated me to research noble metal NP self-assembly and characterize the resulting structures. In the remainder of this chapter, I will introduce the phenomenon that makes noble metal NPs so interesting, and explain how it influenced the NPs and methodologies with which I worked. In chapter 2, I present my first project, where I synthesized and characterized AuBP dimers for the first time. Due to the AuBPs' monodispersity,<sup>20</sup> I was able to match the single particle scattering to the *in-situ* solution UV/Vis spectra of the dimers, which cannot be done with AuNRs.<sup>20</sup> Chapter 3 is the result of a collaboration with the Sibener lab, where we successfully controlled the assembly of AuNR monolayers on shallowly

corrugated polymer templates. The AuNRs deposited into the polymer trenches nearly perfectly, and by controlling the underlying polymer film's alignment, we controlled the alignment of the AuNRs. This resulted in our AuNR monolayers demonstrating macroscopic, polarization dependent surface enhanced Raman scattering (SERS) spectra,<sup>22</sup> which had never been previously reported.

In chapter 5, I present the unpublished work of two on-going projects that intend to use the strong electromagnetic field enhancements at the tips of AuBPs<sup>15</sup> to create novel hybrid structures with large optical nonlinearities. The first project, in chapter 5.1, has yielded the creation of unique, AuBP and silver coated gold nanospheres (Ag/AuNS) heterostructures by controlling their placement on pre-patterned polymer substrates. With this result, our collaboration with the Nealey lab demonstrates the generalizability of their methodology to make heterostructure arrays involving almost any noble metal NP. We further hope to show that coupling the field enhancement of a AuBP to a Ag/AuNS scatterer creates a system with large second harmonic generation (SHG) responses. The second project, in chapter 5.2, covers the several unpublished attempts to synthesize single, linked, AuBP – quantum dot (QD) systems. From a simple application of Fermi's Golden Rule,<sup>31,32</sup> our goal was to make structures where the electric field enhancements of the AuBPs significantly enhanced the photoluminescent (PL) properties of a nearby QD. We had also wanted to probe the regimes of PL enhancement and quenching by using pH sensitive DNA strands, allowing us to determine their distance dependence with one system. This work is still ongoing.

In chapters 4 and 6, I present work that is slightly outside the main scope of my thesis. Chapter 4 is a soon to be submitted project, where, in my attempts to expand the work of chapter 3, I managed to stumble upon novel swelling morphologies of a diblock copolymer thin film. The

focus of my work then shifted to characterizing and investigating how these morphologies arose. In the process, I demonstrated that these swollen films can control the macroscopic alignment of small, spherical, highly charged AuNSs, from which larger particles can be grown. This proves to serve a dual purpose, since the particles also probe the film's nanoscopic chemical nature. Chapter 6 contains my contributions as a NP synthesis and characterization expert to two other collaborations. For the first, I synthesized AuBPs that were used to probe the viscoelastic fluid dynamics regime in simple liquids,<sup>33</sup> and for the second, I took TEM images and performed elemental analysis on incredibly stable and bright perovskite NPs.<sup>34</sup>

The conclusion is a more complete summary of the work I've so far described, and provides several ideas for general and specific directions of future research. The fact that each of my projects was unique, presenting its own challenges, methodologies, and results, demonstrates the impressive number of research opportunities available in studying noble metal NP self-assembly. Carefully manipulating the phenomenon that makes these NPs so special yields systems with exciting properties and unexpected potential applications.

## **1.1 The Plasmon Phenomenon**

The fascinating optical properties of noble metal NPs arise because the Drude model of the free electron sea survives the transition to the nanoscale. This means that noble metal NPs' conduction band electrons can still be treated as a freely moving plasma.<sup>35,36</sup> However, the positively charged background cores' existence is now significant. Thus, when the plasma is displaced through exposure to an oscillating electric field, a dipole develops that exerts a restoring force, and causes the plasma to resonate at specific frequencies.<sup>35,36</sup> When the source of the oscillating electric field is a photon, this phenomenon is called a localized surface plasmon

resonance (LSPR), and the frequencies at which it occurs depend upon the metal, the medium, and the dimensions of the NP.<sup>35,36</sup>

To understand how this frequency dependence arises, we must first understand the frequency dependence of a metal's dielectric function. The equation of motion for a plasma when displaced by an oscillating electric field is well described by that of a damped harmonic oscillator,<sup>35</sup>

$$m \frac{d^2 \vec{x}}{dt^2} + m\gamma \frac{d\vec{x}}{dt} = -e\vec{E} \quad (1)$$

where  $\vec{x}$  is the plasma's displacement,  $m$  is the effective optical mass of an electron,  $\gamma$  is the electronic damping parameter,  $e$  is the charge of an electron, and  $\vec{E}$  is the applied electric field.<sup>35</sup>

If we assume that the electric field is harmonic in time,

$$\vec{E}(t) = \vec{E}_0 e^{-i\omega t} \quad (2)$$

then so too is the displacement,

$$\vec{x}(t) = \vec{x}_0 e^{-i\omega t}, \quad (3)$$

such that

$$\vec{x}_0 = \frac{e\vec{E}_0}{m(\omega^2 + i\gamma\omega)}. \quad (4)$$

The macroscopic polarization (dipole moment per unit volume) of the plasma is then

$$\vec{P} = -ne\vec{x} = \frac{-ne^2}{m(\omega^2 + i\gamma\omega)} \vec{E}, \quad (5)$$

where  $n$  is the number density of the electrons.<sup>35</sup> Given the relationships between the dielectric displacement ( $\vec{D}$ ), and  $\vec{P}$  and  $\vec{E}$ ,

$$\vec{D} = \epsilon_0 \vec{E} + \vec{P} = \epsilon_0 \epsilon(\omega) \vec{E}, \quad (6)$$

where  $\epsilon_0$  is the electric permittivity of vacuum and  $\epsilon(\omega)$  is the dielectric function of the metal, then

$$\varepsilon_0 \varepsilon(\omega) \vec{E} = \varepsilon_0 \vec{E} + \frac{-ne^2}{m(\omega^2 + i\gamma\omega)} \vec{E} = \left(1 - \frac{ne^2}{\varepsilon_0 m(\omega^2 + i\gamma\omega)}\right) \varepsilon_0 \vec{E}, \quad (7)$$

meaning

$$\varepsilon(\omega) = 1 - \frac{ne^2}{\varepsilon_0 m(\omega^2 + i\gamma\omega)}. \quad (8)$$

This is the dielectric function of a free plasma, which doesn't account for the background of positive nuclei in a metal. Thus, the dielectric function for a metal replaces '1' with a constant,  $\varepsilon_\infty$ , appropriately named the dielectric constant of the metal. Thus, the frequency dependent dielectric function for a metal is

$$\varepsilon_m(\omega) = \varepsilon_\infty - \frac{ne^2}{\varepsilon_0 m(\omega^2 + i\gamma\omega)}. \quad (9)$$

With this equation, we can understand how the LSPR of noble metal NPs arise. In 1908, Gustav Mie published the seminal work detailing the interaction of light with small gold spheres, using a multipole expansion from which the frequency dependent extinction cross section,  $\sigma_{ext}(\omega)$ , of the particles can be determined.<sup>35-37</sup> For particles with dimensions much smaller than the incident light's wavelength, the phase of the oscillating electromagnetic field can be considered constant, making all but the first term of Mie's expansion negligible.<sup>35,36</sup> This is the quasi-static, or dipole, approximation, and describes the LSPR behavior of noble metal NPs 20 – 100 nm in diameter very well, yielding

$$\sigma_{ext}(\omega) = 9 \frac{\omega}{c} \varepsilon_e^{3/2} V \frac{Im(\varepsilon_m(\omega))}{|\varepsilon_m(\omega) + 2\varepsilon_e|^2}, \quad (10)$$

where  $c$  is the speed of light,  $\varepsilon_e$  is the dielectric constant of the environment,  $V$  is the NPs volume, and the dielectric function of the metal is defined as in (9).<sup>35,36</sup> In the small damping limit, i.e., when the imaginary part of  $\varepsilon_m(\omega)$  can be ignored,  $\sigma_{ext}(\omega)$  is maximized when

$$Re(\varepsilon_m(\omega)) = -2\varepsilon_e. \quad (11)$$

The frequency at which this occurs is the LSPR frequency of the AuNS.

In 1912, Richard Gans extended Mie's theory to ellipsoidal AuNPs.<sup>35,36,38</sup> Now, for a prolate spheroid, the extinction cross section within the dipole approximation is

$$\sigma_{ext}(\omega) = 9 \frac{\omega}{c} \varepsilon_e^{3/2} V \sum_j \left[ \frac{(1/P_j^2) \text{Im}(\varepsilon_m(\omega))}{|\varepsilon_m(\omega) + [(1-P_j)/P_j] \varepsilon_e|^2} \right], \quad (12)$$

where  $P_j$  is the depolarization factor per axis, given by

$$P_A = \frac{1-e^2}{e^2} \left[ \frac{1}{2e} \ln \left( \frac{1+e}{1-e} \right) - 1 \right] \quad (13)$$

for the major axis, and

$$P_B = P_C = \frac{1-P_A}{2} \quad (14)$$

for the minor axes.<sup>36</sup> In this instance,  $e$  is the eccentricity of the particle, defined as

$$e = \sqrt{1 - \frac{1}{R^2}} = \sqrt{1 - \left( \frac{B}{A} \right)^2}, \quad (15)$$

where  $A$  is the length of the major axis,  $B = C$  are the length of the minor axes, and  $R$  is the aspect ratio of the NP.<sup>36</sup> It is through this term that the dimension dependence of LSPRs in anisotropic NPs arises. The LSPR condition is now

$$\text{Re}(\varepsilon_m(\omega)) = \left( \frac{1-P_j}{P_j} \right) \varepsilon_e, \quad (16)$$

and has two solutions.<sup>35,36</sup> The plasmon along the minor axis is called a transverse surface plasmon (TSP), and is close to the LSPR frequency of NSs (Figure 1.1.1a).<sup>39</sup> The plasmon along the major axis is called the longitudinal surface plasmon (LSP), and is redshifted from the TSP.<sup>35,36</sup> As  $R$  increases, the LSP redshifts even further, giving rise to the tunable optical properties of anisotropic NPs (Figure 1.1.1a).<sup>36</sup> As  $A$  increases past  $\sim 100$  nm, the dipole approximation no longer completely describes  $\sigma_{ext}(\omega)$ , and higher order terms of the multipole expansion must be taken into account.<sup>35,36</sup>

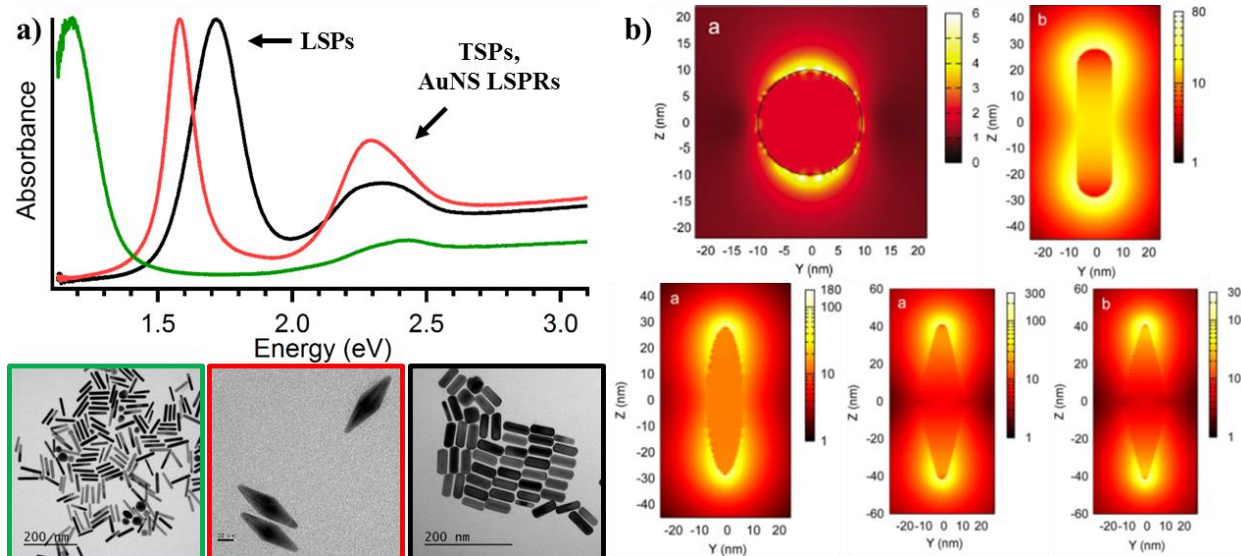


**Figure 1.1.1** a) UV/Vis spectra and TEM images of AuNRs and AuBPs I synthesized, demonstrating the LSP tuning of the structures. In all three syntheses, the large spectral feature around 2.3 eV is a combination of their TSP and the AuNS biproduct LSPR. b) Theoretical simulations of the electric field enhancements of AuNPs of different shape and tip sharpness at their plasmon resonances. Spheres, being the most round, show the least enhancement, and AuBPs, having the sharpest tips, show the most enhancement. Figure 1.1b is adapted with permission from ref. 15. Copyrighted by the American Physical Society, 2007.

## 1.2 Gold Nanorods and Gold Bipyramids

A consequence of Mie theory is that plasmonic NPs can be treated as nanoscale antennae, locally enhancing the applied electromagnetic field.<sup>15,40</sup> Strongest at a noble metal NP's plasmon resonance, this is known as the lightning rod effect, and since antennae focus electric fields to points, anisotropic NPs create much larger enhancements than their spherical counterparts (Figure 1.1.1b).<sup>15</sup> While anisotropic, plasmonic NPs of silver and copper exist, they tend to be less stable than gold counterparts,<sup>41,42</sup> are harder to synthesize,<sup>43</sup> and are limited in shape to spheres or rods.<sup>44</sup>

<sup>47</sup> This last point is very pertinent for electromagnetic field enhancements, since their magnitude directly correlates with NP tip sharpness (Figure 1.1.1b).<sup>15</sup> Thus, the AuBPs first synthesized in our lab<sup>6</sup> over a decade ago are the noble metal NPs with the strongest electromagnetic field enhancements to date (Figure 1.1.1b),<sup>15</sup> with the additional benefit of being the most monodisperse colloiddally synthesized anisotropic plasmonic NPs.<sup>6</sup> Since extensive AuBP colloid and single particle characterizations had previously been performed in our lab,<sup>6,15,48-52</sup> the impetus for my research was to manipulate and utilize the AuBP's extreme lightning rod effect by controlling their assembly (Chapters 2<sup>20</sup> and 5). While this did not always work (Chapters 3<sup>22</sup> and 4), I was always able to pull from the synthetic library of AuNPs to find plasmonic structures to use in my investigations.

## Chapter 2. Gold Bipyramid Nanoparticle Dimers<sup>20</sup>

*This paper was originally published in The Journal of Physical Chemistry C on February 28<sup>th</sup>, 2014, and is adapted with permission here: Malachosky, E. W.; Guyot-Sionnest, P. Gold Bipyramid Nanoparticle Dimers. J. Phys. Chem. C **2014**, 118 (12), 6405–6412. Copyright 2014 American Chemical Society.*

Special thanks to: Dr. Gang Chen, Prof. Yossi Weizmann

This chapter is my first, first-author paper, and is the aqueous synthesis of gold bipyramid (AuBP) dimers. The methodology, its selectivity, and the resulting structures' characterization with optical dark-field and scanning electron microscopy are presented and discussed. In the bowtie orientation, the dimers exhibit a 20% redshift in their plasmon resonance as compared to the individual particles, with a weak dependence on the interparticle separation. From the analysis, it is found that the in situ absorption peaks that develop during the assembly can be assigned to specific dimer structures, which have not been shown previously. Lastly, the kinetics of the assembly are analyzed.

### 2.1 Introduction

Interest in anisotropic colloidal gold nanoparticles (AuNPs) stems from their tunable plasmon resonances and electric field enhancements.<sup>17,53</sup> Gold nanorods (AuNRs) are the most studied example of these particles,<sup>4–6,14,15,24,25,29,54–78</sup> but even the best AuNR samples exhibit aspect ratio variations that cause their inhomogeneous linewidth to exceed their homogenous linewidth by at least two fold. Gold bipyramids (AuBPs), however, have better shape homogeneity, the narrowest

ensemble linewidth of all plasmonic colloidal particles, and are predicted to have larger near-field enhancements due to their sharp tips.<sup>6,15,58,79,80</sup> This makes them natural choices for seeking novel and enhanced optical properties.

We have developed an aqueous methodology for the synthesis of AuBP dimers as a starting point for future field enhancement and nonlinear optical studies. The methodology, its selectivity, and the characterization of the resulting structures are presented and discussed. Previous work on AuBPs<sup>25,64</sup> and AuNRs<sup>24,25,29,59–74</sup> showed the possibility of assembling dimers and extended chains of anisotropic AuNPs with some tip to tip selectivity. The UV/Vis spectra of these reactions exhibit a broad, red-shifted plasmon resonance as they proceed, attributed to the variety of aggregate structures formed. In this paper, we demonstrate the selective functionalization of AuBPs and their assembly into bowtie structures. From their joint structural and optical characterization, we show the dependence of the dimer's plasmon resonance on their geometry and that the distinct spectral features that develop in solution correspond to the plasmon resonances of specific dimer structures. Lastly, we analyze the kinetics of the reaction and show that they do not fit a simple second order model.

## 2.2 Experimental Methods

**Materials.** Hexadecyltrimethylammonium bromide (CTAB,  $\geq 99\%$ ), gold (III) chloride trihydrate ( $\geq 99.9\%$  metals basis,  $\text{HAuCl}_4$ ), silver nitrate (99.9999%,  $\text{AgNO}_3$ ), L-ascorbic acid ( $\geq 99.0\%$ , vit-C), sodium citrate dihydrate ( $\geq 99\%$ ,  $\text{Na}_3\text{Cit}$ ), sodium borohydride ( $\geq 98.5\%$ ,  $\text{NaBH}_4$ ), L-cysteine (97%), L-glutathione ( $\geq 98\%$ ), 2-mercaptoethanol ( $\geq 99\%$ ), 3-mercaptopropionic acid (3-MPA,  $\geq 99\%$ ), cysteamine ( $\geq 95\%$ ), and tetra(ethylene glycol)dithiol (97%) were all purchased from Sigma Aldrich and used without further purification. 5-bromosalicylic acid (5-BSA,  $\geq 98.0\%$ ) was purchased from TCI and used without further purification. Hydrochloric acid (HCl, 1 N) was

purchased from Fisher and used without further purification. 1 mm thick, indium-tin-oxide (ITO) coated glass microscope slides were purchased from NANOCS and were plasma cleaned before use. 18.7 m $\Omega$  nanopure water (NPH<sub>2</sub>O) was obtained from the MRSEC filtration system.

**Instrumentation.** UV/Vis spectra were recorded using an Agilent HP 8453. Scanning electron microscope (SEM) images were taken using a FEI NanoSEM at both 50,000x and 400,000x at operating voltages of 15 kV and 19.5 kV. Transmission electron microscope (TEM) images were taken using a FEI Tecnai F30 TEM operating at 300 kV. HRTEM images were obtained by dropcasting a few drops of the solutions onto a formvar coated, lacy carbon grid, wicking away the excess liquid, and air drying the grid. Dark-Field (DF) optical microscopy spectra were recorded using a home-built microscope with an Andor iDus CCD air cooled to -70 °C as the detector (Figure 2.2.1). The microscope consisted of a 50 W tungsten halogen lamp, an oil immersion condenser (NA 1.2-1.4), Zaber Technologies T-LS28E X-Y mechanized stages, a 60x objective (NA 0.85), and a home-built spectrometer consisting of a lens focused onto a transmission grating. The system was calibrated using a Helium-Argon lamp. The ITO-glass substrates were patterned with a numbered, 100  $\mu$ M x 100  $\mu$ M gold grid system to allow the optical and structural matching.

**Gold Bipyramid Nanoparticle Dimer Synthesis.** AuBPs were synthesized as previously described,<sup>6</sup> which involves two steps. To synthesize the AuBP seeds, in 18.95 mL of NPH<sub>2</sub>O under vigorous stirring at room temperature (RT) were mixed 250  $\mu$ L of 10 mM HAuCl<sub>4</sub>, 500  $\mu$ L of 10 mM Na<sub>3</sub>Cit, and 300  $\mu$ L of NaBH<sub>4</sub> solutions. The colloid was allowed to age for two hours, and should be clear, pink-orange color. To synthesize the AuBPs, 364  $\pm$  4 mg of CTAB were dissolved in 10 mL of NPH<sub>2</sub>O with vigorous stirring at 30 °C. To this was then added 500  $\mu$ L of 10 mM HAuCl<sub>4</sub>, 100  $\mu$ L of 10 mM AgNO<sub>3</sub>, 200  $\mu$ L of 1 M HCl, and 80  $\mu$ L of 100 mM vit-C. The color

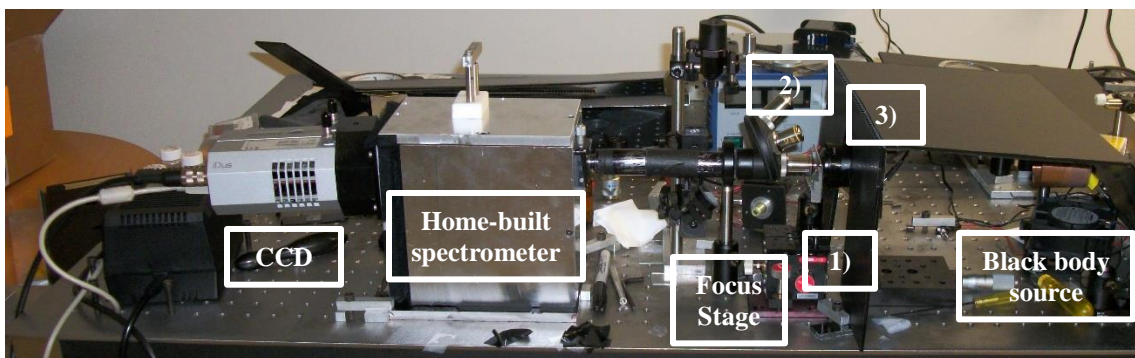


**Figure 2.2.1** Picture of our home-built dark field microscope. 1) is the mechanical sample stage, 2) marks the objectives and nose-piece holder, and 3) marks the dark-field condenser.

will change from gold-orange to clear as the Au(III) is reduced to Au(I). Then, the desired amount of AuBP seeds were added, and the reaction was allowed to run for two hours. Since the AuBP seeds age with time, the correct amount to add is difficult to predict. Thus, these reactions were usually performed in quadruplicate. After the AuBP synthesis, the colloid was centrifuged at 30 °C and 8500 g for 20 min. The supernatant was decanted and the pellet resuspended in 10 mL of a 1 mM CTAB/200  $\mu$ M 5-BSA stabilization solution. The colloid was centrifuged twice more under the same conditions, with the supernatant decanted and the pellet resuspended with the stabilization solution each time. After the final centrifugation, the pellet was resuspended to 2 mL and stored at 8 °C. It was found to be usable for over a month. The colloid was characterized using UV/Vis spectroscopy and TEM (Figure 2.2.2).

Typical AuBP assembly reactions were performed at room temperature in a 4 mL cuvette and were monitored with time-resolved UV/Vis spectra. An aliquot of the stock AuBP colloid (125  $\mu$ L) was diluted with  $\text{NPH}_2\text{O}$  water (2.725 mL) and mixed with 100  $\mu$ L of a 30 mM HCl solution to obtain pH=3. An initial UV/Vis spectrum was recorded. 50  $\mu$ L of a 6 mM linker solution were then swiftly added, mixed, and UV/Vis spectra recorded at constant intervals over the course of

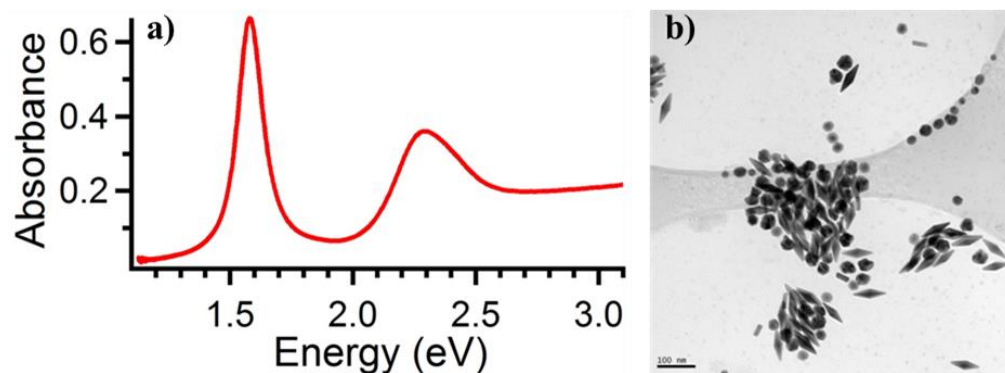


**Figure 2.2.2** a) UV-Vis absorption spectrum of as synthesized AuBP colloid. b) Representative TEM image of the particles in a).

the reaction. The final volume of every reaction mixture was 3 mL. The AuBP and CTAB concentrations are estimated to be 30 pM and 42  $\mu$ M, respectively, and the linking molecule's concentration is 100  $\mu$ M. The diluted colloid, before the addition of the linker, is stable for much longer than the lifetime of the reaction (Figure 2.2.3).

For the samples imaged with the DF microscope, half as much stock colloid (62.5  $\mu$ L) mixed with the same volume of the stabilization solution, was used while all other reaction conditions were kept the same. These assemblies evolved to a predetermined point, defined by their optical spectra, and then a few drops of the reaction mixture was spincast for 10 s at 6000 rpm onto an ITO-glass substrate. The substrate was vacuum-dried for five minutes and analyzed using DF and low resolution SEM. After this data had been collected, the substrate was briefly plasma cleaned to remove dirt buildup and allow high resolution (HR) SEM imaging.

## 2.3 Results and Discussion

Building from the previous literature,<sup>64,65,78</sup> initial assembly experiments were performed on diluted aliquots of stock AuBP colloids using only CTAB and the amino acid glutathione. A broad,

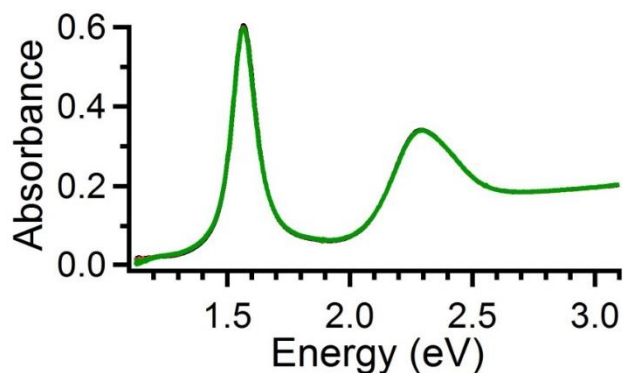


**Figure 2.2.3** UV/Vis spectra of the reaction colloid monitored for an hour without the addition of a linker molecule. The lack of change in the spectra indicates that the reaction mixture is stable and the changes in the UV/Vis spectra of the reaction solutions are caused by the linking molecules.

redshifted plasmon resonance developed, indicating that aggregation occurred, and the greater reduction of the AuBP longitudinal plasmon resonance (LSP) at  $\sim 1.6$  eV over the gold nanosphere (AuNS) resonance at  $\sim 2.3$  eV indicated that the AuBPs were being preferentially aggregated. However, these reactions suffered from large variability in their time and spectral feature evolution (Figure 2.3.1).<sup>29</sup> Suspecting this was caused by poor control of the CTAB concentration, the AuBP colloids were repeatedly centrifuged and resuspended with a 2 mM CTAB solution, which was the lowest CTAB concentration that maintained particle stability. This did not improve the assembly reproducibility. Thus, modifications to the storage temperature, the age of the stock colloid,<sup>29</sup> and the pH of the reaction solution were studied. The most reproducible results, for any sample age, were achieved when the stock colloids were stored at 8 °C before use and the reactions carried out at a pH of 3, ensuring the zwitterionic form of glutathione and preventing its oxidation.

The remaining variability was assigned to inhomogeneous CTAB bilayers,<sup>81</sup> which would allow non-specific binding interactions to occur. Aromatic salts, such as 5-BSA, are known to

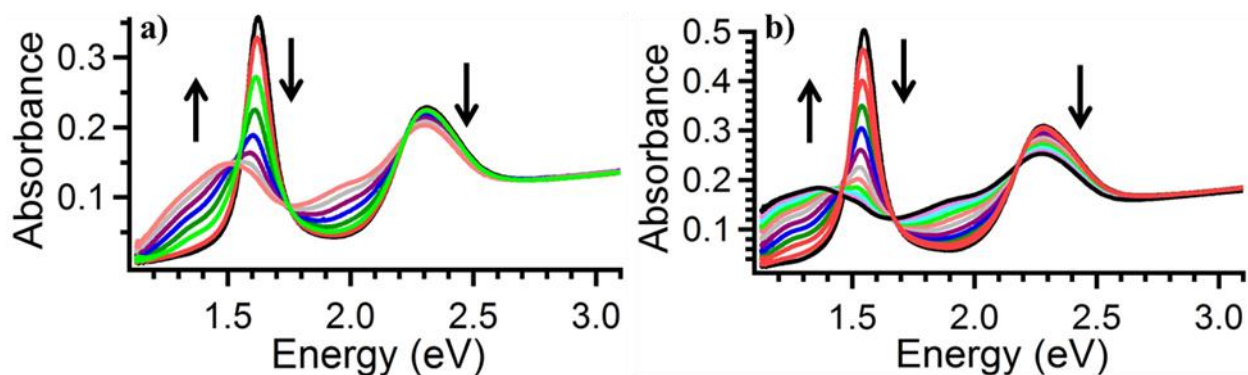


**Figure 2.3.1** Time resolved UV/Vis spectra of early AuBP assembly reactions using two different stock colloid samples. The spectra exhibit very different shapes, even though the stock colloids were treated the same and the reaction mixtures were the same. The arrows indicate the how the peaks evolve with time.

stabilize cylindrical CTAB micelles at lower concentration by improving CTAB's micellar packing parameter.<sup>82-84</sup> Ye et al. recently used this fact to improve AuNR syntheses,<sup>14</sup> suggesting the existence of more homogeneous cylindrical bilayers on the particles. Thus, the stabilization solution was changed to a CTAB/5-BSA mixture. Figure 2.3.2 compares the UV/Vis spectra of assemblies performed with the CTAB and the CTAB/5-BSA solutions. The latter develops better defined spectral features.

We noted in all of these reactions that the LSP of the AuBPs immediately (<30 s) and permanently shifted upon the addition of the glutathione linker. For the assemblies performed with CTAB, this is a ~4 meV redshift, (Figure 2.3.3a, Figure 2.2.3), while it is a ~6 meV blueshift (Figure 2.3.3b) for reactions performed with the CTAB/5-BSA mixture. Because this shift occurred in every reaction, we attribute it to the glutathione binding to the AuBPs and assign it to the plasmon resonance's dependence on its dielectric environment.<sup>37</sup> The refractive indices of the molecules around the AuBPs are 1.435, 1.654, and estimated 1.55 for CTAB, 5- BSA, and

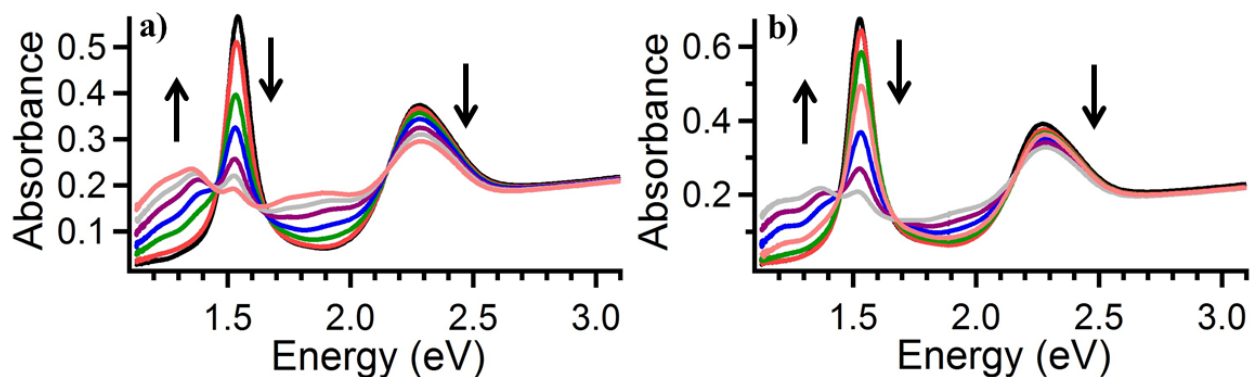


**Figure 2.3.2** a) Representative time resolved UV/Vis spectra of an assembly reaction using glutathione and the 2mM CTAB stabilization solution. b) Representative time resolved UV/Vis spectra of an assembly reaction using glutathione after the stabilization solution was changed to 1mM CTAB/ 200 $\mu$ M 5-BSA. The arrows indicate the spectral evolution with time.

glutathione, respectively. Thus, the AuBP LSP's red-shift upon the addition of glutathione in a CTAB solution is due to an increase in its local polarizability, while its blue-shift in the CTAB/5-BSA solution is due to a polarizability decrease. The fact that these shifts occur on a much faster time scale than the assembly indicates that the glutathione (in 100x excess for full surface coverage) immediately adsorbs to the AuBPs' surfaces. Others have proposed that thiol linkers can only access AuNP surfaces through locations of poor CTAB bilayer coverage,<sup>64,78</sup> such as the tips, but we consider this unlikely given the strong Au-thiol bond compared to the Au-CTAB non-specific interaction. Therefore, we propose that the linker adsorption is not restricted to the tips but rather that the AuBPs are fully coated with glutathione, on top of which is the CTAB/5-BSA bilayer. The tip selective assembly then occurs due to glutathione exposure at regions where the bilayer has broken down due to geometric stress.

AuNP assembly with glutathione was first proposed by Sudeep et al. to arise from a two point electrostatic interaction between the zwitterionic head groups on different particles.<sup>64,78</sup> Since

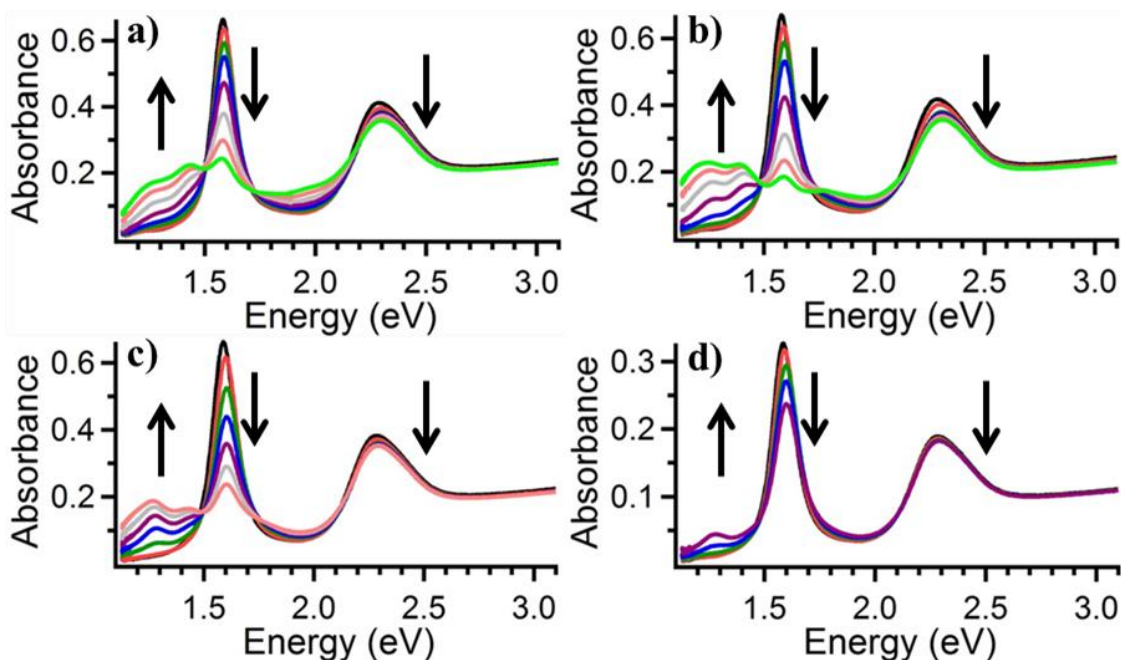


**Figure 2.3.3** Comparison of assembly reactions performed using a) glutathione b) cysteine under the standard reaction conditions. The red-shifted peaks in the cysteine assembly are better defined than the same peaks in the glutathione assembly. c) and d): The spectra of the cysteine assemblies performed for characterization. c) is the reaction performed with the full, 125  $\mu\text{L}$  aliquot of stock colloid and d) is the reaction performed with the half, 62.5  $\mu\text{L}$  aliquot and 62.5  $\mu\text{L}$  of stabilization solution. The sample made for structural and optical analysis was made at the last taken time point in d). The arrows indicate how the spectra evolve with time.

AuNR assembly has been achieved through a variety of other mechanisms as well, including covalent dithiol linking and hydrogen bonding interactions,<sup>24,25,29,59–77</sup> we also investigated other water soluble thiols as linkers. These reactions were performed on the same stock colloid and monitored for one hour, with the results shown in Figure 2.3.4. To explicitly determine the importance of the zwitterionic head group, assemblies were performed with 3-MPA at pH=9 ( $-\text{COO}^-$ , Figure 2.3.4a) and cysteamine at pH=3 ( $-\text{NH}_3^+$ , Figure 2.3.4b). The 3-MPA induced an

immediate blue-shift, which we interpret as its rapid diffusion through the bilayer and adsorption to the AuBPs' surfaces, but the spectral evolution indicates that aggregation did not occur. This could be due to the negatively charged carboxylate group stabilizing the CTAB bilayer in a similar effect to 5-BSA.<sup>14,83,84</sup> The cysteamine reaction exhibited a slow blue shift, indicating that it did not reach the AuBP surfaces quickly, probably due to repulsion from the positive bilayer. The slight shoulder in the UV/Vis spectra that developed over long time indicated the possibility of slow, non-specific aggregation. This was most likely caused by the bilayer's destabilization by the positively charged ammonium group. To test for hydrogen bonding, reactions were performed with 3-MPA and mercaptoethanol at pH=3 (-COOH and -OH, Figures 2.3.4c,d respectively). Both reactions exhibited a slow blue-shift and a small amount of slow, non-specific aggregation, indicating the slow diffusion of the neutral, hydrophilic species through the CTAB bilayer. This would eventually result in a gold surface terminated in neutral -OH groups that could destabilize the bilayer and cause the observed aggregation. The similar results for both molecules indicate that hydrogen bonding is not a large influence on our assembly.

Covalent linking interactions were tested using tetra(ethylene glycol)dithiol at neutral pH (Figure 2.3.4e). Again, the spectral blue-shift occurred slowly, consistent with the neutral thiol results, but no obvious aggregation occurred. Interestingly, both AuBP and AuNS peaks shifted simultaneously, indicating non-selective functionalization that was not previously observed. An assembly reaction performed using glutathione as a control (Figure 2.3.4f) developed the expected spectral features, indicating the specific effectiveness of the amino acid. To test this, an assembly was performed using cysteine, with the results shown in Figures 2.3.3a,b. With cysteine, the reaction exhibited the immediate AuBP LSP blue-shift, as well as better resolved spectral features than those observed with glutathione. Thus, for the remainder of the work, cysteine was used as

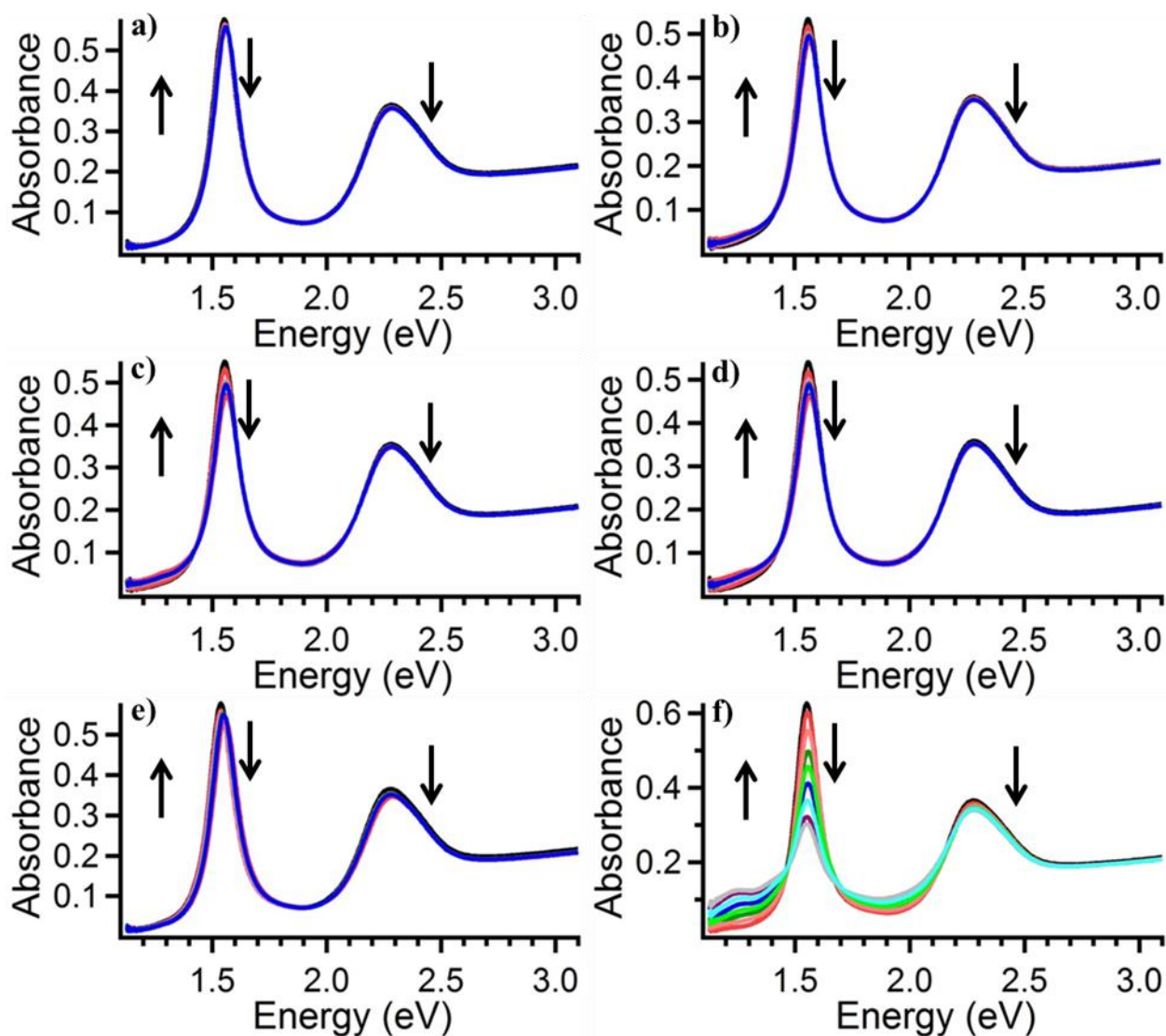


**Figure 2.3.4** Comparison of assembly reactions performed using different thiol linking molecules. a) 3-MPA at pH=9 b) Cysteamine at pH=3 c) 3-MPA at pH=3 d) Mercaptoethanol at pH=3 e) Tetra(ethylene glycol) dithiol at pH=7 f) Glutathione at pH=3. All reactions were monitored for one hour, and the arrows indicate how the spectra evolve with time. As can be seen, no other linker developed similar features to those observed with glutathione.

the linker, and the UV/Vis spectra of the reactions used for characterization are presented as Figures 2.3.3c,d. These results confirm the specific role of zwitterionic amino acids in aqueous

AuNP assembly, which most likely occurs through the two-point electrostatic interaction previously proposed.<sup>64,78</sup> However, our results do not support the idea that the glutathione or cysteine linkers preferentially bind to AuBP tips.

The rapid drop of the AuBP LSP at ~1.6 eV and only a slight decrease in the AuNS resonance at ~2.3 eV in all of the cysteine and glutathione reaction spectra indicate a preference for AuBP aggregation that has not been previously reported. To confirm this, an aliquot of the reaction mixture was spincast onto the ITO-glass substrates at the final time point in Figure 2.3.3d, and one of its 100  $\mu\text{m}$  x 100  $\mu\text{m}$  grids was completely SEM imaged (198, 6  $\mu\text{m}$  x 6  $\mu\text{m}$  images). The results are shown in Table 2.3.1. The region contained over 3000 particles, with a ~30% AuBP and ~70% AuNS distribution, which is typical of a AuBP synthesis.<sup>6</sup> There were 163 total dimers, and 21, 6, 2, and 1 trimers, quadrimers, pentamers and hexamers, respectively.

27% of the AuBPs were taken up in assembly, compared to only 4% of the AuNSs, which can be assigned to a factor of 6 in their relative ‘reactivity,’ and is in fair agreement with the peak amplitude changes in Figure 2.3.3d. We note that no dimers were observed when substrates of the diluted stock colloid without the linker were made (not shown), indicating that the linking molecule, and not solvent evaporation,<sup>24,74</sup> is the cause of the dimerization. A non-specific dimerization would yield structural ratios of: AuBP-AuBP: 1, AuBP-AuNS: 4.7, and AuNS-AuNS: 5.4, while the measured ratios were: AuBP-AuBP: 1, AuBP-AuNS:  $1.21 \pm 0.12$ , and AuNS-AuNS:  $0.16 \pm 0.13$ , with errors from the counting statistics. These results can be interpreted as the AuBPs being about five times more likely to aggregate than the AuNSs, as this would yield ratios of 1:0.93:0.22. The consistency of these results leads us to conclude that the AuBPs are about 5-6 times more ‘reactive,’ i.e., more likely to assemble, than AuNSs, which further supports the picture of a less stable CTAB bilayer at regions of sharp curvature guiding anisotropic AuNP

**Table 2.3.1 Complete AuBP Dimer Particle Count**

AuBP- AuBP	AuBP- AuNS	AuNS- AuNS	Trimer	Quadramer	Pentamer	Hexamer	Oligomer	AuBP	AuNS
69	83	11	23	6	3	1	0	800	2358

assembly.<sup>64,78</sup>

From the SEM images, the AuBP dimers can be subdivided into three structural categories: 28 bowtie, 14 longitudinal edge-edge, and 27 V-shape dimers (Table 2.3.2). To optically characterize these structures, 59 AuBP dimers were isolated using both DF and SEM, with the results presented in Figures 2.3.5 and 2.3.6. Figure 2.3.7 outlines the DF and SEM matching process for the representative bowtie dimer of Figure 2.3.5a. The bowtie dimers range from tip to tip (Figure 2.3.5a) to structures whose tips overlap by no more than half the facet length (Figure 2.3.5b). They exhibit the most red-shifted resonances, with a distribution from 1.25 to 1.4 eV (1.30 eV average, Figure 2.3.5c), and the majority of the structures have less than 10 nm of interparticle overlap (Figure 2.3.5d). The longitudinal edge-edge dimers have a less red-shifted resonance, centered at 1.40 eV (Figure 2.3.6a), while the V-shape AuBP dimer structures have a distinctly blue shifted plasmon resonance centered at 1.74 eV (Figure 2.3.6b). With the lone AuBP LSP on the substrate entered at  $1.62 \pm 0.017$  eV, these resonances are a  $\sim 7\%$  blueshift for the V-shape, a  $\sim 14\%$  redshift for the edge to edge, and a  $\sim 20\%$  redshift for the bowtie dimers.

The polarization dependent spectra (Figure 2.3.8a) of the AuBP dimers and their preservation of lone AuBP full width-half maximum (FWHM) (Figure 2.3.8b) indicate that their resonances are a single, new mode, determined by the coherent coupling between the plasmon resonances of their component NPs.<sup>28,74,85-94</sup> This matches the qualitative expectation from a simple dipole-dipole coupling model, where dipoles aligned end to end yield an optical red-shift, like the bowtie and longitudinal edge-edge structures, while dipoles aligned side to side yield an

**Table 2.3.2 AuBP Dimer Type Analysis**

Type	Bowtie	Longitudinal Edge-Edge	V-Shape
Counts	28	14	27
Ratio, per lone AuBP	0.035	0.018	0.034

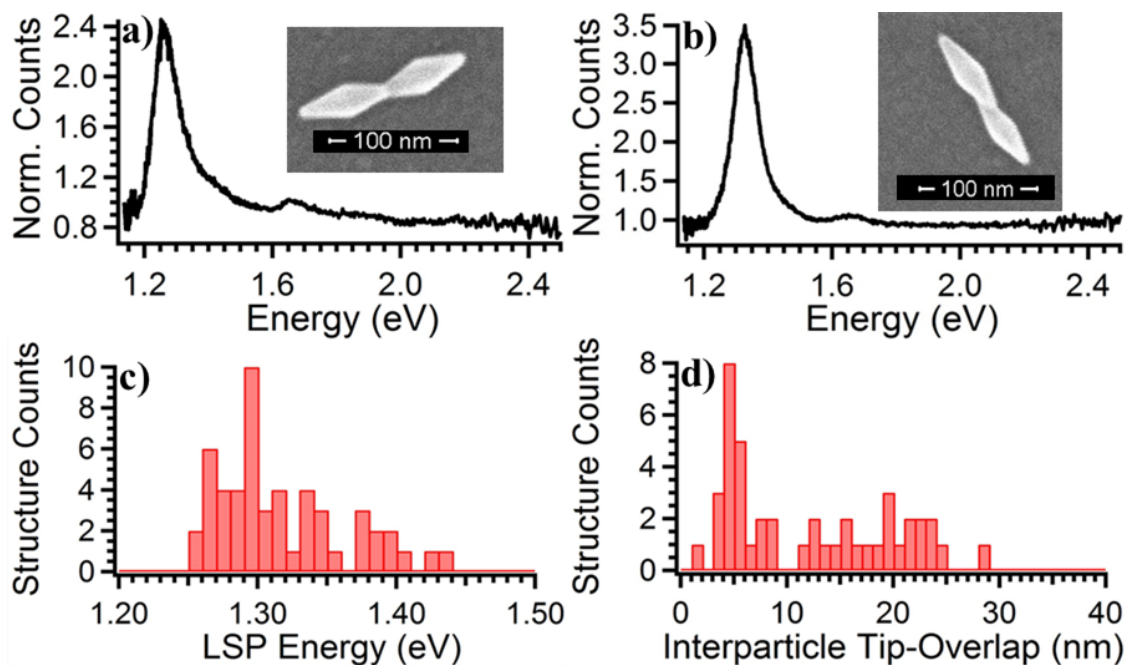


**Figure 2.3.5** Characteristic DF spectra and SEM images of bowtie AuBP dimers. a) Tip to tip and b) tip overlap structures. The counts are normalized to the lamp spectrum. c) Histogram of the plasmon resonances of the bowtie structures. The bin widths are 0.01 eV. d) Histogram of the tip overlap of all bowtie structures. The bin widths are 1 nm.

optical blue-shift, like the V-shape dimers. Even though the HRSEM and HRTEM (Figure 2.3.9) images of some of the bowtie structures seem to show interparticle overlap, we do not believe that a charge transfer plasmon (CTP) causes their plasmon resonances.<sup>24,25,85,95</sup> The bowtie spectra have a similar  $\Delta E/E$  shift to Shao et al.'s for their gapped nanobipyramids,<sup>25</sup> and the HRTEM images of AuBP dimers oriented perpendicular to the beam path show a small interparticle gap (Figure 2.3.9). These factors indicate that the overlap does not correspond to the particles fusing together,

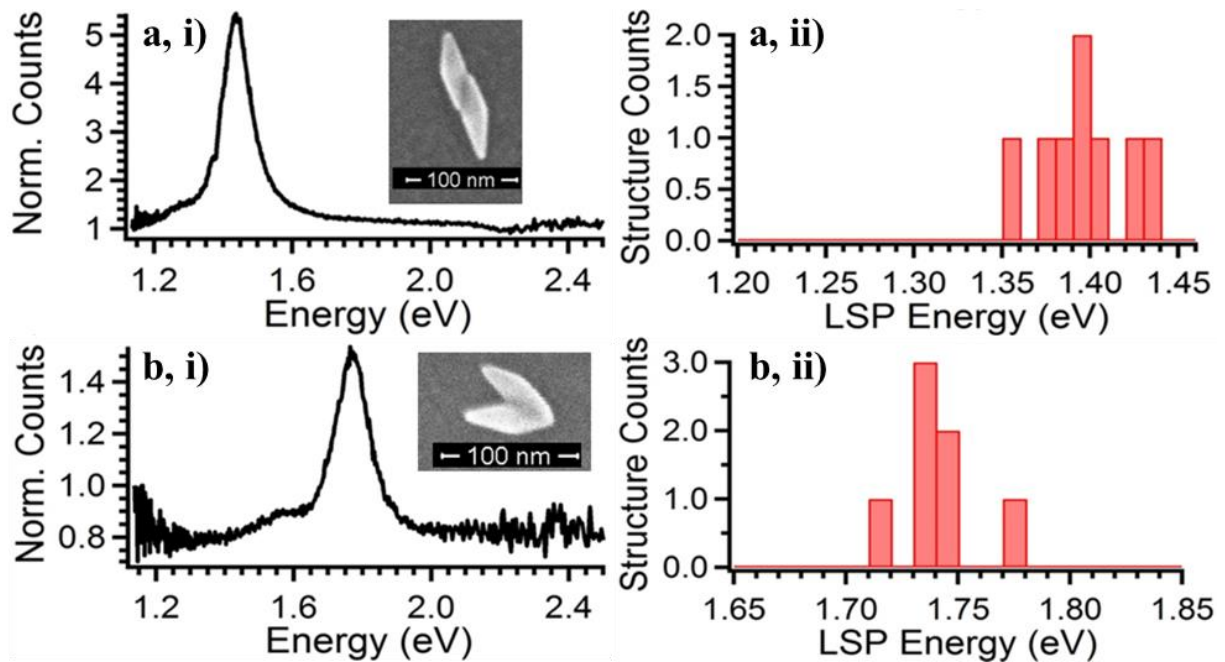


**Figure 2.3.6** Characteristic DF spectra and SEM images of a,i) longitudinal edge-edge and b,i) V-shape dimers. The counts are normalized to the lamp spectrum. Histogram of the a,ii) longitudinal edge-edge and b,ii) V-shape structures' plasmon resonances. The bin widths are 0.01 eV.

but is rather an issue of orientation on the substrate.

To elucidate the relationship between the AuBP dimers' resonances and the coupling between their individual AuBPs, the resonances were divided into two groups and plotted against the component AuBPs' center to center distance. The V-shape dimers (Figure 2.3.10a) display no relationship with particle separation, indicating that their shape is the factor that determines their resonance. The bowtie and longitudinal edge-edge dimers, however, exhibit a slight negative relationship between their plasmon resonances and the straight-line distance between the centers of their individual AuBPs (Figure 2.3.10b). The resonance energy is minimized for structures whose center to center separation corresponds to <10 nm of tip overlap (60-70 nm of center to center separation), indicating that the coupling strength between the particles increases as their

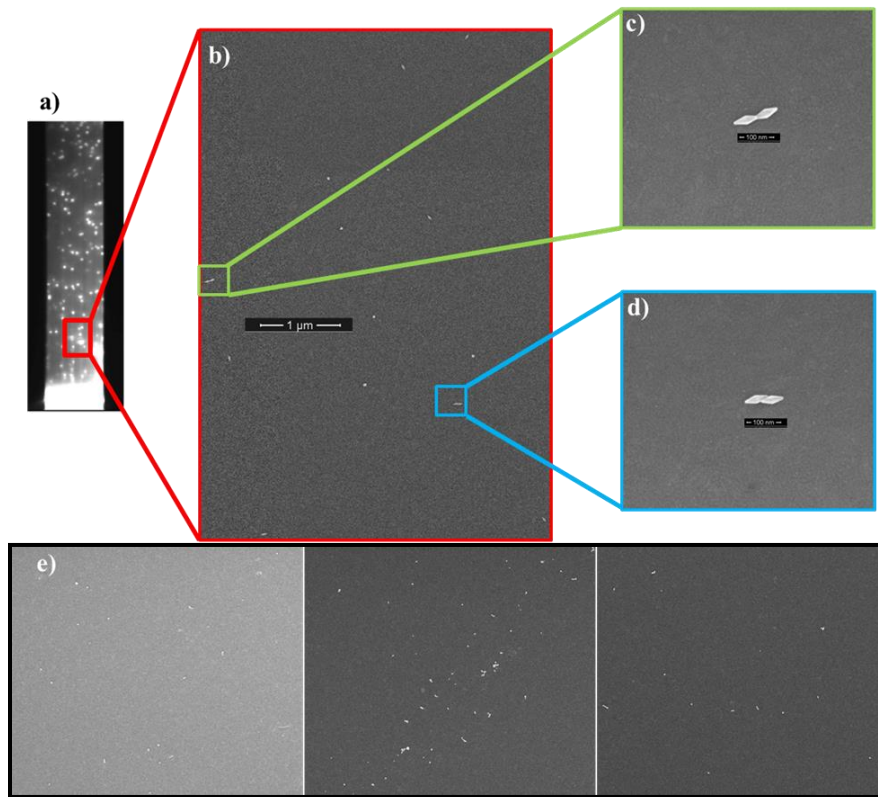


**Figure 2.3.7** a) – d) DF and SEM matching process for the bowtie dimer of Figure 2.3.5a, and nearby longitudinal edge-edge dimer. a) The DF image collected from the CCD camera. The vertical distance is  $\sim 100 \mu\text{m}$ . From this image, a region of interest is identified for SEM mapping. b) The low resolution mapping of the region of interest outlined in a). Multiple SEM images of this region were taken and stitched together using the Gimp 2.8 software package. Then, the DF and SEM images were compared to match the scatterers and their plasmon resonances with their structures. c) and d) Full, high resolution SEM images of the bowtie dimer in Figure 2.3.5a and the nearby longitudinal edge-edge dimer, respectively, after the matching process and plasma cleaning. The only DF scatterers are the AuBPs, since our lamp source is coated in gold to decrease its emission for  $< 550 \text{ nm}$ . e) SEM images of attempts to increase AuBP dimers surface density by multiple depositions. As can be seen, very few dimers are observable, while there are many trimers and other higher order aggregates present.

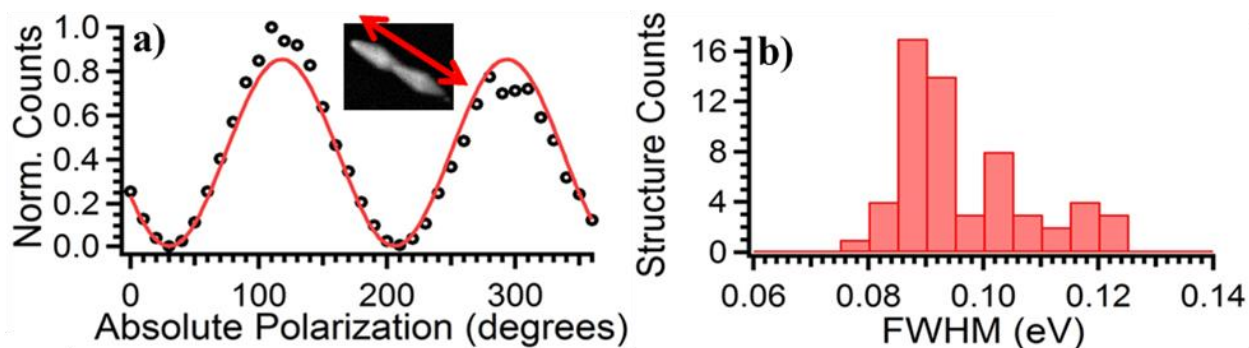


**Figure 2.3.8** a) Polarization dependence of a representative bowtie dimer's spectrum, where  $0^\circ$  polarization corresponds to vertically aligned light. The arrow in the SEM inset shows the direction of polarization of the dimer's plasmon resonance. The counts are normalized to the maximum value. b) Histogram of the FWHM of the optical spectra of the identified AuBP dimers. The average value is 0.0965 eV, and the bin width is 0.005 eV.

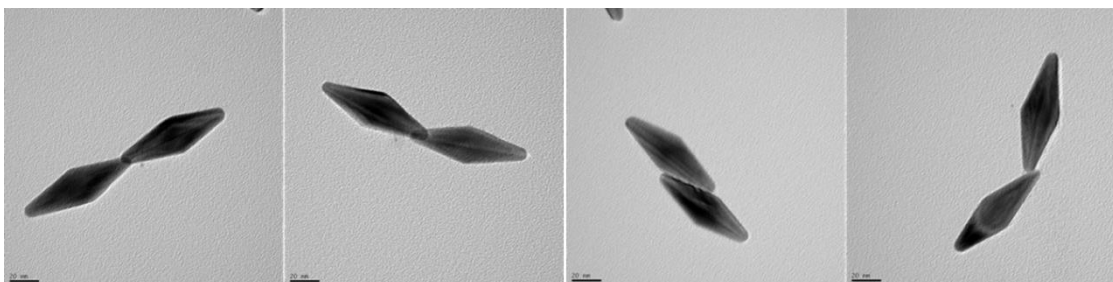


**Figure 2.3.9** Representative TEM images of AuBP dimer structures. The left two images demonstrate dimers with slight interparticle overlap, and the right two images show structures with an interparticle gap.

component AuBPs become more linearly aligned.

Having structurally and optically characterized the AuBP dimer types, the spectral features of the reaction mixture were analyzed to see if there was any relationship with the specific structures.<sup>29</sup> The average AuBP LSP of 1.62 eV on the ITO is a 0.02 eV blue-shift of its post-

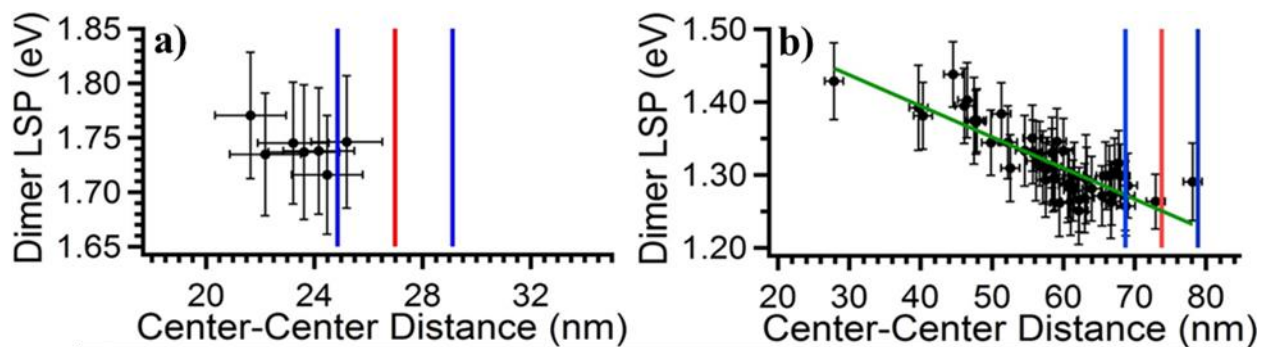


**Figure 2.3.10** The AuBP dimer resonances plotted as a function of the straight-line, center to center distance between their component particles. a) V-shape dimer resonances, which did not exhibit any dependence. b) Bowtie and longitudinal edge-edge resonances. The green line is the linear fit with  $r^2 = 0.71$ . In both graphs, the vertical error bars are the FWHM of the optical spectra and the horizontal error bars are  $\pm 1$  standard deviation in the size of the particles, as measured from HRSEM images. The red line marks the position of the average size parameter of interest (the AuBP a) width and b) length), and the blue lines are  $\pm 1$  standard deviation in the average measurement of each, as determined from the HRSEM images.

linker maximum in solution. This shift is caused by the change in the dielectric environment experienced by the AuBPs and has been studied previously.<sup>50</sup> The exact relationship developed by Burgin et al. cannot be applied to the current work because of the thin layer of surfactant and water that influences the particles' local dielectric environment.<sup>96</sup> The principle of linearity still applies, however, and if it is assumed that every structure on the substrate experiences a similar local environment, then this 0.02 eV blueshift is a correction factor. Thus, the spectra of Figures 2.3.3c,d were analyzed, with the results provided in Figure 2.3.11 and Table 2.3.3. The bowtie dimers' corrected DF and solution peaks match at 1.28 eV, and the correlation for the longitudinal edge-edge and V-shape dimers falls well within the 0.1 eV FWHM of the dimer structures (1.38 eV vs.

1.43 eV and 1.72 eV vs 1.74 eV, respectively). These results mean that the UV/Vis peaks that arise during the assembly reactions can be assigned to specific structures and their in situ development can be monitored (Figure 2.3.12a,b). To the best of our knowledge, no such correlation has been previously reported.

Notably, the V-shape dimer peak  $\sim 1.74$  eV does not develop until late in the fitted spectra of Figure 2.3.3c (Figure 2.3.12b). It is completely absent in the fitted spectra of Figure 2.3.3d (Figure 2.3.11), even though it should be present in almost the same intensity as the bowtie dimer peak from the particle counting results (Table 2.3.2). In fact, only the bowtie dimer peak at 1.27 eV and the AuBP peak at 1.60 eV can be identified at the final time point spectrum in the assembly of Figure 2.3.3d. These peaks have a bowtie to AuBP area ratio of 0.11, but since the bowtie dimers should have about twice the optical cross section of the individual particles, they should have a concentration ratio of  $\sim 0.055$ . From the counting results, the dimer to AuBP ratios are 0.035, 0.018, and 0.034 for the bowtie, longitudinal edge-edge, and V-shape structures respectively. The over-representation of V-shape dimers can be explained as the result of the capillary forces exerted on the particles during the drying process, which could be strong enough to fold some of the bowtie dimers to into the more compact V-shape. If it is assumed that all of the V-shape from the particle counting are the result of such folding, then the bowtie to AuBP ratio would be 0.069, close to expected value of 0.055, supporting the bowtie dimer domination at early assembly times. These results could be confirmed through a cryo-TEM analysis of the reaction mixture.

From the Beer-Lambert Law, absorption spectra changes can be used to extract information about a reaction's kinetics. Figure 2.3.12b is the time evolution of the fitted peaks of Figure 2.3.3c, from which the AuBP LSP peak decrease can be analyzed for the kinetics of aggregation.<sup>29</sup> The 'bimolecular' diffusion limited rate,  $k_d$ , is calculated as

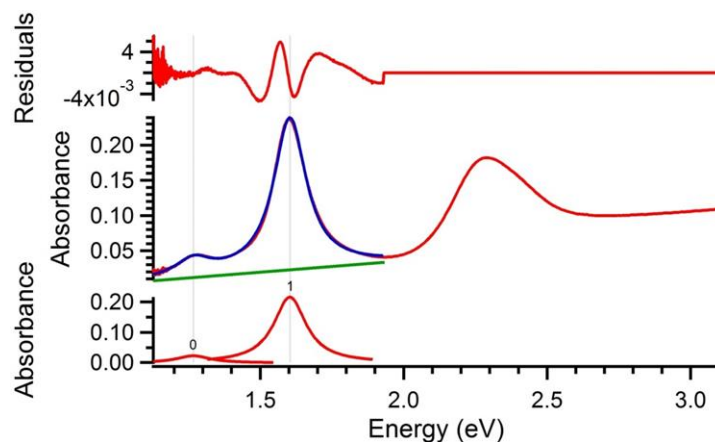


**Figure 2.3.11** Analysis of final time UV/Vis spectrum of Figure 2.3.3d, demonstrating the solution UV/Vis feature analysis. All reaction spectra from Figure 2.3.3c,d text were fitted using Igor's Multippeak routine, with a linear baseline for the regions of 1.1 eV to 1.93 eV. The average solution peak locations are provided in Table 2.3.3.

**Table 2.3.3 AuBP Dimer DF and UV/Vis Spectral Matching Results**

Dimer Type	Average DF Resonance	Corrected Resonances	Solution Peak Locations
Bowtie	1.30 eV	1.28 eV	1.28 eV
Longitudinal Edge-Edge	1.40 eV	1.38 eV	1.43 eV
V-Shape	1.74 eV	1.72 eV	1.74 eV

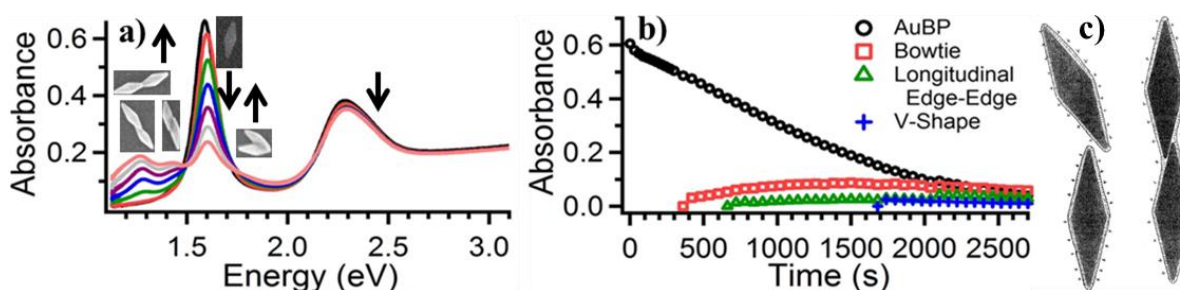


**Figure 2.3.12** a) The UV/Vis reaction spectra from Figure 2.3.3c matching the peaks in the reaction mixture with their corresponding structures. The arrows indicate how the spectra evolve with time. b) The absorbance changes of the fitted peaks over time. c) Cartoon of the intermediate and dimers to explain the apparent first order kinetics discussed in the text.

$$k_d = \frac{8kTC_0}{3\eta} \quad (1)$$

where  $C_0$  is the initial concentration,  $k$  is Boltzmann constant,  $T$  is the temperature and  $\eta$  is the viscosity. Using  $\eta = 10^{-3} \text{ kgm}^{-1}\text{s}^{-1}$  and the estimated  $C_0 = 30 \times 10^{-12} \text{ M}$ , this gives  $k_d = 0.2 \text{ s}^{-1}$ . Thus, most AuBPs have encountered another AuBP after  $\sim 5 \text{ s}$ . However, the assembly clearly takes place on a 1000 s time scale, meaning it is not in the diffusion limit. We also note that the AuBP LSP's rate of disappearance increases with time, which obviously contradicts second order reaction kinetics. Attempting to plot the reaction kinetics as described elsewhere illustrates the discrepancy (Figure 2.3.13a).<sup>17</sup>

Our results are better fit using first order kinetics and a rate that increases with time (Figure 2.3.13b). This is in contrast with previous reports of AuNR assembly using thiols in an acetonitrile-water mixture, where the assembly kinetics are explained with an incubation period, assigned to the thiol linkers binding to the AuNRs, followed by a period of second order kinetics.<sup>16,29</sup> The quick adsorption of the amino acid linkers to the AuBPs' surfaces previously discussed means our assembly will not exhibit a similar incubation period, but it does not address the absence of second order kinetics. To explain this, we propose that the AuBPs quickly form dimer intermediates, but that these do not interact strongly enough to shift their plasmon resonances. Such structures would have a first order rate, however, to transform into the dimers seen in the spectroscopy and SEM. A possible scenario is that the intermediate dimers, formed at the rate of the diffusion limit, must first align end to end. Due to the interaction between the zwitterionic amino acids and the less stable CTAB bilayer at regions of high curvature, these regions would be less positively charged than the rest of the AuNP and would have reduced interparticle repulsion. In such a temporary alignment, a nucleated defect of the bilayers at the tips could lead to bilayer fusion, as illustrated in the cartoon of Figure 2.3.12c. This would be followed by the electrostatic two-point attachment

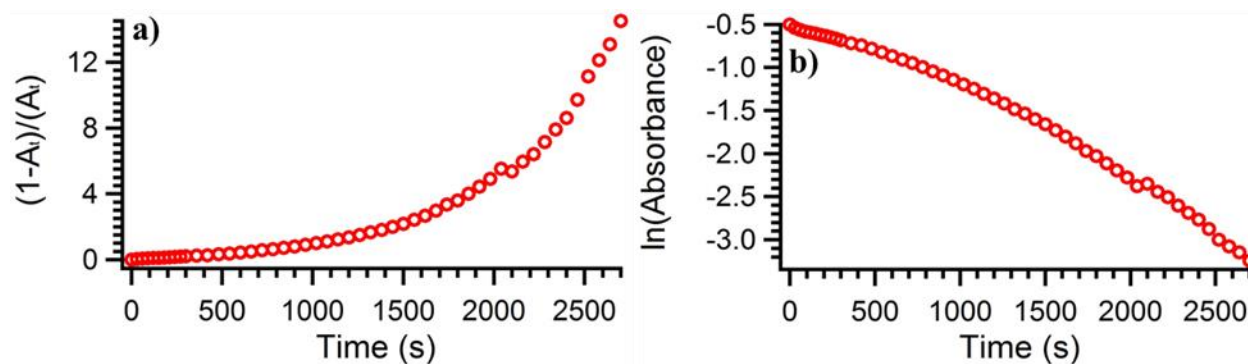


**Figure 2.3.13** Attempted fittings of reaction kinetics. a) Second order, as described by Wang et al.<sup>29</sup> b) First order. The more linear relationship in b) indicates that the reaction is more closely exhibits first order, as opposed to second order, kinetics.

of the amino acid groups, which is the first-order rate limiting step. This explains the spectral feature evolution at early times, where the bowtie dimers dominate. The slight increase with time of the rate constant in Figure 2.3.12b and Figure 2.3.13b can then be explained by the gradual degradation of the bilayer facilitating the fusing. As observed in the spectra, the longitudinal edge-edge structures could then develop as the AuBPs slip past each other to maximize their surface linking interactions. We think that the direct formation of the V-shape structure is unlikely due to the electrostatic repulsion from the sides of the bilayers. It is also an unlikely evolution from the edge to edge dimers, since the surface contact would not increase and the fused bilayer would have become more distorted. However, at long times, a tip to tip dimer could fold into the V-shape as the bilayer continues to destabilize. The small but non-negligible reactivity of the AuNS at early time is assigned to the presence of sharp protrusions on some of the spheres. From Figure 2.2.2, many AuNSs are actually multiply twinned and some exhibit sharp protrusions. Such regions would have CTAB bilayer instabilities similar to those of the AuBPs, which should allow similar

binding interactions to occur. The noted preference for AuBP assembly over AuNS assembly, however, indicates that this is not as strong of an effect.

## **2.4 Conclusion**

In summary, we have developed an aqueous methodology to synthesize AuBP dimers, with specific emphasis on their bowtie orientation. Such a structure is an interesting building block for future field enhancement and non-linear optical studies. The effectiveness of the amino acids glutathione and cysteine were evaluated, as well as the importance of the aromatic additive 5-BSA. The 5-6 fold increase in the AuBPs' 'reactivity' over the AuNSs was also quantified. The AuBP dimers were structurally and optically characterized, and a general relationship between their geometry and plasmon resonance was determined.

From these results, we found that the spectral features of the assembly reactions correspond to the plasmon resonances of specific dimers. Such a result has not been previously reported, and means that these reactions can be monitored in situ for specific structures. Finally, the kinetics of assembly were analyzed, and we determined that they do not correspond to a second order model. Instead, the results seem close to first order, suggesting that the assembly occurs through some intermediate structure.

## **2.5 Post-Publication Notes**

There are a few items relating to the AuBPs that are worth addressing before moving to the next chapter. First, the tweezers used to hold the TEM grids can be contaminated with dried particles that will re-deposit on other grids. This caused quite a bit of unfounded excitement at one point, when I thought I'd managed to synthesize silver bipyramids (Figure 2.5.1a). Second, the dilute

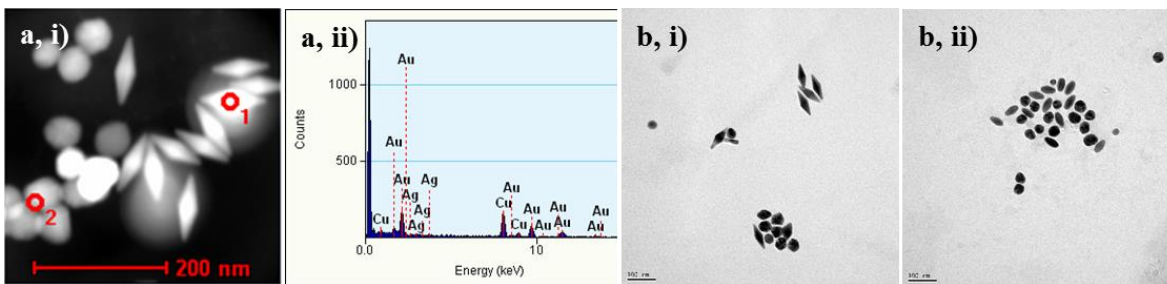


**Figure 2.5.1** a,i) High angle annular dark field TEM image of silver nanospheres and tweezer deposited, AuBP contaminants. a,ii) Energy dispersive x-ray data of point 1 in a,i), confirming the AuBP's presence. b) TEM images displaying the occasional rounding effect.

AuBP aliquots used for TEM analysis will occasionally show severely rounded CTAB coated AuBPs. Preparing a new aliquot from the stock colloid yields the correct particles. Somehow, diluting the stock by an order of magnitude allows AuBPs oxidization (Figure 2.5.1b).

# **Chapter 3. End-to-End Alignment of Gold Nanorods on Topographically Enhanced, Cylinder Forming Diblock Copolymer Templates and their Surface Enhanced Raman Scattering Properties<sup>22</sup>**

*This paper was originally published in The Journal of Physical Chemistry C on August 13<sup>th</sup>, 2014, and is adapted with permission here: Tong, Q.;\* Malachosky, E. W.;\* Raybin, J.; Guyot-Sionnest, P.; Sibener, S. J. End-to-End Alignment of Gold Nanorods on Topographically Enhanced, Cylinder Forming Diblock Copolymer Templates and Their Surface Enhanced Raman Scattering Properties. J. Phys. Chem. C **2014**, 118 (33), 19259–19265. Copyright 2014 American Chemical Society.*

Collaborators: Dr. Qianqian Tong, Jonathan Raybin, Prof. Steven J. Sibener

Special thanks to: Dr. Justin Jureller

This chapter is my second project, and my first co-authored paper. Here, we present a facile methodology for the end-to-end assembly of gold nanorods of various aspect ratios on corrugated, horizontal, cylinder-forming diblock copolymer templates. Although the depth of corrugation is significantly smaller than the diameter of the nanorods, they exhibit excellent selectivity (>98%) and alignment for placement in the polymer grooves due to capillary forces and the substrate's topography. Enhanced corrugation of the diblock template is achieved by chemical swelling prior to deposition of the metallic nanorods. Graphoepitaxy of the diblock copolymer in nanoconfining

channels is employed to achieve essentially perfect long range orientation of the substrate, while subsequent deposition of nanorod arrays whose alignment maps onto that of the diblock template with high fidelity provides novel organic-inorganic hybrid surfaces whose surface enhanced Raman spectroscopy (SERS) properties are characterized. These arrays of aligned gold nanorods exhibit polarization dependent spectra for adsorbed molecular species with a 24-fold enhancement in signal intensity when the trenches are aligned with parallel versus perpendicular orientation with respect to the incident polarization of the excitation laser. The simple construction of these systems and their unique SERS properties provide a new and efficacious platform for the construction of functional nano-devices.

### **3.1 Introduction**

Thin films of nanoparticles (NPs) have attracted considerable attention due to their potential applications related to electronic devices,<sup>97,98</sup> magnetic storage,<sup>99</sup> and sensors.<sup>100,101</sup> Investigations into the last category have focused on noble metals NPs, due to their well-documented surface enhanced Raman spectroscopic (SERS) properties.<sup>11,101,102</sup> Gold NP (AuNP) SERS systems are typically fabricated using either top down or bottom up techniques, where the regions of electric field enhancement, called hot spots, are made by electron beam lithography (EBL)<sup>103,104</sup> or ion-beam sputtering,<sup>105</sup> or through the deposition of colloiddally synthesized AuNPs. Controlling the deposition of colloidal AuNPs is attractive because the locations of the hot spots are determined by the order and alignment of the AuNPs on the substrate. This has been done by chemically functionalizing<sup>106-109</sup> or patterning<sup>107,110-115</sup> the substrates, or by modifying the AuNP colloid.<sup>116-</sup>

This paper presents a facile, bottom up technique that produces highly ordered arrays of colloidal gold nanorods (AuNRs) aligned end-to-end with favorable and polarization-dependent SERS properties. AuNRs have received particular attention due to their controllable syntheses,<sup>4,5,14,119,120</sup> tunable plasmon resonances,<sup>17</sup> and electromagnetic field enhancements,<sup>15</sup> making these NPs<sup>11</sup> and their assemblies<sup>102</sup> of interest for SERS.<sup>102,115,118</sup> Coupling between plasmonic NPs makes AuNR assemblies exhibit stronger hot spots than the individual structures and increases the SERS response,<sup>102</sup> as documented for AuNR chains<sup>116,121,122</sup> and various large-scale, 2D and 3D AuNR aggregates.<sup>23,115,118</sup>

The AuNR arrays presented in this paper are made by depositing AuNR colloids onto silicon-nitride substrates patterned with horizontal, cylinder-forming polystyrene-*block*-poly(methylmethacrylate) (PS-*b*-PMMA) block copolymer (BCP) templates. BCP templates are attractive platforms because they self-assemble into spheres, lamellae, cylinders, and other well-ordered microdomains easily and cost effectively, and can achieve long range, defect-free structures.<sup>123–126</sup> BCP microdomains are also comparable in size to colloiddally synthesized NPs (5 nm to 50 nm).<sup>127</sup>

NP ordering and alignment when mixed in BCP systems has been demonstrated previously for AuNRs in PS-PMMA, where the NRs modified by polyethylene glycol are fully embedded inside the PMMA domain.<sup>128</sup> Semiconductor nanorods have also been successfully embedded into BCP designed with appropriate interactions.<sup>76</sup> While bulk alignment is of interest, surface assembly has the advantage of giving chemical access to the particle surface. While the surface assembly of nanoparticles in specific domains has not yet been very successful when based solely on the surface chemical or wetting characteristics, it has been demonstrated that an enhanced corrugation helps. FePt NPs ordering at the surface of cylinder forming PS-PMMA domains was

first demonstrated using UV enhanced corrugation.<sup>129,130</sup> Plasma etching of a lamellar PMMA domain has also been examined, allowing alignment of gold nanorods with significant order.<sup>111</sup> Solvent swelling of lamellar PMMA in acetic acid vapor has also been applied to several nanoparticle systems, including ZnO nanorods.<sup>131</sup> This present work shows that a similar acetic acid swelling of PMMA in horizontal cylinder PS-PMMA microdomains can be used with great success to align gold nanorods even though the corrugation is less than half of the prior work involving lamellar PS-PMMA. Moreover, we demonstrate such hierarchical assembly for nanoconfined, highly aligned, and essentially defect-free cylindrical diblock substrates.

Although the BCP corrugation is significantly smaller than the particle diameter, excellent alignment is readily achieved for single and individual chains of end-to-end aligned AuNRs. It is herein demonstrated that the combination of graphoepitaxy of the diblock substrate in nanoconfining channels to produce essentially perfect diblock orientation coupled with the subsequent deposition of nanorod arrays whose alignment maps onto that of the diblock template with high fidelity is a highly efficacious route to the formations of spatially anisotropic SERS platforms.

### **3.2 Experimental Methods**

The corrugated block copolymer thin films were fabricated on silicon nitride ( $\text{Si}_3\text{N}_4$ ) substrates purchased from Virginia Semiconductor, Inc., which had been cut to  $\sim 1$  cm x 1 cm, cleaned with toluene, acetone, and methanol using an ultrasonic cleaner, then dried with nitrogen. The substrates were spincoated with 77 kg/mol, 29 wt % PS-*b*-PMMA BCP, purchased from Polymer Source, Inc. and was used without further purification, in 0.9% toluene solution at 4000-5500 rpm for 60 s, and then annealed at 523 K under an Ar for an hour. The phase separated BCP thin films were

then exposed to saturated acetic acid vapor for 15 minutes to induce the selective swelling of the PMMA cylinder domains (Figure 3.2.1). For the substrates created by graphoepitaxy, the 500 nm wide, 20  $\mu\text{m}$  long, and 50 nm deep trenches were patterned into the substrate with EBL using a Hitachi 2700 SEM operating at 300  $\mu\text{C}/\text{cm}^2$  before being coated with BCP. The polymer substrates were imaged by atomic force microscopy (AFM), using an Asylum Research's MFP-3D AFM performed in AC (tapping) mode with Olympus AC240TS cantilevers with a spring constant of 2 N/m.

The AuNRs used in this study were synthesized using a scaled down and slightly modified version of the protocol developed by Ye et al,<sup>14</sup> using the same materials as given in Chapter 2. Benzenethiol (BT,  $\geq 98\%$ ) was purchased from Sigma Aldrich and used without further purification. In all cases, the AuNR seeds were synthesized by dissolving 364 mg of CTAB in 10 mL of  $\text{NPH}_2\text{O}$  at 30  $^\circ\text{C}$  and under vigorous stirring, then adding 250  $\mu\text{L}$  of a 10 mM  $\text{HAuCl}_4$  solution and 600  $\mu\text{L}$  of a fresh, 10 mM  $\text{NaBH}_4$  solution. The solution promptly turned yellow-brown, and was vigorously stirred for two minutes before being set aside. Also, all AuNR colloids were made by dissolving 182 mg of CTAB and 21.9 mg of 5-BSA in 10 mL of  $\text{NPH}_2\text{O}$  at 70  $^\circ\text{C}$  under vigorous stirring, and were then cooled to 30  $^\circ\text{C}$ . For the AuNRs of aspect ratio (AR) 3.05 to 3.20, 96  $\mu\text{L}$  of a 10 mM  $\text{AgNO}_3$  solution, 500  $\mu\text{L}$  of a 10 mM  $\text{HAuCl}_4$ , 51.2  $\mu\text{L}$  of a fresh, 100 mM Vitamin C solution, and 16  $\mu\text{L}$  of the AuNR seed solution were added to the solution. For the AuNRs of AR 4.02, 384  $\mu\text{L}$  of a 10 mM  $\text{AgNO}_3$  solution, 500  $\mu\text{L}$  of a 10 mM  $\text{HAuCl}_4$ , 500  $\mu\text{L}$  of 1M HCl, 51.2  $\mu\text{L}$  of a fresh, 100 mM Vitamin C solution, and 16  $\mu\text{L}$  of the AuNR seed solution were added to the solution. For the AuNRs of AR 6.33, 384  $\mu\text{L}$  of a 10 mM  $\text{AgNO}_3$  solution, 500  $\mu\text{L}$  of a 10 mM  $\text{HAuCl}_4$ , 500  $\mu\text{L}$  of 1M HCl, 25.6  $\mu\text{L}$  of a fresh, 100 mM vit-C solution, and 16  $\mu\text{L}$  of the AuNR seed solution were added to the solution. All of the colloids were vigorously

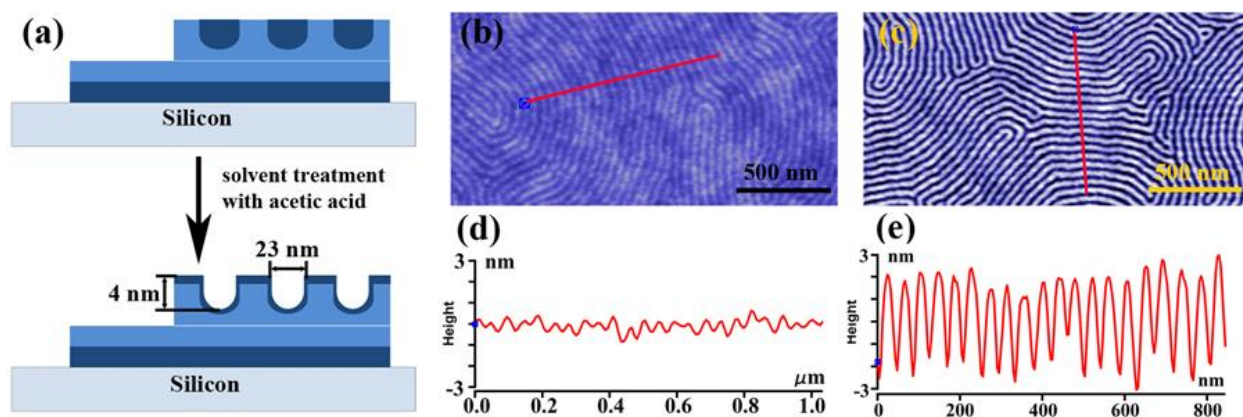


**Figure 3.2.1** (a) Schematic representation of the corrugated, horizontal cylinder-forming PS-*b*-PMMA BCP template fabrication. The dark blue regions correspond to PMMA domains, while the light blue regions correspond to PS domains. (b) – (e) AFM images and topographic height profiles before (b, d) and after (c, e) the acetic acid vapor treatment. The film’s corrugation increases from ~1 nm (d) to ~4 nm (e) after the acetic acid treatment. The height profiles are taken along the arrows in (b) and (c), and the AFM images are 2 μm × 1 μm.

stirred for 30 s, then left to age overnight (15 to 18 hours). All were then hard centrifuged at 8500 *g* and 30 °C for 15 minutes, and had their supernatants decanted and pellets resuspended in 10 mL of NPH<sub>2</sub>O before being centrifuged again under the same conditions. After the second centrifugation, the supernatant was decanted and the pellet resuspended with 250 μL of NPH<sub>2</sub>O. Aliquots of these mixtures were removed for UV/Vis and TEM analysis (Figure 3.2.2). The UV/Vis spectra were recorded on the same Agilent HP 8453 as in Chapter 2, and the TEM images were taken on the new a FEI Spirit TEM operating at 120 kV.

To achieve different surface densities of the same AR AuNRs on the thin, BCP fingerprint films, the AuNR colloid was spincoated for 60 s at 3000 rpm 2, 6, or 10 times, dried in air, then imaged using the Asylum Research MFP-3D AFM. To deposit the AuNRs of different AR onto

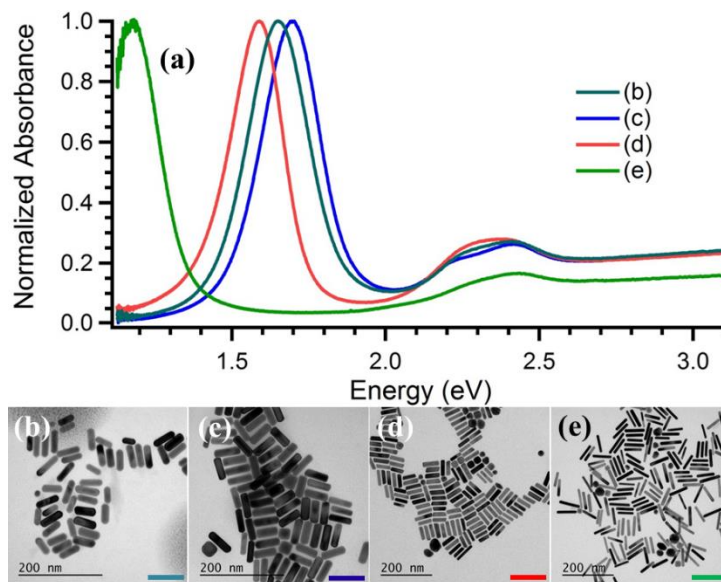


**Figure 3.2.2** (a) UV/vis spectra of the AuNRs used in the paper. Absorbances are normalized to the LSP maximum. (b) TEM images of the Figure 3.3.1 AR 3.05, 20 nm by 61 nm AuNRs. (c) TEM images of the Figure 3.3.2a, AR 3.20,  $58.95 \pm 3.63$  nm by  $18.41 \pm 1.95$  nm AuNRs. (d) TEM images of the Figure 3.2.2b, AR 4.02,  $59.76 \pm 7.26$  nm by  $14.87 \pm 2.00$  nm AuNRs. (e) TEM images of the Figure 3.2.2c, AR 6.33,  $70.50 \pm 7.59$  nm by  $11.14 \pm 1.62$  nm AuNRs.

the thin, BCP fingerprint films, each colloid was spincoated 6 times at 3000 rpm for 60 s, dried in air, then imaged by AFM. For the substrates created by graphoepitaxy, the AuNR colloid was dropcast onto the surface, the excess liquid wicked away, and the substrates dried in air before AFM imaging. This was repeated several times to achieve the desired particle densities. Regions of interest for Raman spectroscopy were also identified at this point.

The SERS characterization of the BCP films with deposited AuNRs were performed with a Horiba LabRam Evolution confocal Raman microscope, using its 785 nm diode laser, NA 0.90 100x objective, 1200 gr/mm, and Andor Synapse CCD detector. For the BCP thin films without AuNRs and with different surface densities of the same AR AuNRs, 20  $\mu$ L of a  $2 \times 10^{-4}$  M BT

solution in ethanol were dropcast onto the substrates, dried, and the Raman spectra recorded with laser power of 14.1  $\mu\text{W}$  for 30 s. The SERS characterization of the graphoepitaxy substrates was performed by dropcasting 21  $\mu\text{L}$  of a  $2 \times 10^{-5}$  M BT solution in ethanol onto the  $0.81 \mu\text{m}^2$  substrates, to ensure the BT monolayer packing of  $0.544 \text{ nmole}/\text{cm}^2$ .<sup>132</sup> The samples were mounted on a rotation stage and manually oriented parallel ( $0^\circ$ ) or perpendicular ( $90^\circ$ ) to the laser's polarization, as determined by using the reflected microscopy optics of the Raman microscope, and the Raman spectra were recorded with a laser power of  $75.5 \mu\text{W}$  for 20 s. The laser was scanned over the sample's surface using the Duoscan capability of the microscope, meaning the beam was moved with mirrors, instead of the sample being moved by the mechanical stage. This helped limit possible issues involving backlash and drift that could have been exacerbated through the use of an after-market rotation stage. All SERS data were recorded using the Horiba LabSpec 6 software, and the peak fits were performed in Igor Pro with background corrected Voigt functions. The 785 nm laser was used for all of the experiments because the 633 nm laser yielded too high of a fluorescent background, caused by the AuNRs.

### 3.3 Results and Discussion

The topographically enhanced, horizontal cylinder-forming PS-*b*-PMMA BCP templates were fabricated by the selective swelling of the PMMA domains in a saturated vapor of acetic acid.<sup>131</sup> Since the PMMA blocks are bound to the PS blocks, their microdomains cannot expand laterally. Instead, the PMMA chains swell and overflow onto the film surface, as shown in Figure 3.2.1a. When the substrates are removed from the solvent chamber, the acetic acid quickly evaporates, causing the PMMA chains to adopt a collapsed conformation and shrink, leaving behind a corrugated surface. Figures 3.2.1b,d are the atomic force microscopy (AFM) images and height

profiles of the BCP films before the acetic acid treatment, and Figures 3.2.1c,e are the AFM images and height profiles of the films after the solvent treatment. As can be seen, the film's height profile increases from ~1 nm to ~4 nm, with a periodicity of ~23 nm, after the acetic acid treatment (Figure 3.2.1e).

To investigate AuNR alignment on these BCP films, 20 nm by 61 nm AuNRs (aspect ratio (AR) 3.05, Figure 3.2.2b) were spincoated onto the templates and imaged by AFM. Low surface density AuNR arrays were made by spincoating the stock colloid twice. The AuNRs were sparsely dispersed over the entire substrate, predominantly existing as isolated particles, with only 45 AuNRs/ $\mu\text{m}^2$  (Figure 3.3.1a). They exhibited a nearly exclusive (>98%, as determined by counting over 800 AuNRs) preference to rest within the fingerprint grooves, where they were aligned along the contours. When the colloid was spincoated 6 times onto the films, the surface density increased to 160 AuNRs/ $\mu\text{m}^2$ , and the AuNRs nearly covered the substrate as a monolayer (Figure 3.3.1b). The AuNRs were still aligned end-to-end along the contours of the fingerprints, resting within the grooves with over 97% selectivity. After 10 spincoatings, the AuNRs formed 3D clusters with >300 AuNRs/ $\mu\text{m}^2$ , and lost the structure of the underlying substrate (Figure 3.3.1c). Increasing the AuNR aspect ratio did not change the alignment results. AuNRs of AR 3.20 (Figure 3.2.2c), 4.02 (Figure 3.2.2d), and 6.33 (Figure 3.2.2e), which varied from 11 nm to 18 nm in width and 59 nm to 71 nm in length, were spincoated onto the BCP fingerprint templates. In all cases, the AuNRs deposited end-to-end in the fingerprint grooves with over 97% selectivity (Figure 3.3.2). Remarkably, the AuNRs of AR 6.33 did not exhibit any side-to-side packing, even though their diameters (11 nm) were a factor of two smaller than the width of the grooves (23 nm) (Figure 3.3.2c). Also, none of the AuNRs exhibited obvious tilting within the polymer grooves, and all were aligned with the pattern's contours.

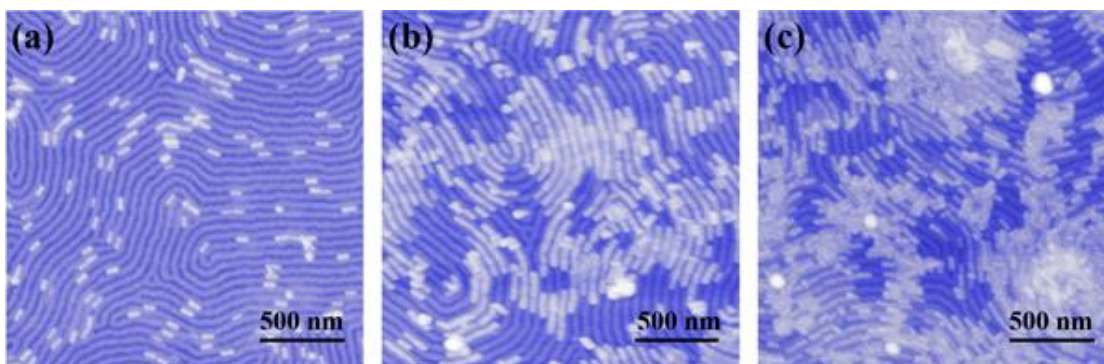


**Figure 3.3.1** AFM images of Figure 3.2.2b AuNRs deposited on the topographically enhanced, horizontal cylinder-forming PS-*b*-PMMA BCP thin films after solvent treatment with acetic acid. The AuNR densities are (a) 45 AuNRs/ $\mu\text{m}^2$ , (b) 160 AuNRs/ $\mu\text{m}^2$ , and (c)  $>300$  AuNRs/ $\mu\text{m}^2$ . The AuNRs are 20 nm by 61 nm, and the images are  $2 \mu\text{m} \times 2 \mu\text{m}$ . The AuNRs in (b) appear larger because an AFM tip with a larger radius was used to record the image.

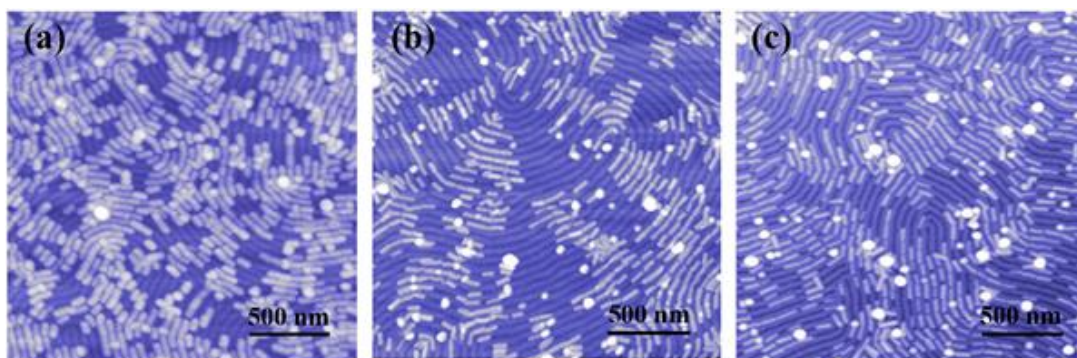


**Figure 3.3.2** AFM images of AuNRs with different ARs on the topographically enhanced, horizontal cylinder-forming PS-*b*-PMMA BCP thin films. (a) AuNRs of Figure 3.2.2c, length  $58.95 \pm 3.63$  nm and width  $18.41 \pm 1.95$  nm, AR = 3.20. (b) AuNRs of Figure 3.2.2d, length  $59.76 \pm 7.26$  nm and width  $14.87 \pm 2.00$  nm, AR = 4.02. (c) AuNRs of Figure 3.2.2e, length  $70.50 \pm 7.59$  nm and width  $11.14 \pm 1.62$  nm, AR = 6.33. All of the AuNRs align in grooves with over 97% selectivity. The images are  $2 \mu\text{m} \times 2 \mu\text{m}$ .

These AuNR deposition results exhibit advantages over previous systems, attributed to our use of cylinder-forming and corrugation-enhanced BCP templates.<sup>107,111,112,131</sup> First, the AuNRs only assemble end-to-end within the template grooves. Second, the AuNRs did not exhibit any obvious deviations from the contours of the grooves. Third, the AuNRs did this even though the BCP templates' height profiles were far smaller than the deposited AuNRs' diameters (ranging in ratio from 1:2.75-1:5). These observations are consistent with a simple model involving the capillary forces exerted on partially immersed rodlike viruses,<sup>133</sup> colloidal particles,<sup>134-138</sup> and the topography of the BCP template<sup>139</sup> (Figure 3.3.3). Because of the aspect ratio of the AuNRs, only the capillary force arising from the contact line along their length is considered.<sup>138</sup> This force

$$F = \gamma 2L \cos(\alpha) \quad (1)$$

is maximized when the particles are half-immersed,<sup>139</sup> where  $\gamma$  is the surface tension of water (72.8 dyn/cm),  $L$  is the length of the rod, and  $\alpha$  is the contact angle of the water at the AuNR's surface. The energy a AuNR gains by moving from a crest to a trough is calculated by integrating over the substrate's corrugation  $h$ , giving an energy of

$$E = \gamma 2Lh \cos(\alpha) \quad (2)$$

(Figure 3.3.3a). For the AuNRs with 61 nm length, and  $\alpha = 30^\circ$ ,<sup>139</sup> the crest to trough energy difference is  $3.08 \times 10^{-17}$  J of energy, four orders of magnitude greater than their room temperature Brownian motion energy of  $4.11 \times 10^{-21}$  J. The strength of the capillary force explains both the AuNRs' extreme preference and the alignment in the grooves. Because the fingerprints are generated from the PMMA cylinder domains, their bottoms are curved (Figures 3.2.1a, 3.3.3a). Therefore, any misalignment in the grooves results in the AuNRs having a vertical displacement. From the equation of the tangent circle describing the curvature of the grooves (radius  $\sim 20$  nm), the thermal energy could only induce a misalignment of  $\sim 0.5^\circ$ .

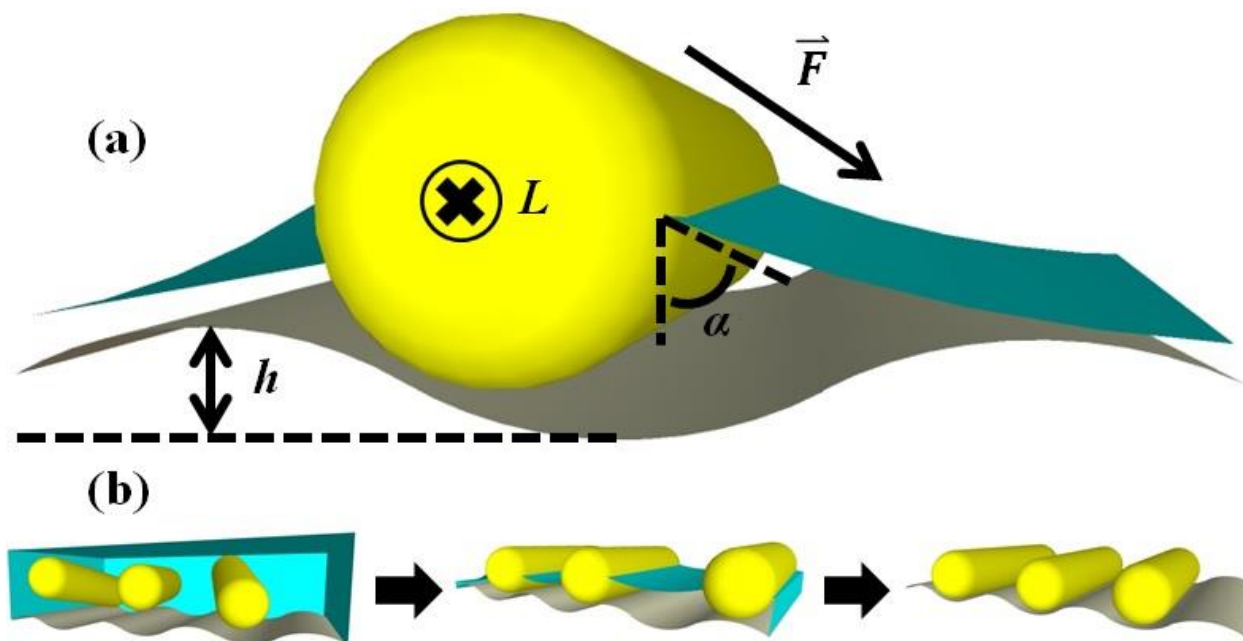


**Figure 3.3.3** Schematic representation of the AuNRs drying on the substrates. (a) Partially immersed AuNR being drawn into a polymer trench. The  $\vec{F}$  indicates the direction of the capillary force. All variables are the same as defined in the text. (b) Schematic representation of the AuNR deposition process, from the fully immersed AuNRs, to the partially immersed particles, to the aligned product.

Thus, the capillary force explains the AuNRs' order, but it does not explain the lack of lateral packing. For the AuNRs with larger diameters (20 nm, 18.41 nm, and 14.87 nm), which are close to the grooves' widths (23 nm), the absence of side-to-side packing could be explained due to geometric confinement. However, this does not address the case of the AR 6.33 AuNRs, whose diameters are about half the channel width. The dearth of horizontal packing is attributed to the electrostatic repulsion between the AuNRs. The colloiddally synthesized AuNRs are coated in a CTAB and 5-BSA bilayer,<sup>14</sup> so each rod can be approximated as having a positive charge,  $q$ , roughly equal to the number of  $\text{CTA}^+$  molecules in its outer layer, as determined by calculating

the AuNR surface area and multiplying by the optimum CTA<sup>+</sup> packing density of 2.44 CTA<sup>+</sup>/nm<sup>2</sup>.<sup>140</sup> The Debye length of the colloid is given by

$$\kappa^{-1} = \sqrt{\frac{\varepsilon_r \varepsilon_0 k_B T}{2 N_A e^2 I}} \quad (3)$$

where  $\varepsilon_r$  is the relative permittivity of water at room temperature,  $\varepsilon_0$  is the permittivity of vacuum,  $k_B$  is the Boltzmann constant,  $T$  is the absolute temperature,  $N_A$  is Avogadro's number,  $e$  is the fundamental unit of charge, and  $I$  is the colloid's ionic strength in mole/m<sup>3</sup>. Using a  $\varepsilon_r$  of 78.54, and a CTAB concentration of 1 mM, the Debye length is 9.62 nm. The electrostatic repulsion for two AR 6.33 AuNRs separated by their Debye length

$$\frac{1}{4\pi\varepsilon_0\varepsilon_r} \frac{|q|^2}{(\kappa^{-1})^2} \quad (4)$$

yields a very large repulsive force of  $1.36 \times 10^{-6}$  N, consistent with the long term stability of the colloidal suspension. Moreover, as long as the particles are fully submerged in solution, they will be separated by at least their Debye length, irrespective of the substrate. As the solvent evaporates, the AuNRs will still be fully immersed, with their interparticle interactions governed by electrostatics. This will keep them well spaced as they come closer to the substrate surface. When enough of the solvent has evaporated such that AuNRs are partially immersed, the capillary forces are strong enough to induce the final assembly on the substrate (Figure 3.3.3b). We believe that end-to-end assembly is favored because of the orientation's reduced electrostatic repulsion in solution, as compared to lateral assembly. We note that if the deposition is formed at higher concentration of the AuNRs, side-to-side and random aggregates appear which we attribute to an increase of the ionic strength as the water evaporates, drastically shrinking the Debye length. Attractive capillary forces can facilitate further the end-to-end assembly of the AuNRs in the channels.<sup>135</sup>

SERS measurements were performed on the samples of Figure 3.3.1 to characterize the enhancement properties of the AuNR films. Benzenethiol (BT) diluted in ethanol was dropcast onto the substrates and dried in air, and the Raman spectra were recorded using the 785 nm laser of a Horiba LabRam Evolution confocal Raman microscope. Spectra recorded from BCP thin films without AuNRs showed no signal, while spectra with intensities that increased with AuNR surface density were recorded from the Figure 3.3.1 substrates (Figure 3.3.4). The selective and reproducible AuNR deposition directed by the BCP microdomains indicated that linear, end to end AuNR arrays of micron dimensions with unique SERS properties could be achieved if the microdomains' alignments could be controlled. Graphoepitaxy is known to do this.<sup>123,125</sup> Thus, substrates were patterned with sets of 500 nm wide and 50 nm deep trenches before the BCP thin film was deposited and treated. Because the aligned PS-*b*-PMMA cylinder domains are confined to the trenches, the AuNR colloids were dropcast onto the substrates so the drying contact line would draw the NPs into the pre-defined trenches.<sup>107,110,112,114,141</sup> After the droplet has receded, a thin layer of solvent still covers each trench, since they are deeper than the AuNRs' diameters. This is similar to the situation depicted in the middle panel of Figure 3.3.3b, meaning that as the solvent evaporates, the previously described capillary forces and the BCP microdomains will direct the AuNR assembly. The Figure 3.2.2b AuNRs were found in the trenches with over 97% selectivity, with surface densities dictated by the number of depositions performed. For trenches with surface densities of 40 AuNRs/ $\mu\text{m}^2$  (Figure 3.3.5a) and 160 AuNRs/ $\mu\text{m}^2$  (Figure 3.3.5b), the AuNRs aligned along the straight BCP contours, while trenches with over 250 AuNRs/ $\mu\text{m}^2$  (Figure 3.3.5c) exhibited large, 3D clusters that lost the structure of the underlying film, similar to Figure 3.3.3c.

The nearly monolayer coverage of linearly aligned AuNRs in the trenches of Figure 3.3.5b

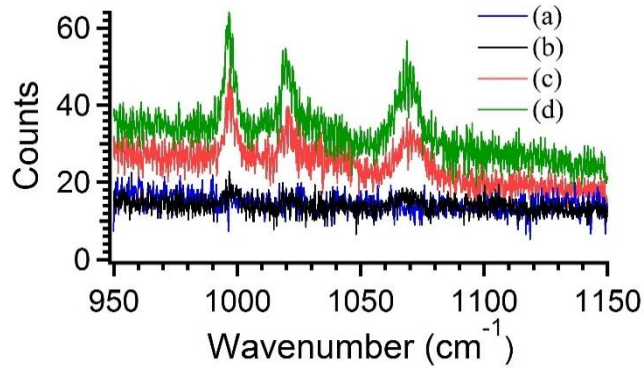


**Figure 3.3.4** Raman spectra of (a) BCP fingerprint substrate without AuNRs, (b) Figure 3.3.1a, 45 AuNRs/ $\mu\text{m}^2$  substrate, (c) Figure 3.3.1b, 160 AuNRs/ $\mu\text{m}^2$  substrate, (d) Figure 3.3.1c, >300 AuNRs/ $\mu\text{m}^2$  substrate. The peaks at 998, 1022, and 1072  $\text{cm}^{-1}$  are the characteristic BT peaks in this region.

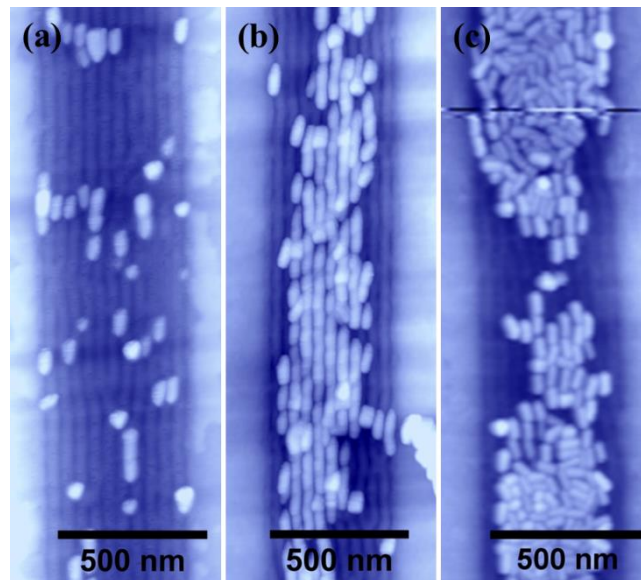


**Figure 3.3.5** AFM images of different Figure 3.2.22b AuNR colloid concentrations dropcast onto laterally ordered thin films of horizontal, cylinder forming PS-*b*-PMMA BCP made using graphoepitaxy. The AuNR densities are (a) 40 AuNRs/ $\mu\text{m}^2$ , (b) 160 AuNR/ $\mu\text{m}^2$ , and (c) >250 AuNRs/ $\mu\text{m}^2$ . The AuNRs are 20 nm by 61 nm, and the images are  $0.75 \mu\text{m} \times 1.5 \mu\text{m}$ .

present a combination of surface density and alignment that should have the most interesting and useful SERS properties. Explicitly, we wished to investigate how the AuNR localization affected the Raman signal across the substrate and whether the nanowire AuNR arrays exhibited polarization dependent SERS.<sup>142-144</sup> Because the graphoepitaxy trenches are optically identifiable, local regions on the substrates can be closely matched with corresponding AFM images (Figures 3.3.6, 3.3.7). Thus, samples were functionalized with a monolayer of BT,<sup>132</sup> mounted on a rotation stage, and the signal intensities of the characteristic BT peaks at 998, 1022, 1072, and 1572  $\text{cm}^{-1}$  were tracked by scanning the laser over specific trenches oriented parallel ( $0^\circ$ ) (Figures 3.3.6a, 3.3.7a) and perpendicular ( $90^\circ$ ) (Figure 3.3.6c, 3.3.7b) to the incident laser polarization in 200 nm steps. When the trenches were aligned parallel to the laser polarization (Figures 3.3.6a, 3.3.7a), the BT peak intensities modulated with the periodicity of the trenches, showing a 3.5x signal enhancement when the laser scanned inside, as opposed to outside, the trench (Figures 3.3.6b, 3.3.7a). For the Figures 3.3.6 and 3.3.7 sample, this corresponds to 1200 nm, since the trenches were 500 nm wide and were separated by 700 nm crests. This periodicity and signal localization are especially impressive since the theoretical minimum of the laser spot diameter was  $\sim 1064$  nm,  $\sim 50\%$  larger than the spacing between the trenches. When the trench was aligned perpendicular to the laser polarization (Figures 3.3.6c, 3.3.7b), the Raman signal intensities were severely reduced and showed no correlation with the substrate's surface (Figures 3.3.6d, 3.3.7b). The in-trench signal intensities of the parallel orientation exhibited a 24-fold enhancement over the same regions in the perpendicular orientation, demonstrating that these large, ordered, macroscopic arrays of anisotropic NPs maintain the polarization dependence of single structures (Figure 3.3.7). These SERS results show that macroscopic systems of closely spaced, colloiddally synthesized NPs will still have strong, directionally dependent electromagnetic enhancement properties when their

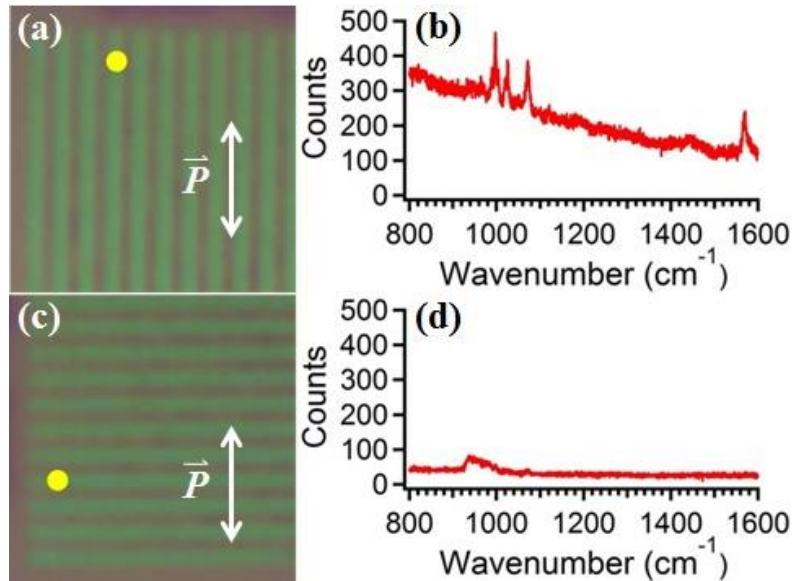


**Figure 3.3.6** (a, c) Optical images of graphoepitaxy trenches oriented parallel (a) and perpendicular (c) to the incident laser. The yellow dot indicates the region of the trench that was scanned over. (b, d) Raw Raman spectra recorded from the middle of each trench oriented parallel (b) and perpendicular (d) to the laser. The spectral features in (b) correspond to the characteristic BT peaks in this region, while the spectral feature at  $950\text{ cm}^{-1}$  in (d) corresponds to the silicon feature in this region. These spectra correspond to the respective 600 nm step positions in Figure 3.3.7a,b. The arrows and  $\vec{P}$  indicate the laser orientation relative to the substrate.

alignment is carefully controlled.

### 3.4 Conclusion

In summary, we investigated the alignment of gold nanorods on topographically enhanced, horizontal cylinder-forming PS-*b*-PMMA BCP templates, whose corrugation was much smaller than the widths of the gold nanorods. We demonstrated precise control over the ordering and orientation of gold nanorods of multiple aspect ratios for surface densities at and below 160

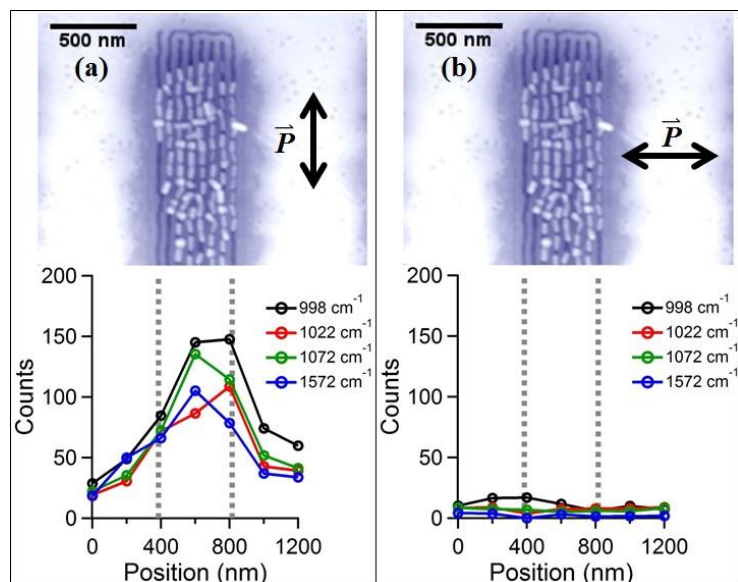


**Figure 3.3.7** (a) Results of the Raman spectral mapping over the graphoepitaxy trench aligned parallel to the laser (Figure 3.3.6a). Top: AFM image of the trench region. Bottom: Plot of the signal intensities of the four characteristic BT peaks, which are maximized within the trench and minimized in regions outside the trench. (b) Results of the Raman spectral mapping over the graphoepitaxy trench aligned perpendicular to the laser (Figure 3.3.6b). Top: AFM image of the trench region. Bottom: Plot of the signal intensities of the four characteristic BT peaks, which are severely reduced and featureless. The arrows and  $\vec{P}$  indicate the laser orientation relative to the substrate, and the gray lines indicate the width of the trench.

AuNR/ $\mu\text{m}^2$ , and presented a simple model that demonstrated that the topography of the substrate, while shallow, drives the gold nanorod alignment. Enhanced corrugation of the diblock template was achieved by chemical swelling prior to deposition of the metallic nanorods. Graphoepitaxy of the diblock copolymer in nanoconfining channels was employed to achieve essentially perfect long-range orientation of the templating substrate, while subsequent deposition of nanorods whose alignment maps onto that of the diblock template with high fidelity provides novel organic-

inorganic hybrid surfaces exhibiting highly-aligned arrays of nanorods. We characterized the SERS properties of these structures, and found that they exhibit extreme signal localization and polarization dependent spectra, with a maximum 24-fold signal enhancement. This effective, topography driven AuNR assembly and alignment that shows strong, directional electromagnetic enhancements offers great potential for the fabrication of reproducible, macroscopic, colloidal AuNR based plasmonic waveguides, optoelectronics and sensing chips.

### **3.5 Post-Publication Notes**

Before moving on, there are a couple of items worth mentioning about this project. First, we did initially attempt this work with AuBPs, but given how they lie on substrates,<sup>50</sup> it didn't work very well. The second point is that, after this paper was published, the AuNR syntheses were further refined. This is especially true for the high AR rods with LSP around 1064 nm (Figure 3.2.2e), which did not initially have very high yield. To make AuNRs with LSPs at ~800 nm with high yield, substitute 384  $\mu\text{L}$  of 10 mM  $\text{AgNO}_3$  for the amount listed in the methods section, and add 500  $\mu\text{L}$  of 1 M HCl. To make AuNRs with LSPs at ~1060 nm with high yield, substitute 192  $\mu\text{L}$  of 10 mM  $\text{AgNO}_3$  for the amount listed in the methods section, and add 500  $\mu\text{L}$  of 1 M HCl.

# **Chapter 4. Surface Morphology Development in Diblock Copolymer Thin Films through Sequential Solvent Exposure**

Collaborator: Alexander Filatov

Special thanks to: Nicole James, Prof. Heinrich Jaeger

This chapter presents my currently unpublished work on polystyrene-poly(2-vinylpyridine) (PS-P2VP) diblock copolymer thin films upon exposure to several P2VP selective solvents. Initially intended to expand upon the results of chapter 3, this project eventually took on a life of its own. Pre-treatment of a diblock copolymer thin film with a nearly neutral solvent dramatically improves the minority-block's swelling when the film is exposed to selective solvents. Oven annealed PS-P2VP thin films were exposed to P2VP selective solvents, with or without a tetrahydrofuran vapor treatment, and the resulting surface morphologies were characterized. Pre-treating the films not only increased the number of swelling events, but also induced the development of never previously reported, raised, horizontal P2VP cylinders. These cylinders are inverted from the standard post-swelling structures, and arise due to a complex set of interactions. By observing the selective deposition of small, negatively charged gold nanoparticles, we also show that P2VP never over-swells to cover film surfaces, instead remaining localized to its cylinder domains. Using shear-force, we macroscopically align the diblock copolymer, and use it as a template to control the assembly of gold nanoparticles onto films with polarization dependent optical properties.

## **4.1 Introduction**

As the field of nanoparticles (NPs) matures, the controlled self-assembly of these inorganic materials offers promising pathways for their application.<sup>100,145</sup> In particular, thin films of gold nanoparticles (AuNPs) have already demonstrated possible applications as sensors<sup>22,23,100,102</sup> and filters.<sup>146,147</sup> Interest in these particles is driven by their well-known electromagnetic field enhancements, with closely spaced particles creating the strongest ‘hot-spots.’<sup>100,122</sup>

Diblock copolymer thin films offer a unique template to control the self-assembly of NPs (and AuNPs in particular), by controlling the chemical nature<sup>106,111</sup> or topography<sup>22,111,129,131,148,149</sup> of their surfaces, in conjunction with their underlying alignment.<sup>22,150</sup> Several procedures exist to macroscopically align horizontal, cylinder forming diblock copolymer thin films<sup>151–156</sup> and modifications to their topography are usually achieved due to the selectivity of different solvents for each block.<sup>157</sup>

Before these films can be used, though, how and why topographies develop must be understood. Thus, this work presents the surface morphology changes in thin films of a commercially available, shear-force alignable,<sup>152</sup> cylinder forming PS-P2VP diblock copolymer. We discover that pre-treating the films with a slightly selective P2VP solvent not only increases the number of swelling events that occur, but also results in a never before seen surface topography that cannot be explained by traditional swelling descriptions.<sup>157,158</sup> We therefore investigate the diblock’s swelling behavior, ultimately elucidating the criteria that yield the different morphologies. Using small, negatively charged AuNPs, we probe the chemical nature of these films at the nanoscale, as well as demonstrating their utility as templates for NP alignment and growth. By aligning the underlying copolymer, we AuNP films with macroscopic structural and optical anisotropies.

## 4.2 Experimental Methods

**New Materials.** Cylinder forming polystyrene-poly(2-vinylpyridine) was purchased from Polymer Source Inc. and used without further purification. 1.1 mm ITO glass slides from NANOCS were cut to 1 cm x 1 cm, and cleaned with ethanol, acetone, chloroform, and toluene before use. Tetrahydrofuran (anhydrous, THF), ethanol (200 proof, EtOH), acetic acid (glacial, AA), chloroform, and acetone were purchased from Fisher and used without further purification. Formic acid ( $\geq 95\%$ , FA), propionic acid ( $\geq 99.5\%$ , PA), butyric acid ( $\geq 99\%$ , BA), L-ascorbic acid ( $\geq 99.0\%$ ), and toluene ( $\geq 99\%$ ) were obtained from Sigma Aldrich and used without further purification. Gold(III) chloride trihydrate ( $\geq 99.99\%$  metals basis,  $\text{HAuCl}_4$ ) was bought from Acros and used without further purification. Hexadecyltrimethylammonium bromide ( $\geq 98\%$ , CTAB) was purchased from TCI and used without further purification. Sylgard 184 polydimethoxysilane (PDMS) and curing agent were used as obtained from Electron Microscopy Sciences.

**New Instrumentation.** All atomic force microscopy (AFM) micrographs were recorded using a Bruker Multimode 8 operating in soft tapping mode, all SEM images were recorded using a Zeiss Merlin with an accelerating voltage of 10 keV, and all XPS data were recorded on a Kratos AXIS Nova at an operating voltage of 160 eV, performing 5 sweeps with dwell times of 0.1 s for survey spectra, and 0.6 s for scanning the Nitrogen 1S peak regime. All UV/Vis absorption and reflectance spectra were recorded using a Cary UV/Vis/NIR 5000. For the polarization dependent data, the orientation of the incoming beam was set as S, and the sample was rotated manually. For the reflectance measurements, the sample was angled at  $45^\circ$  to the incoming beam, with the detector located at  $90^\circ$ . All images were analyzed in Gwyddion, and all graphs were made in Igor.

**New Methods.** Monolayer thin films of PS-P2VP were made by spincoating 1% w/w PS-P2VP solutions in a 70/30 toluene/THF mixture onto the cleaned ITO glass substrate between 3000 and

5500 rpm for 60 s. The substrates were then thermally annealed in an oven in an inert atmosphere (nitrogen, N<sub>2</sub>) at 230 °C for 20 - 24 hours.

Substrates were shear aligned using a simple weight and pulley system, with 869.33 g normal mass and 290.23 g lateral mass, similar to what has previously been described (Figure 4.2.1a).<sup>151</sup> After baking, the substrate was placed on a hot plate, and a 0.5-1 mm thick PDMS pad trimmed to smaller than its dimensions (~ 0.8 cm x 0.8 cm) was carefully placed on top. The normal force was then applied, and the temperature increased to 150 °C. The lateral force was then introduced, and allowed to shear the substrates for 60 minutes. After 60 minutes, the heat was turned off, and the system was allowed to cool to room temperature with the shear force in place to freeze the alignment. PDMS pads were prepared in a glass petri dish by mixing the Sylgard 184 elastomer and curing agent in a 10:1 w/w ratio, degassing the mixture for one hour, then baking it for at least two hours at ~70 °C.

Substrates were exposed to THF vapors at room temperature for 15 minutes by filling the bottom of a 50 mL beaker with ~5mL of THF, then carefully placing a secondary container holding the substrate in the beaker, and then covering the beaker with parafilm (Figure 4.2.1b,c). All other solvent vapor exposures were performed the same way. Other substrates were soaked in ~5 mL of the solvents at room temperature for 15 minutes, then rinsed with nanopure water (NPH<sub>2</sub>O), and blown dry with N<sub>2</sub>. The 10% w/w HCl and 1% w/w HCl solutions were prepared by diluting 1 mL and 100 μL of 37% HCl in 3.24 mL and 4.320 mL of NPH<sub>2</sub>O, respectively. Substrates soaked in PA and BA this way lost their PS- P2VP films (Figure 4.2.2).

The small AuNPs used in this study are the AuBP seeds, synthesized as described in chapter 2. The substrates were soaked face up in 3 mL aliquots of these particles for 1 or 24 hours. The gold overgrowth solution is the AuBP growth solution described in chapter 2. Once the growth

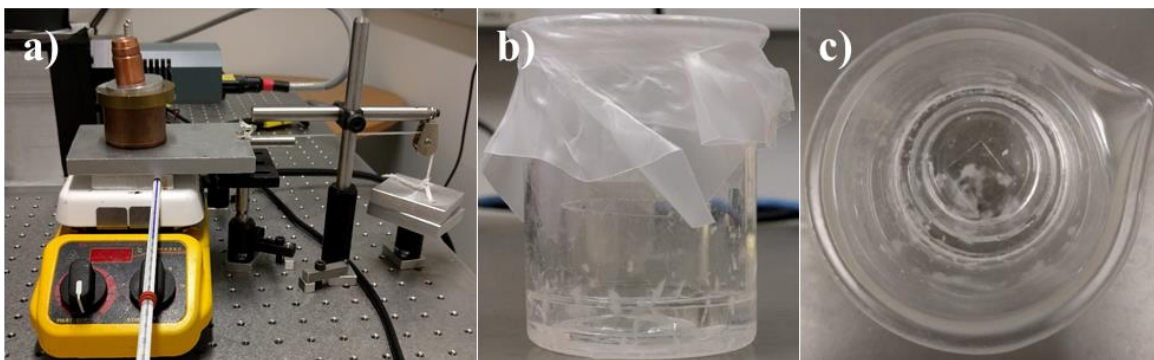


**Figure 4.2.1** a) Weight and pulley system used to align the PS-P2VP substrates. b) Side view and c) top view of solvent vapor annealing apparatus.

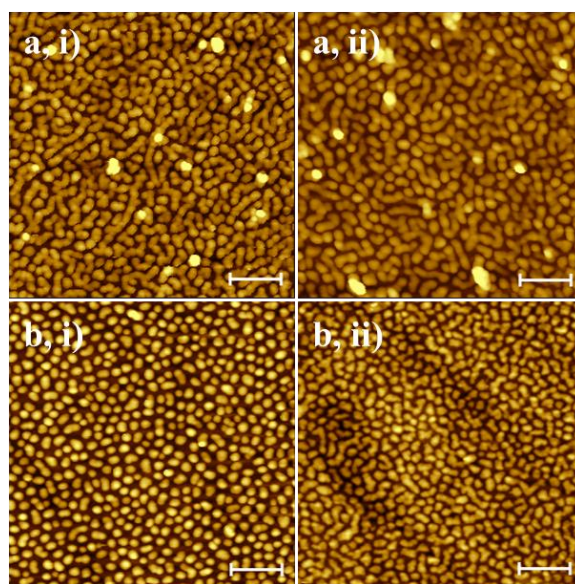


**Figure 4.2.2** AFM height micrograph of PS-P2VP diblock copolymer thin films after a) 20-24 hour, 230 °C oven anneal in N<sub>2</sub>, followed by i) 15 min soak in PA, ii) 15 min soak in BA, or b) 20-24 hour, 230 °C oven anneal in N<sub>2</sub>, 15 min THF vapor exposure, then i) 15 min soak in PA, ii) 15 min soak in BA. The scale bars are 200 nm.

solution had turned clear after the addition of the vit-C, the stirring was stopped. The substrates were then soaked, face up, in the reaction solution for 15 minutes. After this, they were removed,

rinsed thoroughly with  $\text{NH}_2\text{O}$ , and blown dry with  $\text{N}_2$ .

### 4.3 Results and Discussion

**Morphology Development.** Since PS-P2VP diblock copolymer thin films can be macroscopically aligned,<sup>152</sup> our initial investigations to make them useful for AuNP alignment focused on controlling the films' surface topographies. Building on the established literature,<sup>149,152,159</sup> several solvents expected to be P2VP selective were chosen to do this, with the results shown in Figure 4.3.1. Several morphologies developed, with the well-known mushroom caps the dominant.<sup>159</sup> These appeared in the films exposed to 10% HCl, 1% HCl, FA, BA, and EtOH (Figure 4.3.1b,c,d,g,h), with surface densities given in Table 4.3.1. The THF exposed film showed minimal enhancement of the encased P2VP cylinders, and it is difficult to precisely determine the AA and PA exposed film's surface morphologies. (Figures 4.3.1a,e,f, 4.3.2).

Given our previous work,<sup>22</sup> THF's uniform P2VP swelling (Table 4.3.1) seemed to offer a promising route to make the substrates we desired. However, THF had not brought the P2VP to the film's surface, as demonstrated by a comparison of the AFM phase images, XPS spectra, and water contact angles of an annealed and a THF exposed substrate (Figure 4.3.3). The film's surface remained coated in PS, which would be problematic for aqueous NP deposition.<sup>146,147</sup> Increasing the THF vapor exposure time could not change this (Figure 4.3.4).

Upon revisiting the results of Figure 4.3.1, it became clear that, while the other solvents did not exhibit the same swelling uniformity as THF, several seemed to swell P2VP better. Thus, we decided to try to enhance the corrugation of THF treated films by then exposing them to the other solvents. The differences are striking (Figure 4.3.5). While the majority of the topographies (Figure 4.3.5a,b,c,g) are still mushroom caps, they now appear with vastly higher surface densities

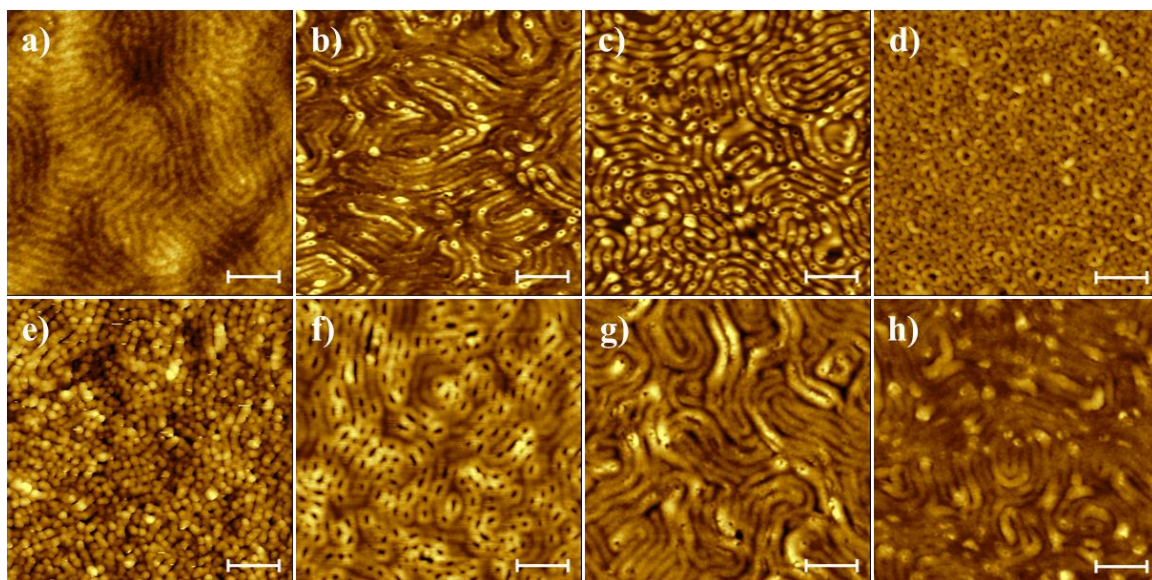


**Figure 4.3.1** AFM height micrographs of PS-P2VP diblock copolymer thin films after a) exposure to THF vapors, soaking in b) 10% HCl, c) 1% HCl, d) FA, e) AA, exposure to vapors of f) PA, g) BA, or soaking in g) EtOH for 15 minutes. All scale bars are 200 nm.

**Table 4.3.1** Analysis of Figure 4.3.1 Film Topographies

Solvent	THF	10% HCl	1% HCl	FA	AA	PA	BA	EtOH
Structure	Cylinder	Mushroom	Mushroom	Mushroom	---	---	Mushroom	Mushroom
Density/ Period, Corrugation	43.3 +/- 4.8 nm, 0.68 +/- 0.18 nm	99 structures per $\mu\text{m}^2$	252 structures per $\mu\text{m}^2$	447 structures per $\mu\text{m}^2$	---	---	33 structures per $\mu\text{m}^2$	11 structures per $\mu\text{m}^2$

(Table 4.3.2). This is especially true in the case of the EtOH, which had a 49x increase in mushroom caps/ $\mu\text{m}^2$ . As can be qualitatively observed by eye, and quantitatively determined by comparing the center-to-center widths of the caps (Table 4.3.2) with the cylinder spacing obtained from the THF exposed films (Table 4.3.1), the mushrooms are confined to the fingerprint pattern of the P2VP cylinders. While they occur with some regularity within the P2VP domains, this does not represent the development of Rayleigh instabilities, since the minimum period of the

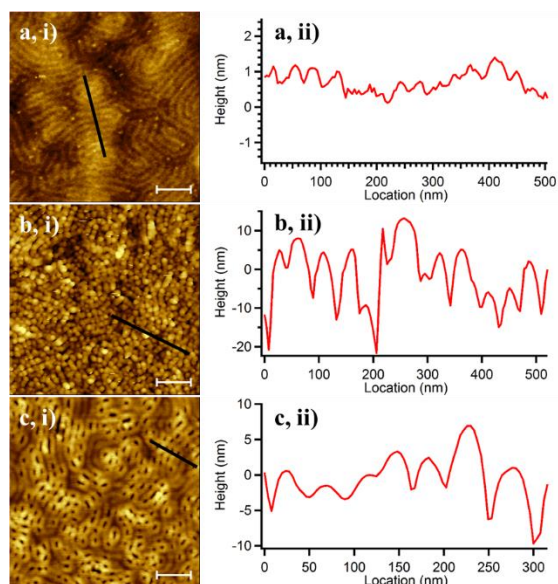


**Figure 4.3.2** AFM height micrographs (i) and height profiles (ii) along the black lines in (i) of substrates exposed to a) THF vapors, b) soaked in AA, and c) PA vapors for 15 minutes. The scale bars are all 200 nm.

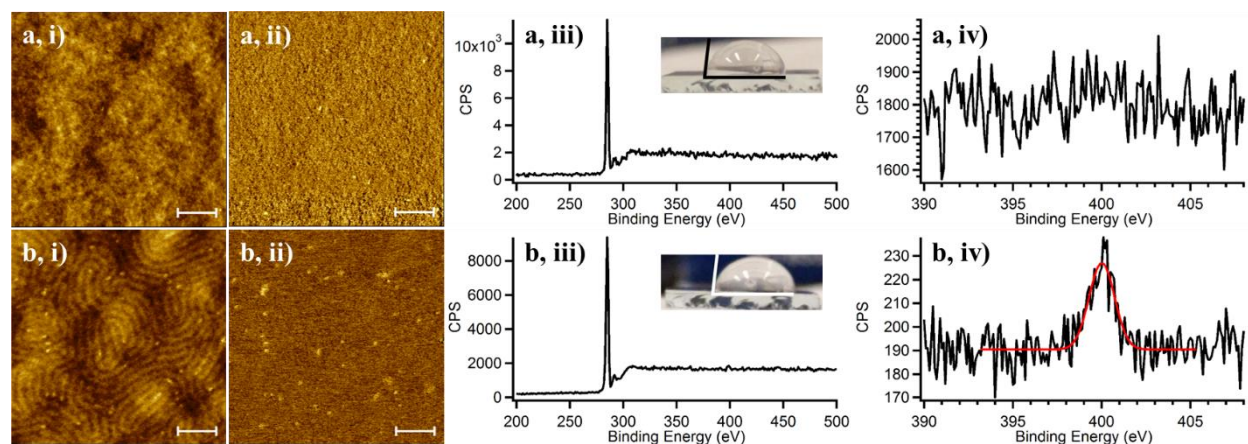


**Figure 4.3.3** i) AFM height micrograph, ii) AFM phase micrograph, iii) XPS survey, with water contact angle inset, and iv) XPS scan of the Nitrogen 1S peak around 400 eV of PS-P2VP diblock copolymer thin films after a) 230 °C 20 - 24 hour inert atmosphere bake, and b) after exposure to THF vapors for 15 minutes. The contact angles for both substrates are 85°, and the area of the Gaussian fit in b,iv) is 66.5 counts. The scale bars are all 200 nm.

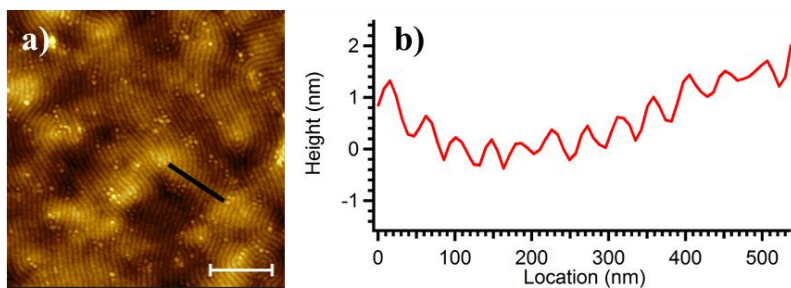


**Figure 4.3.4** PS-P2VP diblock copolymer thin film a) AFM height micrograph and b) height profile over the black line in a) after 12 hour exposure to THF vapors. Scale bar in a) is 500 nm.

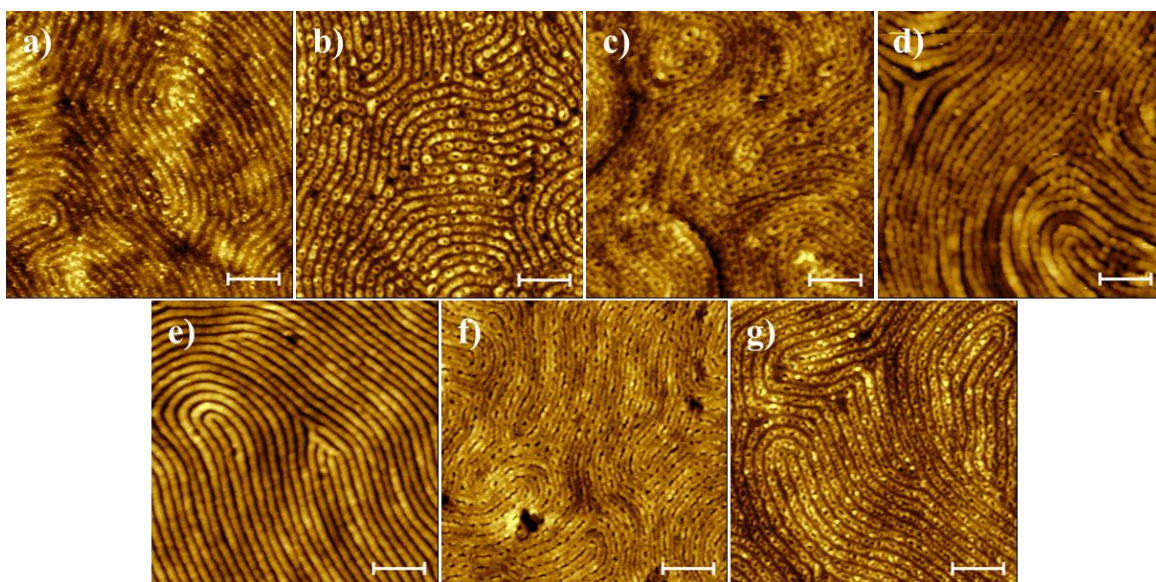


**Figure 4.3.5** AFM height micrographs of PS-P2VP diblock copolymer thin films after being exposed to THF vapors, then soaked in a) 10% HCl, b) 1% HCl, c) FA, d) AA, exposed to vapors of e) PA, f) BA, and soaked in g) EtOH for 15 minutes. All scale bars are 200 nm.

**Table 4.3.2** Analysis of Figure 4.3.5 Mushroom Topographies

Solvent	10% HCl	1% HCl	FA	EtOH
Density	301 structures per $\mu\text{m}^2$	500 structures per $\mu\text{m}^2$	457 structures per $\mu\text{m}^2$	535 structures per $\mu\text{m}^2$
Center to Center Width	42.1 +/- 5.4 nm	44.1 +/- 4.8 nm	46.6 +/- 4.7 nm	44.8 +/- 4.6 nm
Center to Center Length	42.1 +/- 11.9 nm	42.0 +/- 11.7 nm	45.1 +/- 11.9 nm	34.3 +/- 8.7 nm

mushrooms would have to be larger than the circumference of the cylinders.<sup>160</sup> This would correspond to a distance of almost 70 nm for this system, which is not observed (Table 4.3.2). Thus, the mushrooms structures are the result of separate, localized swelling events within the P2VP cylinder as they seek to release strain, and not due to the liquefaction of the entire domain.

The rod-like structures obtained after soaking in AA (Figure 4.3.5d) and upon exposure to PA or BA vapors (Figure 4.3.5e,f) are considerably more interesting. These also correspond to the P2VP domains (Table 4.3.3), with the PA exposed film appearing similar to morphologies reported to successfully deposit and align AuNPs.<sup>22,149</sup> However, the height profiles of these films show that the topography is inverted from the norm (Figure 4.3.6).<sup>22,148,149,158</sup> This was surprising, since such a structure has not been observed in PS-P2VP thin films before, and doesn't fit the standard description of diblock copolymer thin film swelling.<sup>22,148,149,158,159,161</sup> Over-swollen domains that collapse can only create negative spaces, like the mushroom caps, not raised, positive spaces, like these cylinders. The hydrophilic nature and improved Nitrogen 1S signal of the substrates confirm that the raised rods are composed of P2VP (Figure 4.3.7a). However, when compared with the same data for a mushroom forming film, the cylinder substrate is less hydrophilic and has a smaller Nitrogen signal (Figure 4.3.7b). These ridges, then, do not present as much P2VP at a film's surface as the mushrooms. Combined with their localization, this raises interesting questions about the material that exists between them.

To elucidate the chemical nature of the Figure 4.3.5 film surfaces, selected substrates of each morphology (1% HCl and FA for mushroom caps, and PA for raised cylinders) were soaked in solutions of small, negatively charged AuNPs for 73 minutes. As seen in Figure 4.3.8, the AuNPs only deposit where P2VP is exposed, following the fingerprint patterns across the films' surface, and even preferentially aggregate around the edges of the exposed mushrooms (Figure

**Table 4.3.3** Analysis of Figure 4.3.5 Cylinder Topographies

Solvent	AA	PA	BA
Center-Center Width, Corrugation	38.5 +/- 7.7 nm, 9.1 +/- 5.3 nm	42.0 +/- 6.8 nm, 9.5 +/- 1.8 nm	40.4 +/- 3.9 nm, 2.9 +/- 2.1 nm

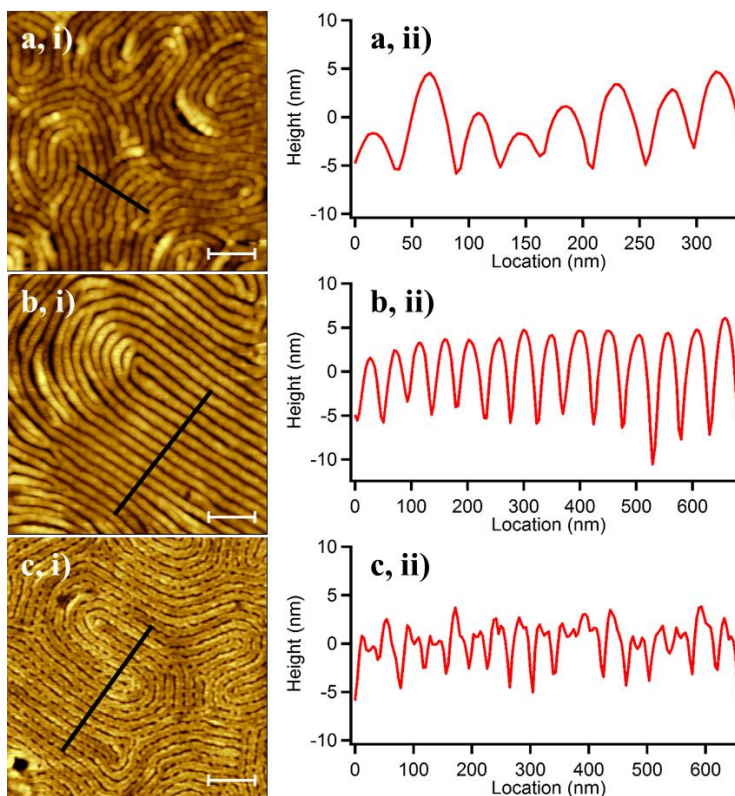


**Figure 4.3.6** AFM height micrographs (i) and corresponding height profiles across the black lines (ii) of PS-P2VP diblock copolymer thin films after being exposed to THF vapors, then a) soaked in AA, or exposed to vapors of b) PA or c) BA for 15 minutes. All scale bars are 200 nm.

4.3.8a,b). Substrates soaked in AuNPs for 24 hours show the same selectivity (Figure 4.3.9), even when the P2VP selective solvent is EtOH (Figure 4.3.9c). These results confirm P2VP's confined swollen morphologies, which is unlike most other diblock copolymer systems.<sup>22,149,158,161</sup> Since P2VP does not over-swell and cover the film surfaces, PS still coats the interstitial regions (Figure 4.3.10). This makes the nanoscale nature of these substrates complex, and has important

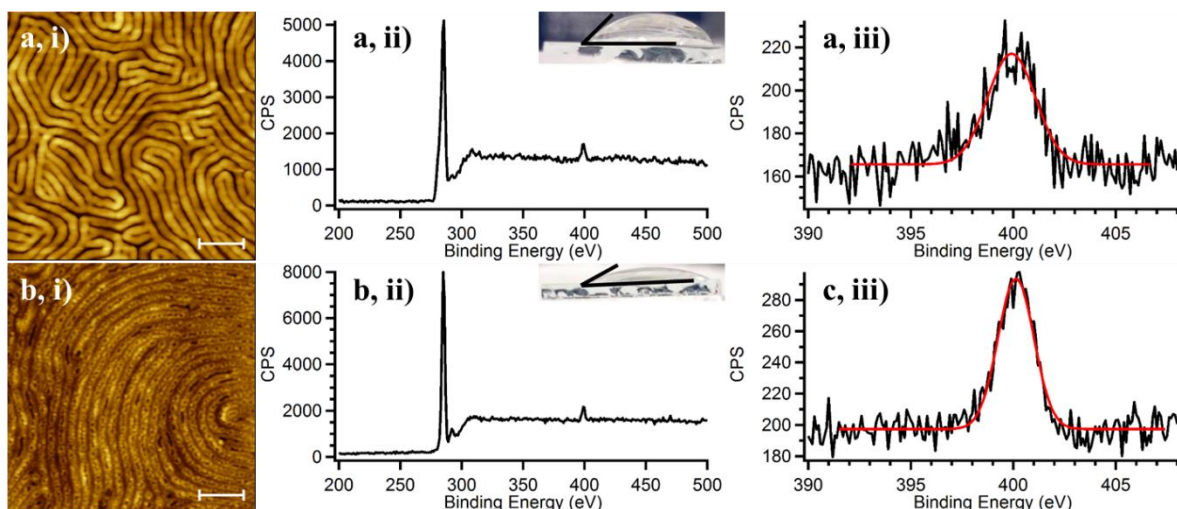


**Figure 4.3.7** i) AFM height micrograph, ii) XPS survey, with inset water contact angle, and iii) XPS scan of the Nitrogen 1S peak region of substrates pre-treated with THF vapors, then a) exposed to PA vapors, and b) soaked in EtOH for 15 minutes. The scale bars in i) are 200 nm, the water contact angle of a,ii) is  $51.6^\circ$ , and of b,ii) is  $23.1^\circ$ , and the area of the Gaussian fit in a,iii) is 156.5 counts, and in b,iii) is 211.5 counts.

implications for this copolymer's use to assemble NPs.

**THF Effect.** The swelling morphologies of Figure 4.3.5 arise through a combination of the THF pre-treatment and the P2VP selective solvent effects. In an effort to de-convolute their contributions, and try to understand our system, the films of Figures 4.3.1 and 4.3.5 were re-exposed to THF vapors (Figures 4.3.11 and 4.3.12, i) panels). Surprisingly, the substrates all lost their topographies, appearing as if they had only been exposed to THF. As is confirmed by the featureless AFM phase image, similar height profile, water contact angle, and XPS analysis of the N1S region (Figure 4.3.13) to the THF only exposed substrates (Figures 4.3.1a, 4.3.2a, 4.3.3b), the P2VP cylinders are again encased in PS. Upon exposure to their respective P2VP selective

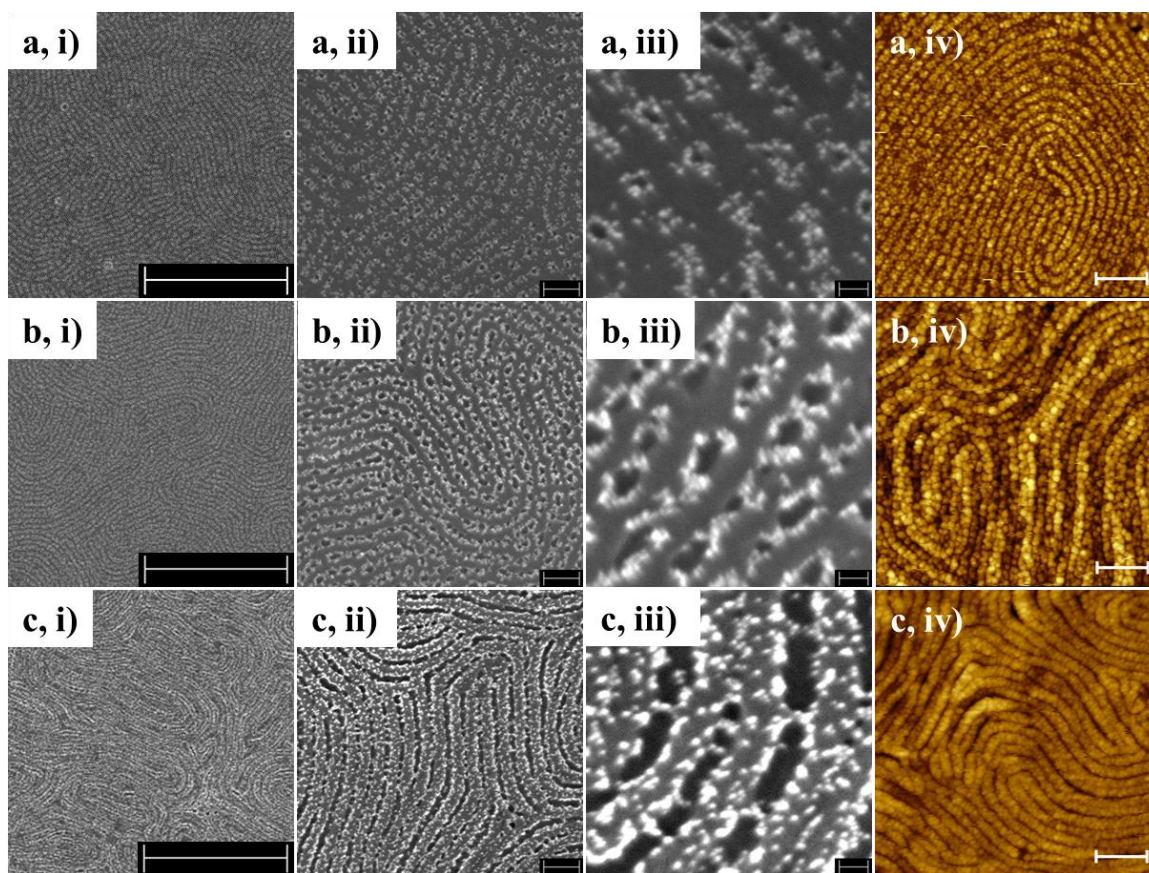


**Figure 4.3.8** i) – iii) SEM and iv) AFM height images of substrates pre-treated with THF vapor, then soaked in a) 1% HCl, b) FA, or exposed to vapors of c) PA for 15 minutes, then soaked in negatively charged AuNPs for 73 minutes. The scale bars are i) 1  $\mu\text{m}$ , ii) 100 nm, and iii) 20 nm, and iv) 200 nm.

solvents, all the films developed morphologies similar to those in Figure 4.3.5 (Figures 4.3.11 and 4.3.12, ii) panels). P2VP's presence on the surface of the substrates was confirmed with a similar set of analyses (Figure 4.3.14).

Similar PS-P2VP surface reversibility has only been reported with solvents that are distinctly preferential for one polymer block or the other,<sup>162</sup> not the same one. Since THF's sudden lack of P2VP selectivity seems to contradict our previous results, multiple rounds of solvent

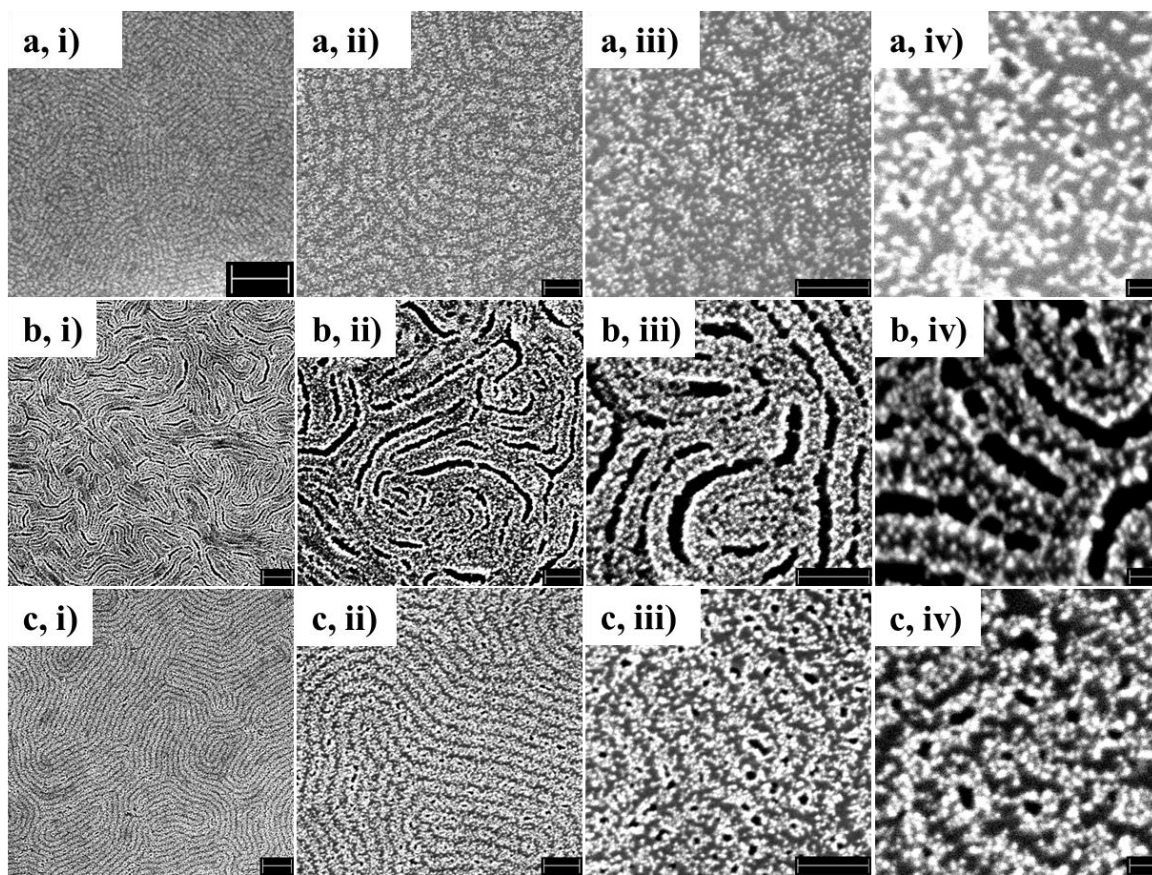


**Figure 4.3.9** SEM images of THF pre-treated PS-P2VP substrates, then a) soaked in 1% HCl, b) exposed to vapors of PA, or c) soaked in EtOH for 15 minutes, then soaked in citrate capped AuNPs for 24 hours. The scale bars are i) 200 nm, ii) and iii) 100 nm, and iv) 20 nm.

exposures were performed to study this phenomenon further (Figures 4.3.15 – 4.3.21). In every instance, the films lost their corrugation after a THF treatment, and with the exception of the EtOH soaked substrate (Figure 4.3.21), all their phase micrographs were featureless as well. The 10% HCl, FA, AA, and BA exposed films consistently developed the same morphologies as observed in Figure 4.3.5 after exposure to their P2VP selective solvent (Figures 4.3.15, 4.3.17, 4.3.18, 4.3.20). The films exposed to 1% HCl, PA, and EtOH (Figures 4.3.16, 4.3.19, 4.3.21), on the other hand, began to exhibit vertical pore<sup>149</sup> or spherical micelle-like<sup>162</sup> morphologies after multiple

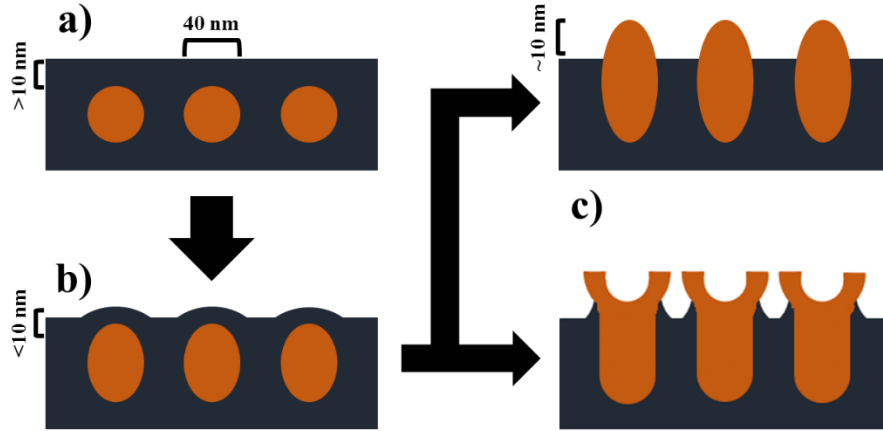


**Figure 4.3.10** Schematic depicting the PS-P2VP diblock copolymer thin film's evolution with solvent treatments. The PS matrix is black, and the P2VP domains are orange. a) Film morphology after oven annealing. The film thickness is about 70 nm, and the P2VP cylinders are about 40 nm wide, and buried in the PS matrix at a depth greater than 10 nm. b) Film morphology after THF vapor treatment. The surface swelling is as described in Figures 4.3.1, 4.3.3, and 4.3.4, and the P2VP cylinders are now within about 10 nm of the film surface. c) Swollen P2VP raised cylinder or mushroom morphologies after selective solvent treatment.

rounds of THF and P2VP selective solvent treatments. The new morphologies initially followed the P2VP fingerprint pattern, but eventually began to exhibit hexagonal packing (Figures 4.3.16, 4.3.19, and 4.3.21), indicating that the original P2VP cylinder domains are breaking-up due to the repeated exposures.

These results help elucidate THF's unique effect on our diblock copolymer films. The Flory-Huggins Interaction Parameters<sup>157</sup> is often used to describe how well a solvent and a polymer will interact,

$$\chi_{\text{solvent-polymer}} = \frac{V_s}{RT} (\delta_s - \delta_p)^2 + 0.34 \quad (1)$$

where  $V_s$  is the molar volume of the solvent, in  $m^3/L$ ,  $R$  is the gas constant,  $T$  is the temperature,

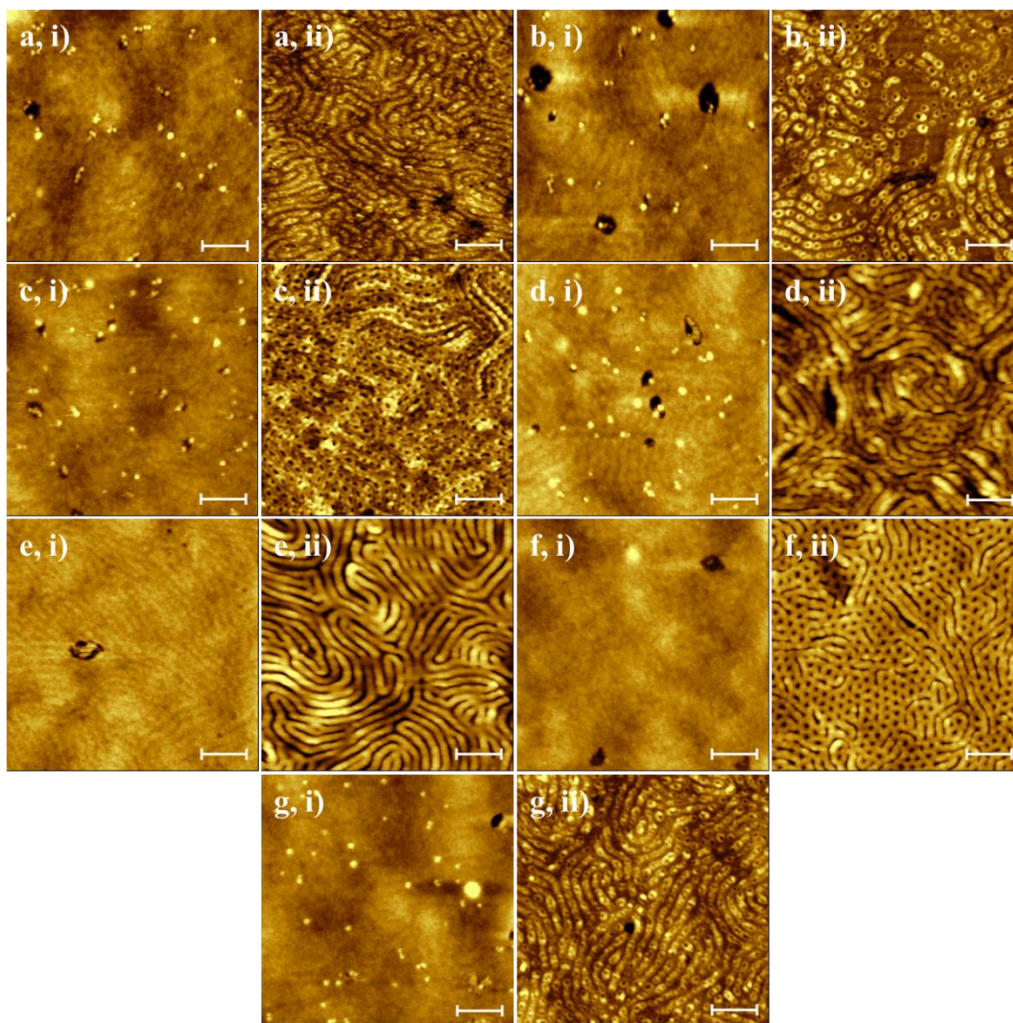


**Figure 4.3.11** AFM height micrographs of the substrates in Figure 4.3.1 (no THF pre-treatment) after i) being exposed to THF vapors for 15 minutes, then soaked in a,ii) 10% HCl, b,ii) 1% HCl, c,ii) FA, d,ii) AA, exposed to vapors of e,ii) PA, f,ii) BA, or soaked in g,ii) EtOH again for 15 minutes. All scale bars are 200 nm.

and  $\delta_s$  and  $\delta_p$  are the Hildebrand parameters of the solvent and polymer, respectively.<sup>157</sup> A comparison of  $\chi_{THF-PS,P2VP}$  (Table 4.3.4) indicate that THF should be more preferential for PS. However, THF's polar nature and well known hydrogen bonding capabilities<sup>163</sup> could lead to errors when calculating  $\chi$  from its Hildebrand parameter, which assumes nonpolar conditions and

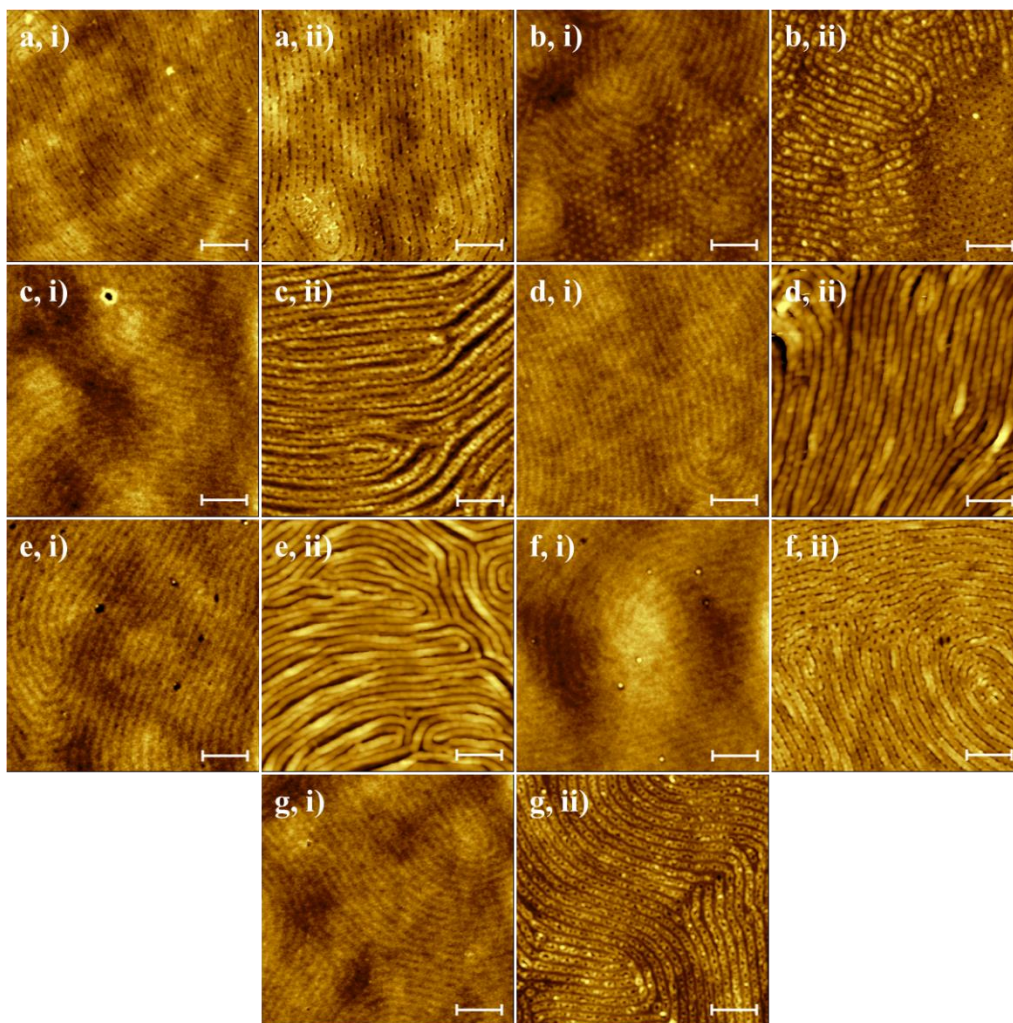


**Figure 4.3.12** AFM height micrographs of the substrates in Figure 4.3.5 (THF pre-treated) after i) being exposed to THF vapors for 15 minutes, then soaked in a,ii) 10% HCl, b,ii) 1% HCl, c,ii) FA, d,ii) AA, exposed to vapors of e,ii) PA, f,ii) BA, or soaked in g,ii) EtOH again for 15 minutes. All scale bars are 200 nm.

interactions.<sup>157</sup> This would explain why our observed swelling results (Figures 4.3.1a, 4.3.2a, 4.3.3b) seem to contradict the  $\chi$  values, and fits the expectation that the slightly polar and hydrogen bonding THF would preferentially interact with the slightly polar and hydrogen bonding P2VP block of the copolymer.  $\chi_{THF-PS}$  being less than 0.5, though, indicates that THF will still interact

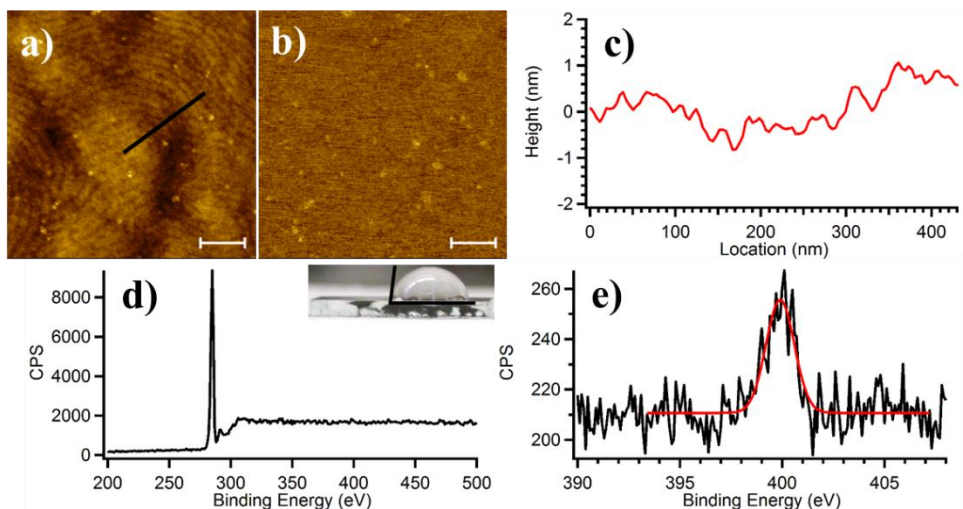


**Figure 4.3.13** a) AFM height and b) phase micrographs, c) height profile along the black line in a), d) XPS survey, with water contact angle inset, and e) XPS scan of the Nitrogen 1S peak of a substrate exposed to THF, PA, and then THF. The scale bars in a) and b) are 200 nm, the water contact angle in d) is  $81.6^\circ$ , and the area of the Gaussian fit in e) is 78.0 counts.

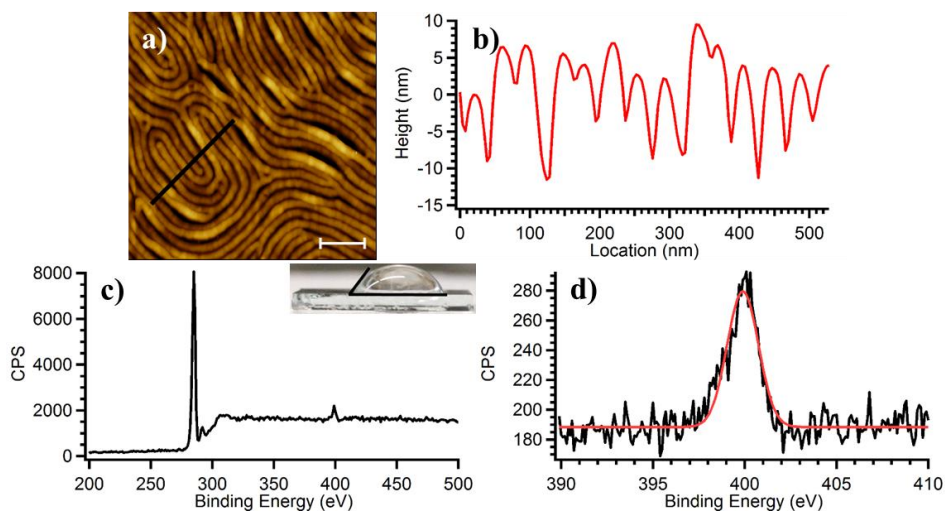


**Figure 4.3.14** a) AFM height micrograph, b) height profile along the black line in a), c) XPS survey, with water contact angle inset, and d) XPS scan of the Nitrogen 1S peak of a substrate exposed to THF, PA, THF, then PA. The scale bar in a) is 200 nm, the water contact angle in c) is  $66.1^\circ$ , and the area of the Gaussian fit in d) is 195.3 counts.

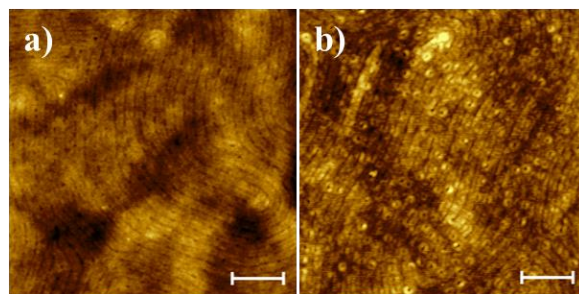


**Figure 4.3.15** AFM height micrographs of Figure 4.3.5a substrate after a) its fifth (THF vapor) and b) sixth solvent exposures (10% HCl soak). The scale bars are 200 nm.

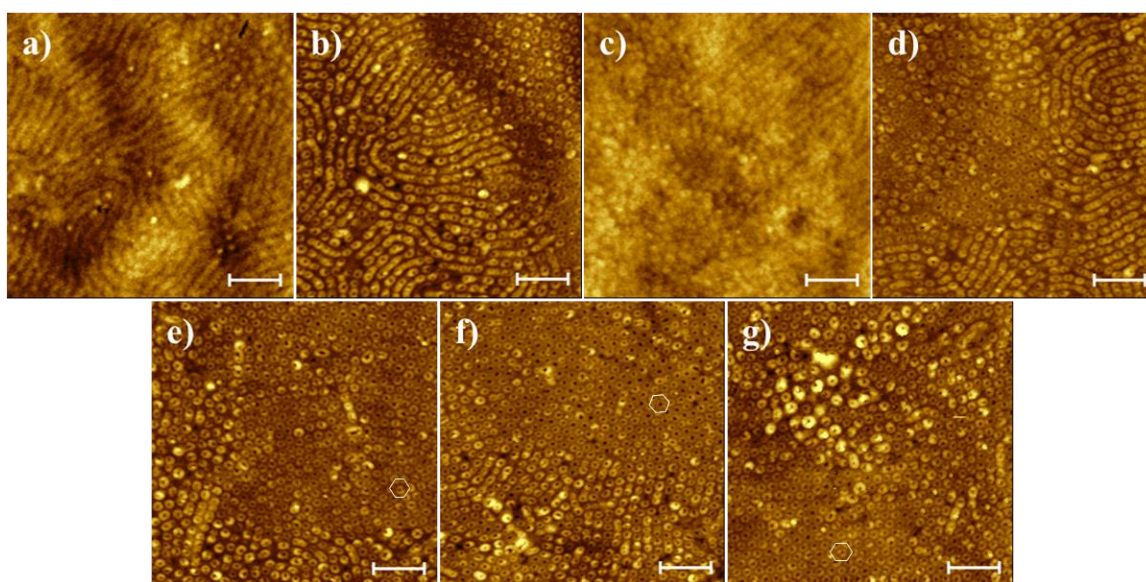


**Figure 4.3.16** AFM height micrographs of Figure 4.3.5b substrate after a) its fifth (THF vapor), b) its sixth (1% HCl soak), c) seventh (THF vapor), d) eighth (1% HCl soak), e) twelfth (THF, 1% HCl, THF, 1% HCl), f) sixteenth (THF, 1% HCl, THF, 1% HCl) and g) twentieth (THF, 1% HCl, THF, 1% HCl) solvent exposures. The scale bars are 200 nm, and the hexagons mark examples of hexagonal packing that develop.

well with PS. Thus, we propose that, while THF exhibits a slight preference for P2VP, it is a nearly-neutral solvent for this diblock copolymer, meaning exposure to its vapor plasticizes both

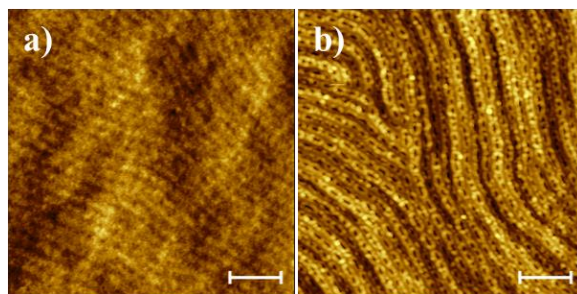


**Figure 4.3.17** AFM height micrographs of Figure 4.3.5c substrate after a) its fifth (THF vapor) and b) sixth solvent exposures (FA soak). The scale bars are 200 nm.

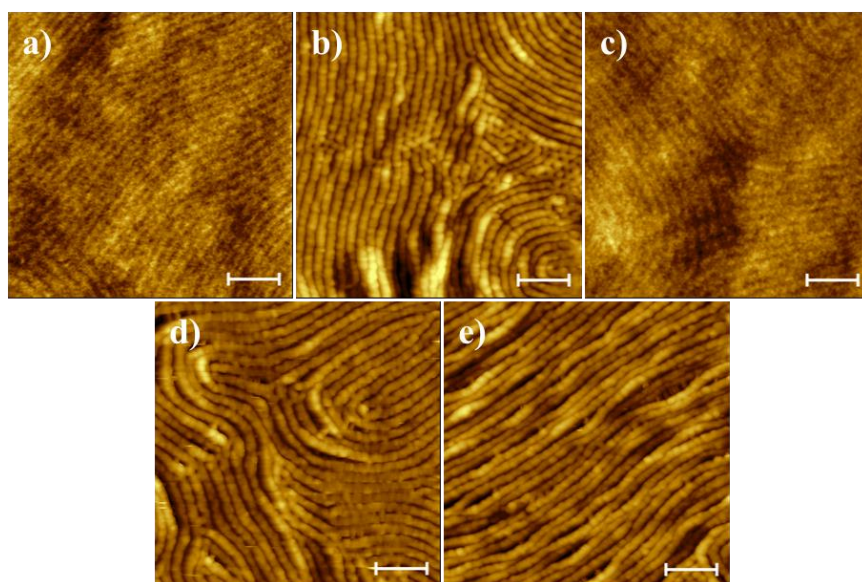


**Figure 4.3.18** AFM height micrographs of Figure 4.3.5d substrate after a) its fifth (THF vapor), b) sixth (AA soak), c) seventh (THF vapor), d) eighth (AA soak), and e) twelfth (THF, AA, THF, AA) solvent exposures. The scale bars are 200 nm.

blocks of our copolymer film, quite possibly through the incorporation of residual THF molecules into both domains. To directly test this, a film was thermally annealed, exposed to THF, and then baked at 80 °C for 72 hours under N<sub>2</sub> (Figure 4.3.22). The corrugation of the film was reduced, even though it was baked well below the glass transition temperature ( $T_g$ ) of both PS and P2VP.<sup>152</sup>

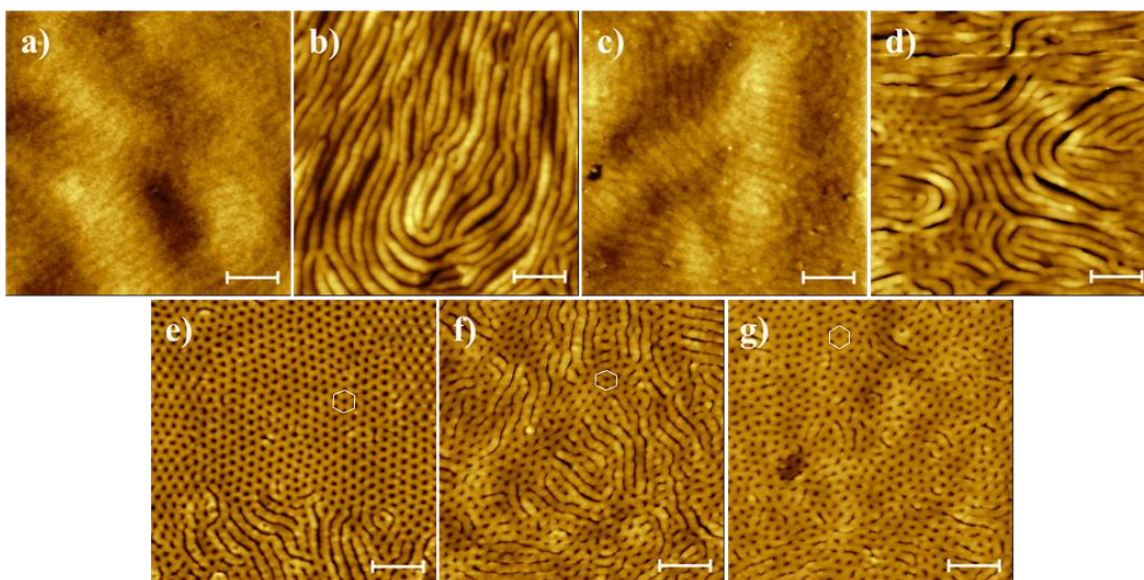


**Figure 4.3.19** AFM height micrographs of Figure 4.3.5e substrate after a) its fifth (THF vapor), b) sixth (PA vapor), c) seventh (THF vapor), d) eighth (PA vapor), e) twelfth (THF, PA, THF, PA), f) sixteenth (THF, PA, THF, PA), and g) twentieth (THF, PA, THF, PA) solvent exposures. The scale bars are 200 nm, and the hexagons mark examples of hexagonal packing.

This effect was even more pronounced on films exposed to THF and a P2VP selective solvent, when a completely featureless surface is achieved after baking at only 60 °C for 24 hours (Figure 4.3.23).

These results draw a close comparison to the diblock copolymer solvent vapor annealing technique, where the incorporation of the solvent into the thin film not only increases polymer chain mobility, but also affects how the blocks interact.<sup>164</sup> A key aspect of copolymer film swelling is how well the selective solvent can access its preferential block;<sup>158,162</sup> in this case, how well the P2VP selective solvents can permeate the PS matrix that encases the P2VP cylinder domains. As demonstrated by Tables 4.3.1 – 4.3.3, the substrates ‘pre-treated’ with THF have a higher surface density, in the case of the mushroom caps, or a more regular, better defined, and more steeply

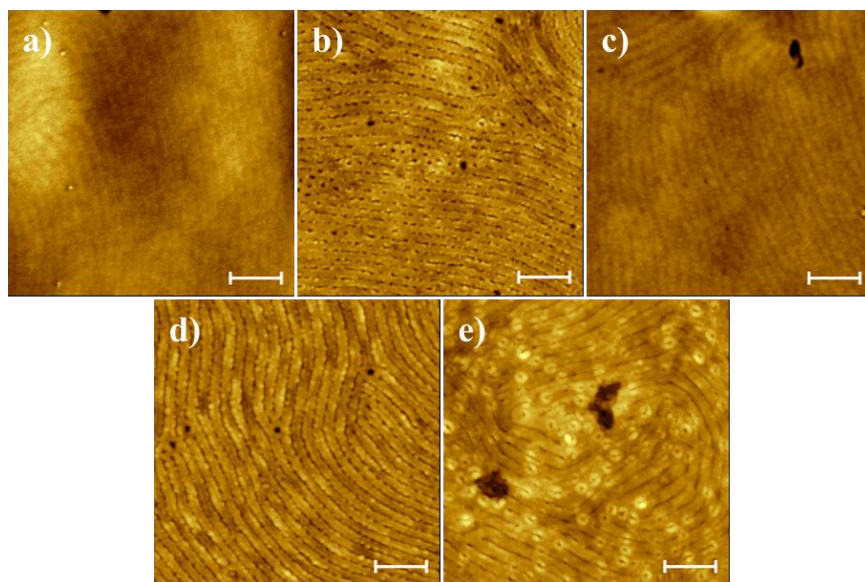


**Figure 4.3.20** AFM height micrographs of Figure 4.3.5f substrate after a) its fifth (THF vapor), b) sixth (BA vapor), c) seventh (THF vapor), d) eighth (BA vapor), and e) twelfth (THF, BA, THF, BA) solvent exposures. The scale bars are 200 nm.

corrugated, in the case of the cylinders, surface morphology upon selective solvent exposure (Figure 4.3.5, Tables 4.3.2 and 4.3.3) than their oven annealed only counterparts (Figure 4.3.1, Table 4.3.1). Easier penetration by the P2VP solvents of a PS block rendered slightly polar by residual THF molecules is the simplest explanation for this improvement.

Finally, THF's ability to favorably interact with the PS matrix explains the surface reversibility of the films in Figures 4.3.11, 4.3.12, and 4.3.15 – 4.3.21. Given the pHs, pKas (Table 4.3.5), and general polarity of the selective solvents used in this study, we propose that these solvents make the P2VP domains too polar to be swollen by THF anymore. Thus, further THF exposures would only result in the PS domains swelling. Since diblock copolymer domains are chemically bound to one another,<sup>22</sup> the PS swelling would force the P2VP domains to reorient by folding in on themselves, and ultimately being covered by PS (Figure 4.3.24). The

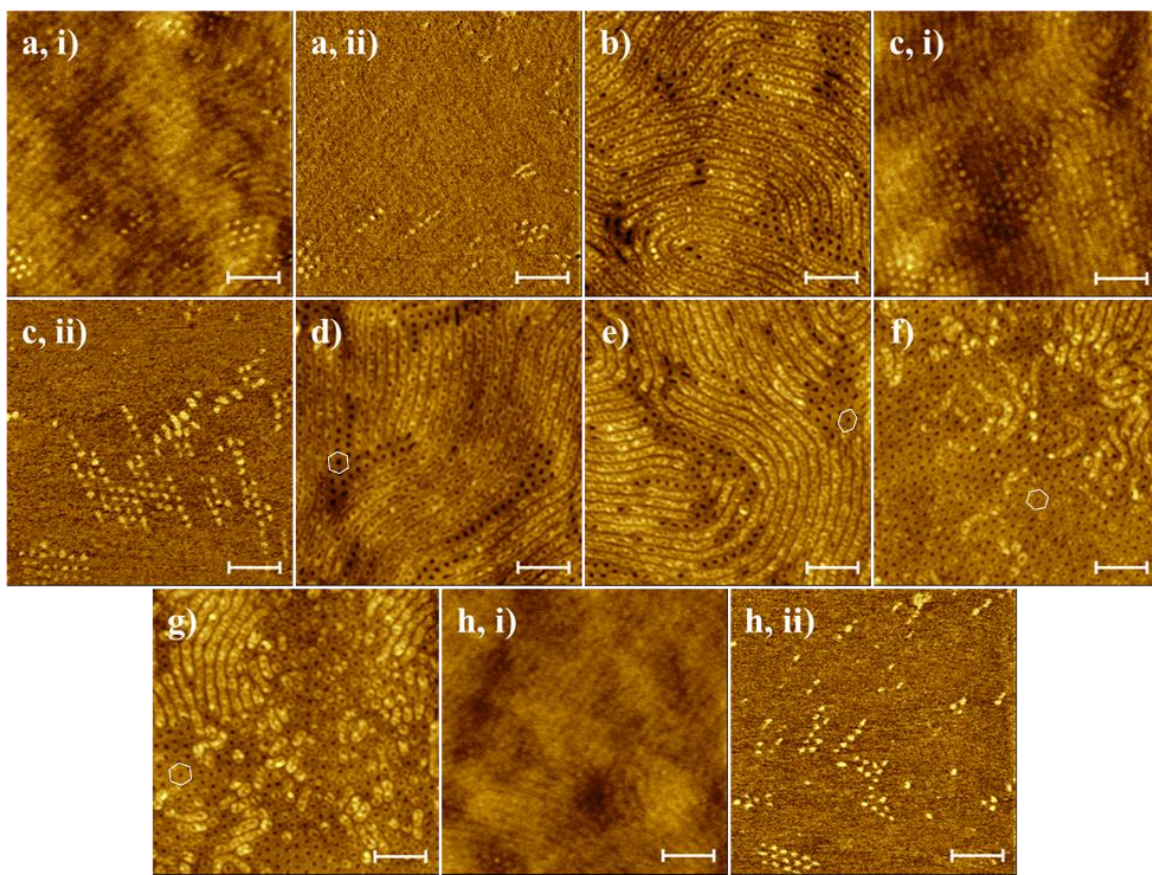


**Figure 4.3.21** AFM micrographs of Figure 4.3.5g substrate after a) its fifth (THF vapor), b) sixth (EtOH soak), c) seventh (THF vapor), d) eighth (EtOH soak), e) twelfth (THF, EtOH, THF, EtOH), f) sixteenth (THF, EtOH, THF, EtOH), g) twentieth (THF, EtOH, THF, EtOH), and h) twenty-first solvent (THF) exposures. In a), c), and h), image i) is the height profile, and ii) is the corresponding phase profile of i). The scale bars are 200 nm, and the hexagons mark examples of hexagonal packing.

**Table 4.3.4**

Flory-Huggins Interaction Parameters of PS and P2VP with the Solvents Used in this Study

Parameter	THF	FA	AA	PA	BA	EtOH	PS	P2VP
$\delta$ (MPa) <sup>1/2</sup>	18.61	24.81	20.7	20.3	21.1	26	18.67	21.27 <sup>165</sup>
$\chi_{solvent-PS}$	0.34	0.91	0.44	0.42	0.56	1.61	----	----
$\chi_{solvent-P2VP}$	0.57	0.53	0.35	0.37	0.34	0.87	----	----

\*All Hildebrand parameters come from ref. 157 unless otherwise specified.

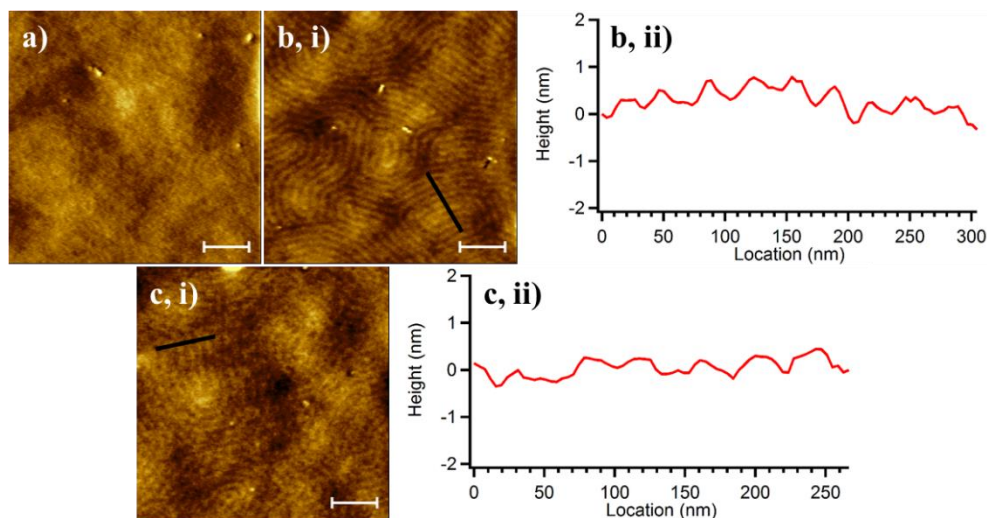


**Figure 4.3.22** AFM height micrographs of a substrate a) annealed at 230 °C for 20 – 24 hours, b, i) then exposed to THF vapors for 15 minutes, then c, i) baked at 80 °C for 72 hours. ii) are the height profiles across the black lines in their respective i). All scale bars are 200 nm.

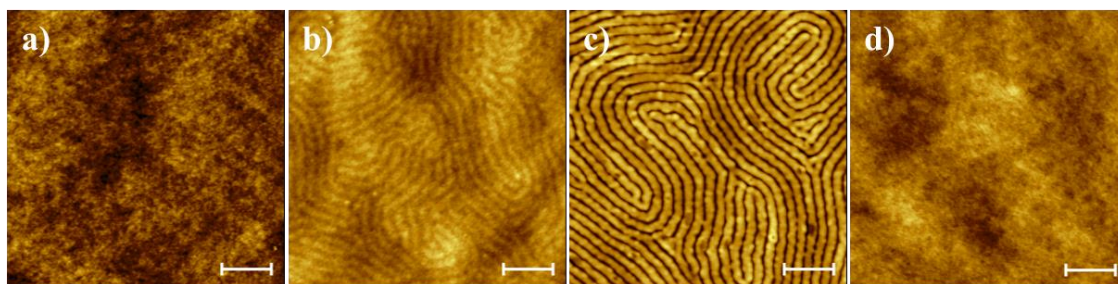


**Figure 4.3.23** AFM height micrographs of a PS-P2VP diblock film demonstrating its structural morphology changes after a) the 20- 24 hour 230 °C oven anneal, then b) a 15 min THF vapor exposure, then c) a 15 min PA vapor exposure, and finally a d) 24 hour, 60 °C bake. All scale bars are 200 nm.

**Table 4.3.5** pH and pKa Values of Materials Used in this Study

	10% HCl	1% HCl	FA	AA	PA	BA	EtOH	P2VP	PS	THF
pH/pKa	-0.45	0.56	3.75 <sup>166</sup>	4.76 <sup>167</sup>	4.88 <sup>167</sup>	4.82 <sup>166</sup>	15.9 <sup>166</sup>	4.5 <sup>168</sup>	-----	-----

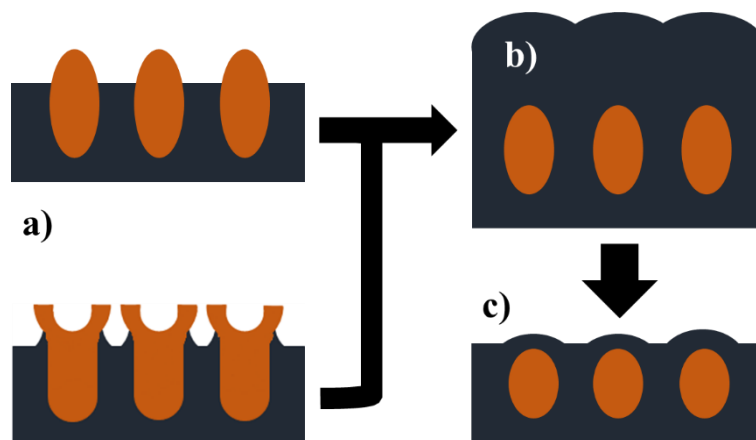


**Figure 4.3.24** Cut-away illustration of the swelling of the P2VP diblock copolymer thin films when exposed to THF vapors after exposure to the P2VP selective solvents. The black regions represent the PS matrix, and the orange represent the P2VP domains. a) Swollen P2VP raised cylinder or mushroom morphologies after selective solvent treatment, as in Figure 4.3.10c. b) Proposed THF swelling of the PS matrix, forcing the P2VP domains to collapse. c) Post-THF swelling morphology, similar to Figure 4.3.10b.

inability of the film to completely reset is due to the changes wrought in the P2VP cylinders, preventing their complete de-swelling.

**Selective Solvent Effect.** While THF's effect accounts for the general improvement in P2VP swelling, it does not explain why various solvents cause different swelling morphologies. Reviewing the results presented so far does not provide a clear answer either. While exposure methodology (vapor vs. soak) could be the culprit, it can't be the complete cause, since films soaked in AA form raised cylinder structures (Figures 4.3.5d, 4.3.6a). Nor is the defining factor clearly pH or pKa related. Solutions with a pH or pKa value below P2VP's generally swell P2VP significantly because of their ability to protonate it.<sup>159,168</sup> This explanation would predict that the

10% HCl solution would induce the most swelling (Table 4.3.5), which was clearly not observed (Tables 4.3.1, 4.3.2, and 4.3.3), and it cannot explain how P2VP is swollen by solvents with pKa's above its own (Table 4.3.5). Finally, it cannot explain the different swelling structures.

Given the apparent complexity of this story, we decided to first investigate if soaking or vapor exposing the films affected the structural morphologies. THF pre-treated films were soaked in, or exposed to vapors of, the P2VP selective solvents for various amounts of time. For all seven solvents, the films developed the previously shown morphologies (Figure 4.3.5a-d,g) after only one minute of soaking (Figure 4.3.25a-d,g), including their removal by PA and BA (Figures 4.2.2, 4.3.25e,f). Longer soaking times didn't yield any changes (Figure 4.3.26). Films exposed to vapors of FA, AA, and EtOH eventually developed the same morphologies as their minute soaked counterparts, but only after 48 hours (Figure 4.3.27). The exposure methodology, therefore, dictates how quickly the mushroom caps or raised cylinders form.

This explanation also covers the swelling behavior of the PA and BA exposed films. As shown in Figure 4.3.28, the raised horizontal cylinder's development during a vapor exposure can be monitored. After 10 minutes under PA or 60 minutes under BA, surface structures with the same characteristics (Figure 4.3.28a,iii,b,c) as the 15 minute PA exposures used in the rest of this work (Table 4.3.3) develop. With longer PA exposure, the P2VP cylinders lose their separation and merge together (Figure 4.3.28a,iv), until the surface morphology is lost (Figure 4.3.28a,v). The reduced water contact angle of the hour long PA exposed film (Figure 4.3.28a,v inset) indicates that this is due to the P2VP finally overflowing and coating the film's surface. All the swelling results of THF pretreated films that are then soaked in or exposed to vapors of PA or BA point to the raised cylinders being incomplete swelling of the P2VP domains. Thus, unlike for the other solvents, the exposure methodology is slightly involved in these structures' development,

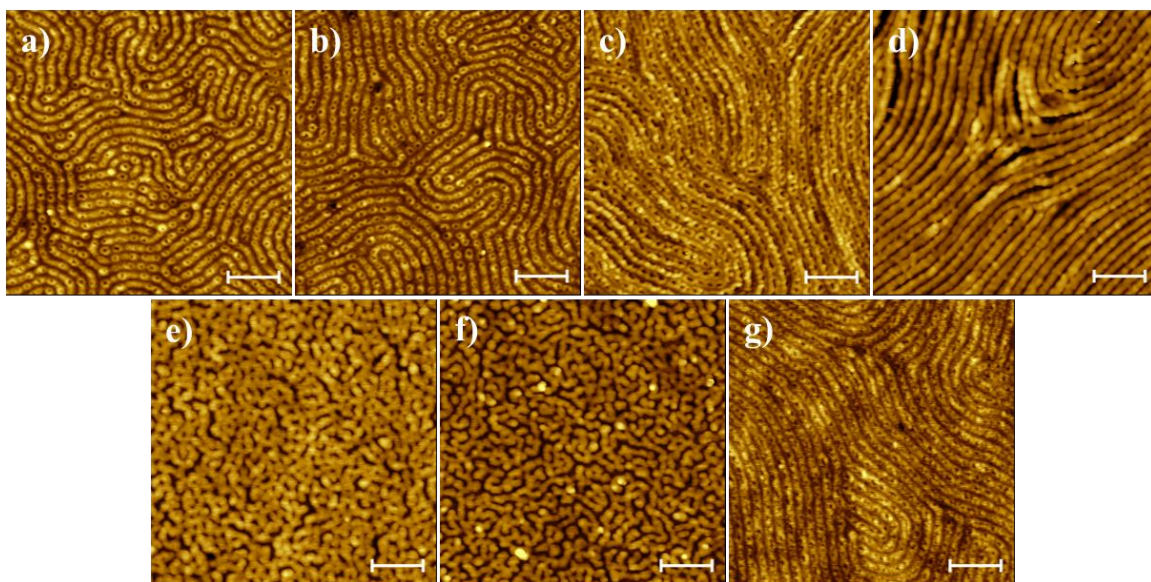


**Figure 4.3.25** AFM height micrographs of films exposed to THF vapors for 15 minutes, then soaked in a) 10% HCl, b) 1% HCl, c) FA, d) AA, e) PA, f) BA, or g) EtOH for 1 minute. All scale bars are 200 nm.

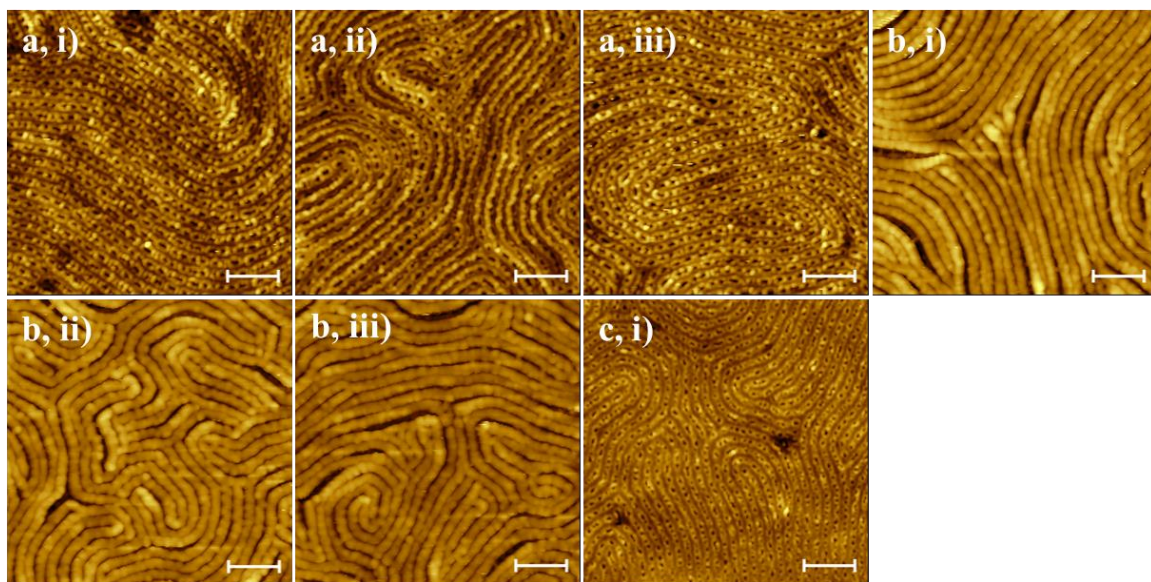


**Figure 4.3.26** AFM height micrographs of PS-P2VP diblock films soaked in a) FA, b) AA, or c) EtOH for i) 5 minutes, ii) 10 minutes, or iii) 30 minutes.

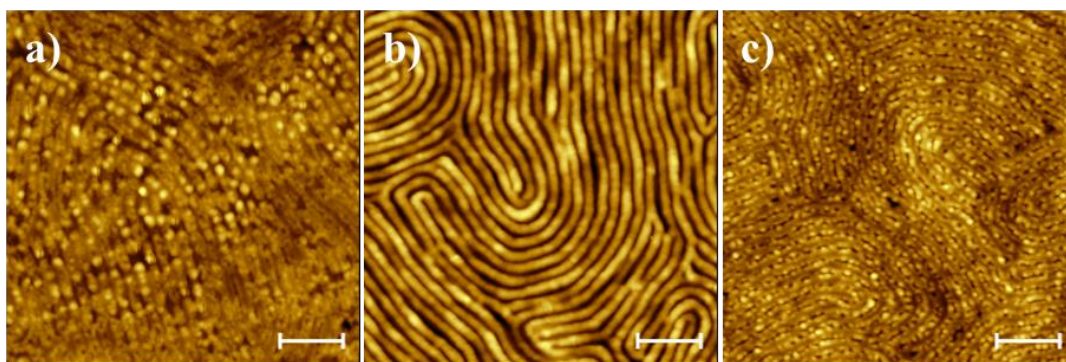


**Figure 4.3.27** AFM height micrographs of films pre-treated with THF, then exposed to vapors of a) FA, b) AA, c) and EtOH for 48 hours. All scale bars are 200 nm.

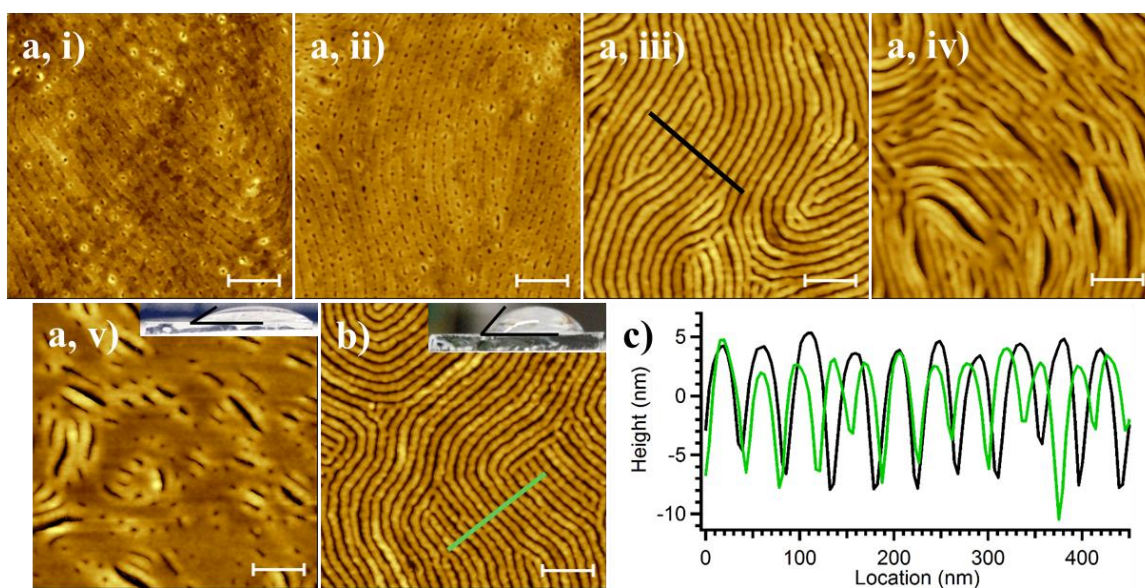


**Figure 4.3.28** AFM height micrographs films exposed to THF vapors for 15 minutes, then exposed to vapors of a) PA for i) 1 minute, ii) 5 minutes, iii) 10 minutes, iv) 30 minutes, v) 60 minutes, or b) BA for 60 minutes. c) Height profiles over the corresponding lines in a,iii) and b), with  $42.5 \pm 4.4$  nm period and  $10.4 \pm 1.6$  nm corrugation, and  $37.7 \pm 4.4$  nm period and  $8.27 \pm 2.1$  nm corrugation, respectively. The insets of a,v) and b) show the water contact angles of the films, which are  $33.5^\circ$  and  $48.4^\circ$ , respectively. All scale bars are 200 nm.

since the slower swelling afforded by vapor exposure allows them to be observed.

Since the exposure methodology does not dictate whether a film will swell into mushroom caps or raised cylinders, the root cause lies with differences between the solvents. Because no universal metric of solvent polarity exists, the P2VP selective solvents' pH or pKa values can be used to compare them instead (Table 4.3.5). Initially, these values do not seem to present a trend, since the 10% HCl solution, 1% HCl solution, and FA, which will swell P2VP by protonating it, and EtOH, which can only swell P2VP by hydrogen bonding with it, all form mushrooms. However, these solvents do share the similarity of being at least three-quarters of a pH unit away from P2VP's pKa, while the raised cylinder swelling solvents of AA, PA, and BA are all less than 10% above that value. This suggests that a complex swelling mechanism, but still based on hydrogen bonding, results in the raised cylinder morphologies. To investigate this, THF pre-treated films were soaked in 1% HCl solution, FA, or EtOH, then exposed to PA vapors (Figure 4.3.29a-c). In all three cases, the mushroom morphologies were converted into raised cylinders after PA exposure. Soaking a pre-treated, PA exposed film in FA could not convert the raised cylinders to mushroom caps (Figure 4.3.29d). This could only be achieved with an intermediate THF step (Figure 4.3.30), which is consistent with the idea of THF exposures after P2VP selective solvent treatments 'resetting' the films. The persistence of the mushroom cap morphologies after a film was soaked in FA twice means that the results of Figure 4.3.29a-c were caused by exposure to PA, as opposed to improved solvent uptake by the exposed P2VP (Figure 4.3.31).

PA's ability to transform the EtOH made mushroom caps into raised cylinders (Figure 4.3.29c), as well as the PA raised cylinders' inability to be transformed into mushroom caps by FA (Figure 4.3.29d), indicate that an electrostatic effect, in addition to hydrogen bonding, is involved in swelling the cylinders. These effects cannot be separated, as demonstrated by THF

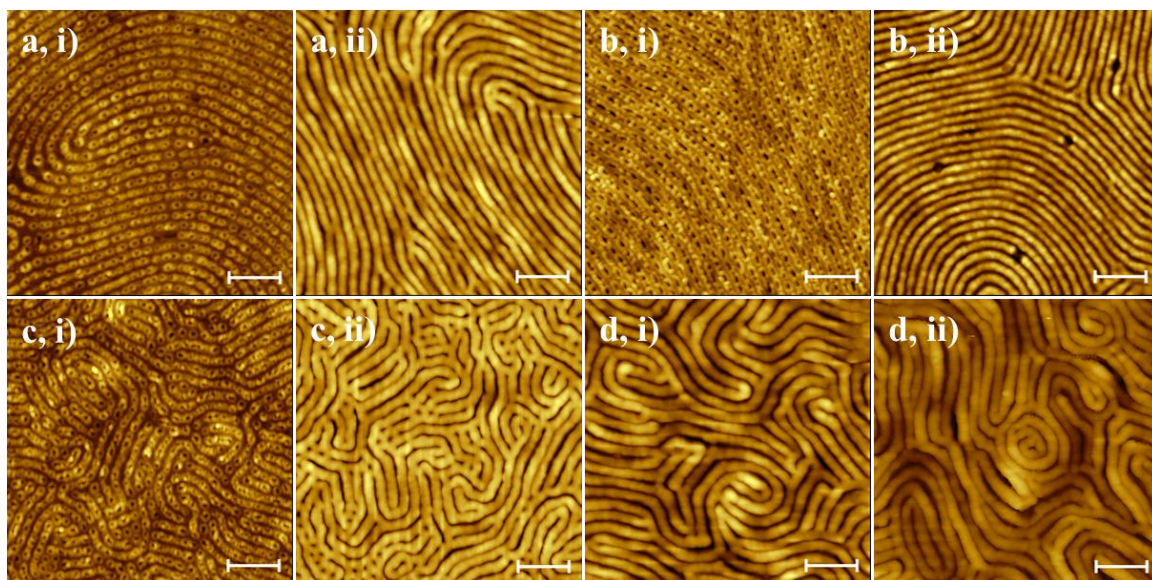


**Figure 4.3.29** AFM height micrographs films pretreated with THF, then soaked in a,i) 1% HCl, b,i) FA, c,i) EtOH, or exposed to vapors d,i) PA, then exposed to vapors of a,ii) – c,ii) PA, or soaked in d,ii) FA for 15 minutes All scale bars are 200 nm.

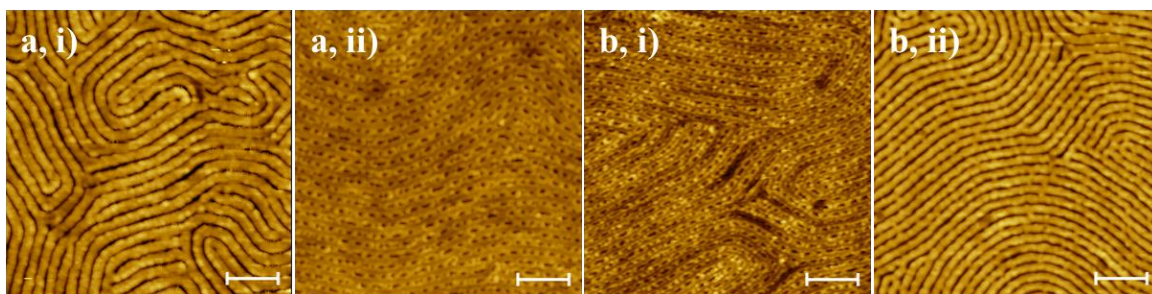


**Figure 4.3.30** AFM height micrographs of films exposed to THF, then a,i) PA, b,i) FA, then THF, then a,ii) FA, b,ii) PA. All scale bars are 200 nm.

pretreated films serially exposed to FA and EtOH only yielding mushroom caps (Figure 4.3.32). Therefore, we propose that the raised ridges occur due to nearly dissociated hydrogen bonds between AA, PA, or BA solvent molecules and the P2VP moieties. These solvents cannot protonate P2VP, but the closeness of their pKas to P2VP's suggests that their acidic hydrogen is

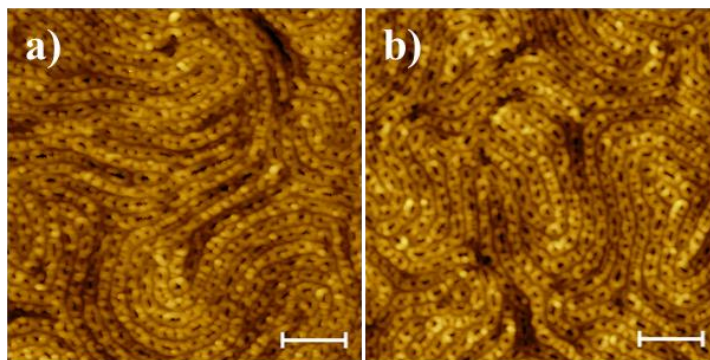


**Figure 4.3.31** AFM height micrographs of films pre-treated with THF, then soaked in a) FA for 15 minutes, then b) FA again for 15 minutes. All scale bars are 200 nm.

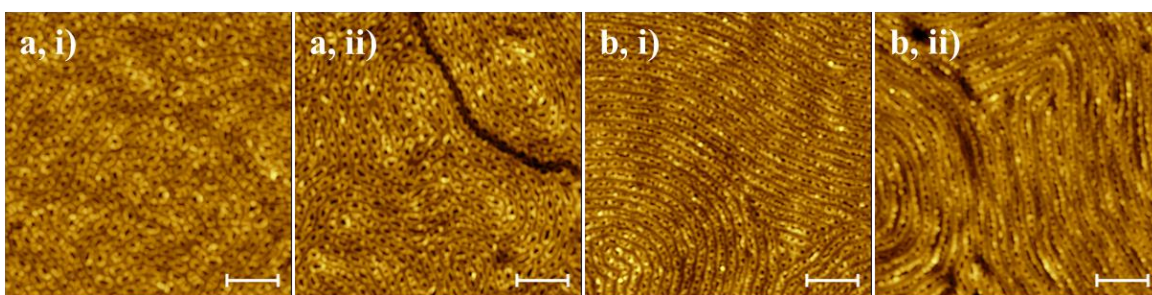


**Figure 4.3.32** AFM height micrographs of films pre-treated with THF, then soaked in a,i) FA or b,i) EtOH, followed by a soak in a,ii) EtOH or b,ii) FA for 15 minutes. All scale bars are 200 nm.

not closely held. This would yield a stronger hydrogen bond with P2VP's nitrogen group, much stronger than in the case of EtOH. As indicated by Figure 4.3.9c, the P2VP domains are significantly positively charged even when swollen by EtOH. Since the organic acids have not dissociated, carboxylate groups are also present within the P2VP domains. Their counterbalancing influence could reduce electrostatic repulsion issues that could promote mushroom formation.

**Gold Nanoparticle Alignment.** The presence of PS at the film's surface, and the charged nature of the exposed P2VP domains, will present challenges<sup>146</sup> when using this copolymer to deposit

and align NPs. However, the issues are not insurmountable. Having found a colloid that takes advantage of this diblock's peculiarities, we decided to explore the possibilities offered by this hybrid system. Thus, an aligned film was exposed to THF and PA vapors (Figure 4.3.33), and soaked in AuNPs for 24 hours. The small, negatively charged AuNPs showed the same selectivity for the exposed P2VP domains as before, creating a macroscopic, structural anisotropy that followed the P2VP cylinder alignment (Figure 4.3.34a). The film had a light pink color, with a weak plasmon resonance at 2.138 eV that was quite wide (full-width half-maximum (FWHM) of 0.77 eV) (Figure 4.3.34c). The film showed a small polarization dependent response, decreasing in absorbance by 8.7% when oriented against, as opposed to with, the incoming light's polarization (Figure 4.3.34d).

Since these AuNPs are commonly used to grow larger particles,<sup>6</sup> the AuNP coated film was exposed to a gold growth solution. During this process, the substrate's color changed to an intense blue, developing a much more intense plasmon resonance at 1.926 eV (Figure 4.3.34c). The larger AuNPs maintain the system's structural anisotropy, only coating the exposed P2VP domains (Figure 4.3.34b). The FWHM of the film shrank dramatically (0.43 eV), and it exhibits a greater polarization dependent response, dropping 12.1% in absorbance when oriented against the incoming light's polarization (Figure 4.3.34d). Unfortunately, this isn't mirrored in the reflectance data (Figure 4.3.35), but the film does show a slight shift in its plasmon resonance with orientation (90°: 1.935 eV, 0°: 1.9136 eV) (Figure 4.3.34d). The existence of these optical anisotropies is somewhat surprising, given the AuNP surface density, and thereby demonstrates the impressive ability and potential of this diblock copolymer film's to control NP deposition and alignment.

#### **4.4 Conclusion**

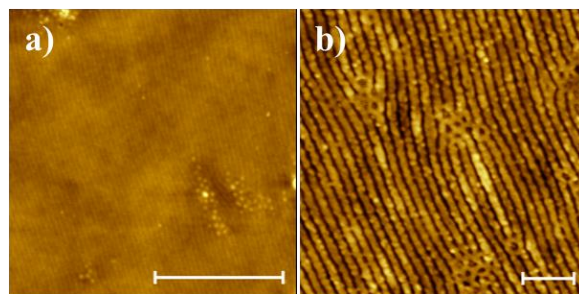


**Figure 4.3.33** AFM height micrographs of the film in Figure 4.3.34 after alignment, then 15 minute a) THF, and b) PA vapor exposures. The scale bar in a) is 1  $\mu\text{m}$ , and in b) is 200 nm.

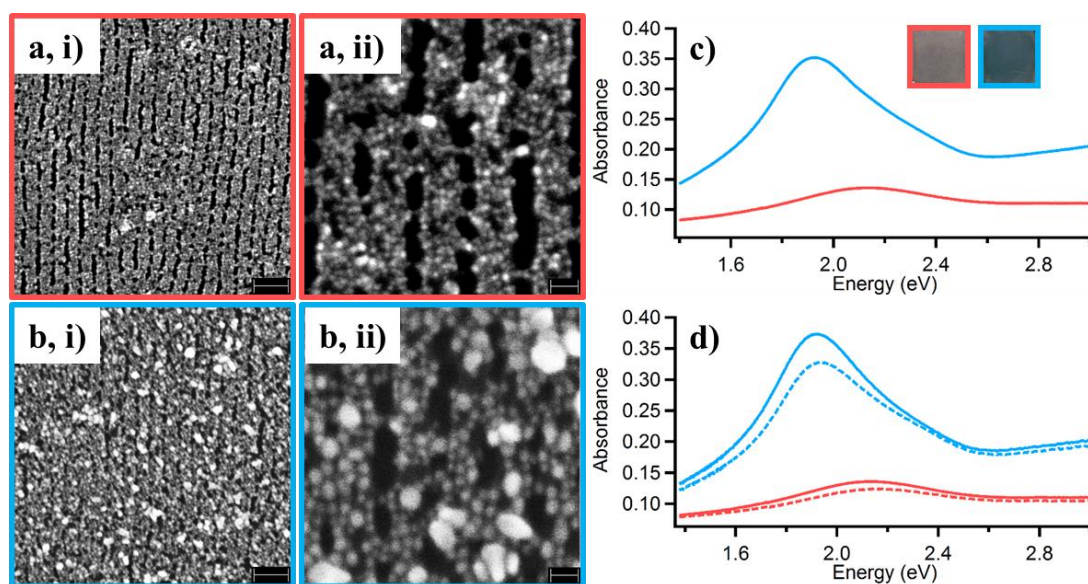


**Figure 4.3.34** P2VP diblock copolymer film aligned, pre-treated with THF, exposed to PA vapors for 15 minutes, then a) soaked in AuNPs for 24 hours, and then b) soaked in a gold growth solution for 15 minutes. The scale bars in i) are 100 nm, and in ii) are 20 nm. c) Absorption spectra of the substrates in a) (pink) and b) (blue). The insets are pictures of the films. d) Polarized absorbance spectra of the substrate in a) and b). The solid lines indicate the spectra obtained with the film aligned with the incoming light's polarization ( $0^\circ$ ), and the dashed lines indicate the spectra obtained when the film was aligned against the incoming light's polarization ( $90^\circ$ ).

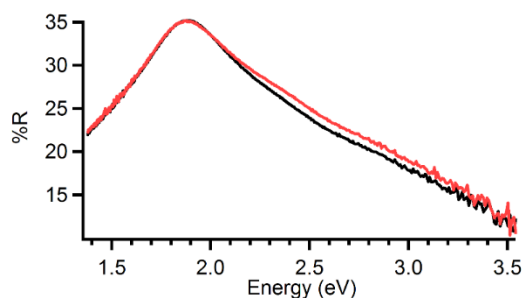


**Figure 4.3.35** Reflectance spectra of the film in Figure 4.3.34 after exposure to the gold overgrowth solution. The red line is the spectrum obtained when the film is aligned with ( $0^\circ$ ) the incoming light's polarization, and the black line corresponds to the spectrum obtained when the film is aligned against ( $90^\circ$ ) the incoming light's polarization

In conclusion, we investigated PS-P2VP diblock copolymer thin film swelling upon exposure to different P2VP selective solvents. With a THF vapor pretreatment, P2VP domain swelling significantly increases upon subsequent solvent exposure, occasionally yielding a unique, raised horizontal cylinder surface morphology. We determine that THF is a near-neutral solvent for the diblock, displaying a slight P2VP preference in freshly annealed films. However, after P2VP selective solvent exposure, THF can only swell the PS matrix due to fundamental changes that occurred in the P2VP domains. This has the unexpected result of de-swelling the films, eliminating their previous surface topographies.

These results indicate that THF promotes P2VP swelling due to its incorporation into the PS matrix. This would make the matrix slightly polar, and therefore more permeable to the P2VP selective solvents, allowing them better access to the P2VP cylinders. However, neither P2VP swelling morphology arise through traditional descriptions of copolymer swelling, resulting in PS still being present on the films' surfaces. Although the mushroom caps are consistent with polymer domains overswelling then collapsing, the P2VP only collapses into itself in this case, as opposed

to collapsing over the entire film. While these structures appear with periodicity within the P2VP domains, they are the results of local swelling events and not due to the development of Rayleigh instabilities. With further investigation, we show that these structures only occur when exposed to solvents with pHs or pKas very removed from P2VP's, indicating that exclusive P2VP protonation or exclusive hydrogen bonding to P2VP moieties yield this topography.

The development of the never-before-seen raised cylinders is more complex. They can only occur due to the P2VP domains swelling homogeneously across their entire length, and cannot result through a more swollen structure's collapse. A case can be made that the exposure methodology plays a role in their development, but this cannot explain how they arise. The solvents that induce these ridges have pKas above, but close to, that of P2VP's, meaning that hydrogen bonding is primarily responsible for these structures. However, the closeness of the pKas indicates that these hydrogen bonds will be exceptionally polarized, and suggests that the carboxylate groups of the AA, PA, and BA solvent molecules could help stabilize the cylinders. Finding that electrostatics play a role in these structures' swelling provides suggestive evidence for this idea.

Finally, we demonstrate that these substrates can serve as excellent templates for controlling AuNP assembly and growth, even though their surface is complex. By aligning the P2VP cylinder domains, we can control the AuNP alignment, and create densely packed films that exhibit long range structural and optical anisotropies. Having developed an understanding of this diblock copolymer's swelling, and demonstrated its utility for NP alignment, we believe these substrates can be integrated with other NP systems, thereby becoming a novel, exciting, springboard with which to study controlled NP assemblies and their optical properties.

#### **4.5 Pertinent Background Results**

As was mentioned at the beginning of the chapter, this project was conceived to expand the results of chapter 3 to the  $\text{cm}^2$  level. Thus, I initially attempted to shear-align the same PS-*b*-PMMA diblock copolymer used there, but encountered two unresolvable issues. After every alignment, the film surface lost its heterogeneity, appearing as if coated in some material (Figure 4.5.1). After some research, PS was identified as the culprit. Due to its larger volume fraction and preferential PDMS wetting at the alignment temperatures, PS would coat the film-PDMS interface during the alignment process, thereby burying the PMMA hemi-cylinders.<sup>169</sup> In addition to this, while an AA vapor treatment could express the PMMA domains, it could not change the film's surface topography, and demonstrated that we could not apply enough force to align the hemi-cylinders (Figure 4.5.1b).<sup>169</sup>

Thus, I went in search of a commercially available, cylinder forming, diblock copolymer with shear-force alignable thin films. The only system I could find that fit these requirements was the PS-P2VP diblock used throughout this chapter. Given the issues with PS-*b*-PMMA, I first focused on the diblock's alignment. Since the P2VP cylinders are encased in PS, this also required a P2VP selective solvent exposure, for which THF worked with great effect.<sup>152</sup> Having established control over this issue, I moved on to improving the diblock's corrugation. This was initially performed with long AA vapor exposures (~24 hour) after THF vapor treatments, and yielded raised cylinders with corrugation about half that in Figure 4.3.27b. Believing I finally had the film systems I wanted, I attempted to coat them with AuNRs. As can be guessed, this did not work (Figure 4.5.2a). While AuNRs appeared to occasionally deposit between the raised cylinders, they did not do so with any obvious regularity or reproducibility, and is most likely the result of the complex nature of these films' surfaces. However, it was this seemingly perfect system's failure that launched my investigation into this diblock copolymer film's swelling.

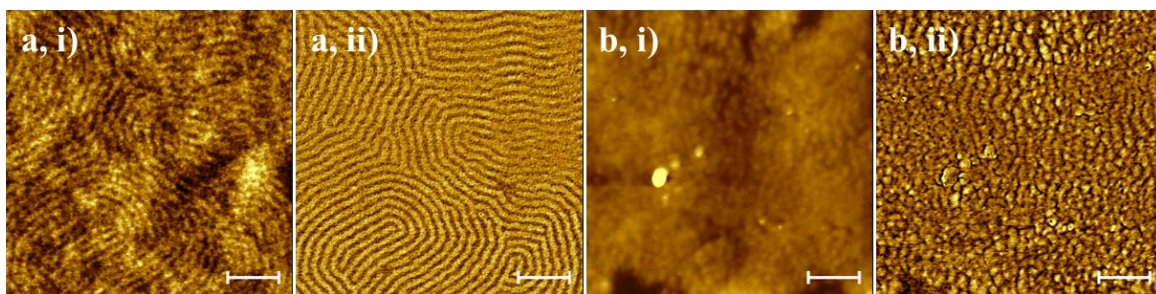


**Figure 4.5.1** i) Height and ii) phase AFM micrographs of PS-*b*-PMMA films like those used in chapter 3 after a) oven annealing, and b) shear-force alignment and 15 minute AA vapor treatment. All scale bars are 200 nm.

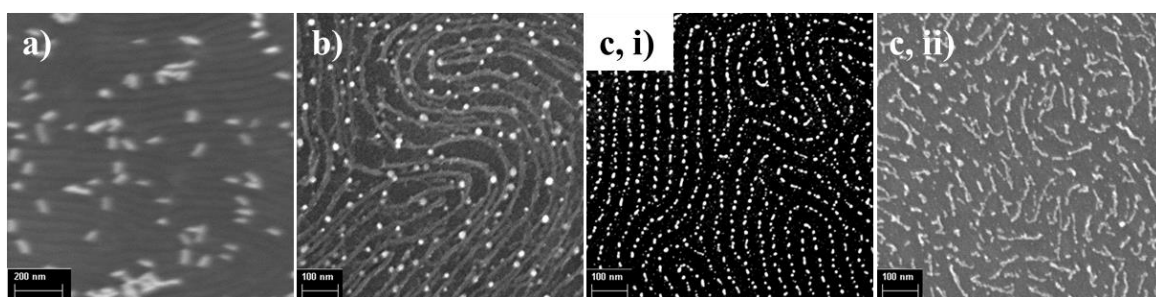


**Figure 4.5.2** a) Representative SEM image of the attempts to deposit AuNRs into the trenches of the PS-P2VP diblock copolymer films. b) PS-P2VP film soaked in a 10 mM HAuCl<sub>4</sub> in AA solution. c) PS-P2VP films exposed to THF and PA vapors, then soaked in a 10 mM HAuCl<sub>4</sub> in i) a 5% wt PA solution, or ii) a 20% wt PA solution.

As this work progressed, I was always considering the potential applications, advantages, and implications of my results. This PS-P2VP diblock has been successfully used to make thin, well defined metal fibers by intercalating the P2VP domain with negative metal ion complexes, then treating the system with oxygen plasma to reduce the metal and remove the polymer.<sup>152,156,159</sup> These reports almost exclusively use silicon substrates, in part because the only consistently reported way to intercalate the P2VP with gold required the use of hydrofluoric acid.<sup>152,159</sup> In

addition to what I could achieve with the AuBP seeds (Figures 4.3.8, 4.3.9, 4.3.34), I hoped my organic acid exposures might provide a way to intercalate  $\text{HAuCl}_4$  without HF, and therefore allow these fibers to be made on glass. This sort of worked (Figure 4.5.2b,c). My best results were obtained with AA, though a large amount AuNS biproducts were present in the system as well (Figure 4.5.2b). I had limited success by pre-treating a film with THF and PA vapor exposures, then soaking the film in different wt % solutions of PA and 10 mM  $\text{HAuCl}_4$  for three hours (Figure 4.5.2c). As I increased the percent of PA in the  $\text{HAuCl}_4$  solutions, the post-plasma gold structures became more fiber-esque (Figure 4.5.3c,ii). Unfortunately, due to time constraints, I have been unable to pursue this idea further.

## Chapter 5. On-going Projects

An overview of my two ongoing projects is contained in this chapter. In chapter 5.1, I cover my work as part of a collaboration to precisely assemble AuBPs and Ag/AuNSs on polymer –coated, ITO glass, and in chapter 5.2, I present my work to create and characterize AuBP – QD hybrid systems, both with and without collaborators. I describe the problems I encountered, and the solutions I employed during each project, and bring the reader up to date with their progress. These projects sought to exploit the AuBPs’ extreme electromagnetic field enhancement capabilities<sup>15</sup> (Figure 1.1.1b) in carefully designed constructs, enhancing the resulting systems’ optical properties. In the first case, we hoped to create arrays of AuBP – AgNS heterostructures with large SHG responses, and in the second case, we hoped to create AuBP – QD systems with enhanced PL properties.

### 5.1 Polymer Templated Gold Bipyramid – Silver Nanosphere Heterostructures with Large Second Harmonic Generation Responses

Collaborators: Dr. Xiaoying Liu, Dr. Yuval Yifat, Prof. Paul Nealey

Special thanks to: Prof. Norbert Scherer

Metallic nanostructures’ abilities to exhibit or enhance nonlinear optical (NLO) properties is well documented.<sup>170–175</sup> Because of the precise location and orientation control,<sup>170,171,175</sup> and the ability to make macroscopic arrays,<sup>172–174</sup> research into this topic has almost exclusively used top-down, lithographically defined structures. This was true until recently, when the Nealey lab developed a methodology that made arrays of various sized AuNSs with controlled the locations and

orientations on polymer coated, ITO substrates.<sup>176–178</sup> These structures also demonstrated enhanced SHG properties.<sup>176–178</sup> Given my work to this point, and the general research interests of our lab, we decided to collaborate to make the first multi-metal and multi-structure plasmonic NP arrays, then study their optical properties. We hoped that, by coupling the large electromagnetic field enhancements of a AuBP excited at its plasmon resonance to a AgNS with a LSPR at half that wavelength, we could make systems with impressive SHG abilities.

### 5.1.1 *Experimental Methods*

*New Materials.* Benzyltrimethylhexadecylammonium chloride (BDAC), poly(4-lithium styrene-sulfonic acid) (30 wt. % solution in water, PSS), hydrogen peroxide (30 wt. % solution in water, H<sub>2</sub>O<sub>2</sub>), and ammonium hydroxide (28 – 30 % NH<sub>3</sub>, NH<sub>4</sub>OH) were purchased from Sigma Aldrich and used without further purification. Sodium Sulfate ( $\geq 99.0\%$ ) and Sulfuric Acid (95-98%) were bought from Fisher Scientific and used without further purification. Hexadecyltrimethylammonium chloride (CTAC, >95%) was purchased from TCI and used without further purification.

*New Methods.* AuBPs were synthesized and cleaned as described in Chapter 2. They were then purified by soaking in synthesis-dependent concentrations of a BDAC solution at 30 °C overnight. The sample described here was soaked in 10 mL of a 125 mM BDAC solution for 10 hours. After this, the supernatant was carefully poured off, and the pellet resuspended with 10 mL of a 5 mM CTAB solution. To remove as much excess BDAC as possible, this colloid was centrifuged at 4000 g and 30 °C for 10 minutes, followed by the decanting of its supernatant and the resuspending of its pellet with 2 mL of NPH<sub>2</sub>O. To reduce the free CTAB concentration and allow high AuBP deposition on the substrates, the solution was centrifuged again, at 2000 g and 30 °C for 10

minutes, followed by its supernatant being decanted and its pellet being resuspended with 2 mL of NPH<sub>2</sub>O.

PSS coated AuBPs were prepared as described elsewhere.<sup>33</sup> After the first post-purification cleaning, the AuBP colloid was diluted to 2.1 mL with NPH<sub>2</sub>O water. It was then divided into seven, 300  $\mu$ L aliquots, to which another 1.2 mL of NPH<sub>2</sub>O were added. These were then centrifuged at 5000 *g* for 5 minutes, their supernatants decanted, and their pellets resuspended with 1.0 mL of NPH<sub>2</sub>O and 500  $\mu$ L of 0.1% wt PSS solution. The NPH<sub>2</sub>O must be added before the 0.1% wt PSS solution, or the colloid will irreversibly aggregate. The AuBPs were allowed to soak for 2 hours. After this, the aliquots were centrifuged at 5000 *g* for 5 minutes, their supernatants decanted, their pellets resuspended with 300  $\mu$ L of NPH<sub>2</sub>O, and then were recombined into a single solution. It is important to note that dividing the AuBP colloid into smaller aliquots improves overall yield after PSS functionalization. Attempts to perform this coating with larger volumes resulted in large numbers of AuBPs lost due to aggregation.

AgNS were synthesized as described elsewhere.<sup>179</sup> 47.5 mL of NPH<sub>2</sub>O were brought to boil in a round bottom flask with vigorous stirring. The silver precursor was prepared separately by mixing 1 mL of 34 mM Na<sub>3</sub>Cit, 1.47 mL of 10 mM AgNO<sub>3</sub>, and 30  $\mu$ L of 100 mM Na<sub>2</sub>SO<sub>4</sub> under vigorous stirring for 5 minutes. 50  $\mu$ L of 100 mM VC was added to the boiling NPH<sub>2</sub>O, and allowed to boil for 60 s. Then, the silver precursor was injected, and the reaction was allowed to run for 60 minutes. Due to the irreproducible nature of this synthesis, many tweaks to it were performed, including performing it under Ar. Unfortunately, nothing systematically improve the synthesis.

Ag coated AuNS were synthesized as described elsewhere.<sup>180</sup> A AuBP colloid was prepared as described in Chapter 2. To it was then added 3.75 mL of 160 mM CTAC solution, 750

$\mu\text{L}$  of 40 mM  $\text{AgNO}_3$  solution, and 750  $\mu\text{L}$  of 100 mM vit-C. The colloid was allowed to age for 20 hours at 70 °C, followed by centrifuging at 2000  $g$  and 30 °C for 30 minutes. The supernatant was decanted, the pellet resuspended with 10 mL of 50 mM CTAB solution, then aged at 30 °C for 4 hours. After this, the yellow supernatant, containing the Ag/AuNSs, and the grey pellet, containing the Ag coated AuBPs, were separated. The Ag/AuNS were centrifuged again at 4000  $g$  and 30 °C for 5 minutes, their supernatant decanted, and their pellet resuspended with 10 mL of  $\text{NPH}_2\text{O}$ .

The Ag coated AuBPs were resuspended to 5 mL with  $\text{NPH}_2\text{O}$ , then mixed with 100  $\mu\text{L}$  of base piranha (1:1 mixture of 30 wt % solutions of  $\text{NH}_4\text{OH}$  and  $\text{H}_2\text{O}_2$ ), and allowed to react for 16 hours to selectively remove the Ag overcoating. When this didn't appear to work, 200  $\mu\text{L}$  more of base piranha were added, and the pellets were soaked for another 6 hours. They were then centrifuged at 5000  $g$  and 30 °C for 15 minutes, their supernatants decanted, and their pellets resuspended with 2 mL of  $\text{NPH}_2\text{O}$ . Due to the lack of AuBP purity and yield, this process was abandoned as a purification technique.

AuBP-Ag/AuNS heterostructures on polymer coated, ITO glass were stored under vacuum when not being characterized, in order to prevent Ag oxidation. Dark field (DF) scattering spectra were recorded using a home-built microscope connected to a home-built spectrometer, similar to the setup used in Chapter 2.

### 5.1.2 Nanoparticle Synthesis Considerations

Two synthetic issues had to be addressed before the AuBP – Ag/AuNS arrays could be made. The first was improving the purity of the AuBP colloid,<sup>6</sup> since any remaining AuNS biproducts would bind to the places intended for AgNSs. The second was determining the right ligand conditions to

allow both the AuBPs and AgNSs to bind to the polymer surface. The Weizmann lab's recent development of a fairly straightforward methodology to separate the AuBPs from their AuNS biproduct<sup>9</sup> handled the purity issue. Utilizing the depletion zone interaction concept,<sup>181</sup> AuBPs were synthesized as described in Chapter 2, then purified by overnight soaking in BDAC. For this study, AuBP purity was vastly more important than AuBP concentration. Therefore, we used slightly lower BDAC concentrations than necessary to ensure high colloid purities (Figure 5.1.2.1). However, this does leave some AuBPs in the supernatant (Figure 5.1.2.1b). After purification, the colloid moves from being dark, wine-red in color to pink-brown, with the significantly reduced feature around 2.3 eV demonstrating the significantly improved purity of the colloid (Figure 5.1.2.1). The AuBPs' dimensions were calculated from TEM images.

While this technique is relatively simple, its implementation is a bit more complex. The BDAC concentration needed for purification is heavily dependent on AuBP size.<sup>9</sup> Since it is almost impossible to predict AuBP sizes before a synthesis, each colloid must be individually analyzed to determine its 'correct' BDAC concentration. I also found this process to be time sensitive, with similarly sized AuBPs soaked for 10, 11, or 12 hours requiring different ( $\pm 25$  mM) BDAC concentrations for purification. Other complications arise while decanting the supernatant. The depletion zone interaction theory<sup>181</sup> only indicates that the correctly sized NPs will sediment. Unfortunately, this sedimentation can happen on any surface of the container used to perform the soak, meaning a significant number of AuBPs can be lost during decanting. Relatedly, a thin film of residual supernatant coats the container walls after being decanted. This is almost exclusively AuNSs, and will settle on top of the pure AuBP sediment if not given enough time to drain. While the resulting purity issue could be corrected with another round of purification, the AuBPs eventually lose their sharp tips under these conditions,<sup>9</sup> negatively impacting their electromagnetic

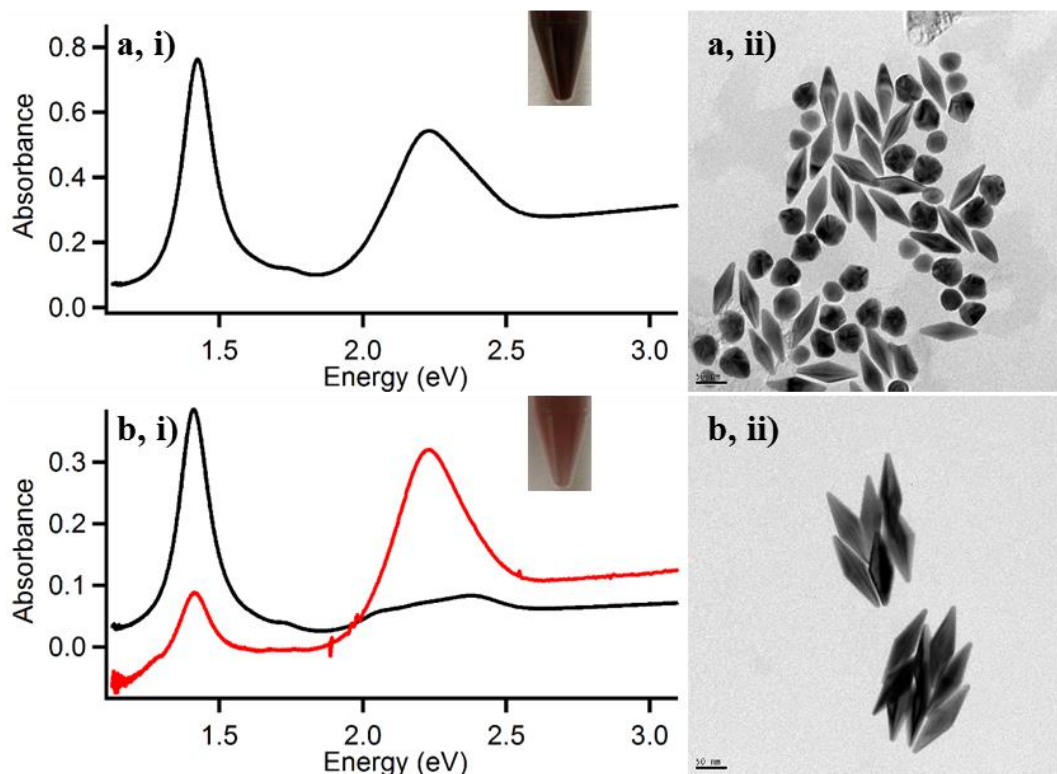


**Figure 5.1.2.1** a) As synthesized and b) purified AuBP colloids. i) UV/Vis spectra of the colloids, with the insets pictures demonstrating their color. The red line in b,i) is the UV/Vis spectra of the decanted supernatant. All spectra were recorded at the same concentration, or scaled to account for dilution effects. ii) Representative TEM images of the colloids. The particles in b) were used for this study, and have a plasmon resonance of 1.411 eV, and are 138.4 +/- 7.5 nm long, and 42.2 +/- 2.4 nm wide.

field enhancements (Figure 1.1.1b).<sup>15</sup> If purity issues are encountered, one subsequent soak at the optimum BDAC concentration can be performed without causing significant rounding. Finally, some of the purified AuBPs irreversibly aggregate during the post-purification centrifugation, further decreasing overall yield.

Having satisfactorily addressed the AuBP colloid's purity, we moved to addressing the NP ligand – polymer surface interaction issue. Given the previous work of the Nealey lab,<sup>176–178</sup> the fact that most AgNS syntheses use citrate as the capping agent,<sup>179</sup> and our lab's success in coating AuBPs in the negatively charged polymer PSS,<sup>33,50</sup> I initially decided to use negatively coated noble metal NPs for this project. Unfortunately, this encountered several problems. First, the PSS coated AuBP's surface density of was consistently low, indicating a poor interaction between the PSS and the polymer surface, and immediately limiting the potential yield of any AuBP – AgNS heterostructures. Second, even though citrate and PSS are negatively charged, the use of different capping agents actually increased the complexity of tuning the polymer – ligand interactions, as opposed to decreasing them. This usually resulted in one or the other NP depositing, but not both (Figure 5.1.2.2a). Lastly, the AgNS syntheses proved to be un-tunable and irreproducible (Figure 5.1.2.2b,c). Despite many synthetic attempts, I could not consistently synthesize spherical AgNP. If I did make AgNSs, they did not have a consistent size dispersity, and their LSPRs could not be shifted from ~400 nm in water. Given the LSPR's dielectric dependence,<sup>37</sup> and since our optical and SHG studies are performed in air, these AgNSs' LSPRs would be too blue to be useful.

The solution, as it turned out, was elegantly simple. Another recent methodology to purify the AuBP colloid involved overgrowing Ag on all of the AuNPs in the solution.<sup>180</sup> The Ag would coat the AuNSs isotropically, and the AuBPs anisotropically, creating large AgNSs and long AgNRs. The NPs would then separate, due to the extreme differences in their depletion zone interactions,<sup>181</sup> with the Ag encased AuBPs forming a pellet, and the Ag coated AuNSs remaining in the supernatant. While this method couldn't separate the AuBPs with enough purity or yield (Figure 5.1.2.3b,c), it did create a large number of Ag/AuNSs with LSPRs in water close to what we needed (Figure 5.1.2.3d). More importantly, these were also coated in CTAB, the original

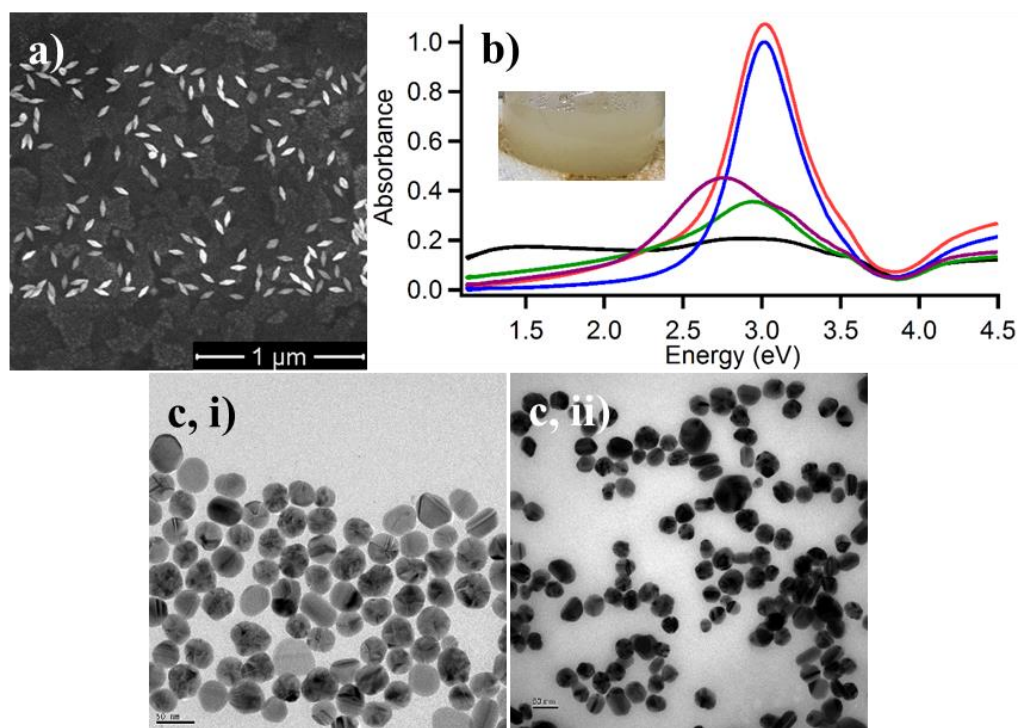


**Figure 5.1.2.2** Representative a) SEM image, b) UV/Vis spectra, and c) TEM images of the issues encountered when trying to use negatively coated noble metal NPs in this project. a) SEM image of the polymer patterned substrate after exposure to both PSS coated AuBPs and citrate coated AgNSs. Only the PSS coated AuBPs anchored to the polymer, and they did so with a low surface density. b) and c) Demonstration of the issues with reproducibly synthesizing AgNSs. b) UV/Vis spectra of several AgNS syntheses, with the inset showing the frequently achieved, bad cloudy-white, as opposed to clear yellow, solution color, and c) TEM images demonstrating the inability to reproduce similar AgNSs. The AgNS in c,i) are  $39.1 \pm 4.4$  nm, and the ones in c,ii) are  $42.5 \pm 8.4$  nm. The SEM image in a) was provided by Xiaoying Liu.

ligand of the AuBP synthesis. Since working with one NP ligand would simplify the polymer substrate optimization, CTAB coated, purified AuBPs (Figure 5.1.2.1b) and Ag/AuNSs were prepared (Figure 5.1.2.3d) to make the heterostructures.

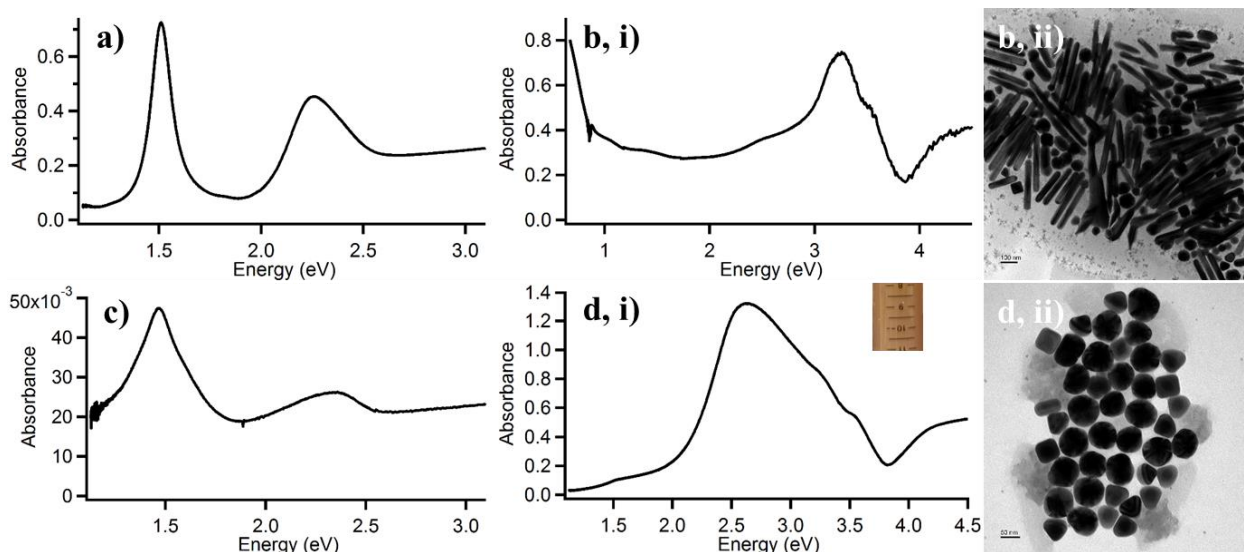


**Figure 5.1.2.3** UV/Vis and TEM images of AuBP colloid purified using the Ag overgrowth method. a) UV/Vis spectrum of as synthesized colloid. b,i) UV/Vis spectrum and b,ii) TEM image of Ag overgrown AuBPs. The plasmon resonance of the Ag overgrown AuBPs is located below 0.67 eV, where our cuvette begins to absorb. c) UV/Vis spectrum of Ag overgrown AuBPs after base piranha etch. d,i) UV/Vis spectrum, with the inset demonstrating the color, and d,ii) TEM image of Ag/AuNSs. These were the AgNPs used for the rest of this study, with a plasmon resonance at 2.627 eV, and are 75.9 +/- 7.3 nm in diameter.

One more synthetic tweak was required before we achieved success. Generally, the AuBP colloid is only high-g centrifuged once to concentrate it and remove excess reactants. A large amount of CTAB (estimated 2 – 5 mM) is still present after this, however, and since it is the AuBPs' CTA<sup>+</sup> ligands that attach them to the polymer surface, freely floating surfactant will interfere with the process. An additional, careful centrifugation removes enough CTAB to allow the AuBPs to stick to the polymer surface with high yield. Since the Ag/AuNS already bound well to the polymer surface, we immediately achieved AuBP – AgNS heterostructures.

### 5.1.3 Dark Field Optical Characterization

Having created these new plasmonic systems, we next needed to characterize their optical properties. Since we again have NPs on a substrate, this done with DF microscopy (Figure 2.2.1). In order to excite both the AgNSs' LSPRs and the AuBPs' LSPs, a Xenon arc lamp was initially used as a light source. Unfortunately, it was rendered non-viable due to its intense UV emission making all of our index of refraction matching, low fluorescence DF oil fluoresce blue (Figure 5.1.3.1). Thus, we investigated the near-IR spectra of the sixteen identifiable AuBP – AgNS structures. Of these, five didn't show a significant shift, eight were significantly blue shifted, and three were significantly red shifted from the isolated AuBP scattering spectra (Figure 5.1.3.2a). The heterostructures' plasmon resonances preserved the individual AuBPs FWHM (Figure 5.1.3.2c) and exhibit polarization dependent responses (Figure 5.1.3.2d), meaning their spectra are the result of a single, new plasmonic mode.<sup>20,74,95</sup>

While there is a correlation between the plasmon resonance of the heterostructure and the distance between its constituent AuBP and Ag/AuNS,<sup>28,89,182</sup> the precise nature of this relationship is limited by the SEM's resolution, and our desire to avoid electron beam induced damage<sup>183</sup> to the sample until all optical data has been collected. The coupling between plasmonic modes of separated NPs is strongly distance dependent.<sup>20,28,89,93,95,182</sup> Thus, the results of the five heterostructures with spectra almost unchanged from the individual AuBPs' are explained by their large interparticle gaps, which we confirm with our own simulations (Figure 5.1.3.3). Although the majority of our structures exhibiting extremely blue-shifted or red-shifted plasmon resonances was unexpected, the same phenomenon explains these results. The spectra of coupled noble metal NPs consistently red-shifts from their individual plasmon resonances with decreasing interparticle distance.<sup>20,28,89,93,95,182</sup> This continues until separations of about 1 nm are achieved, when electron



**Figure 5.1.3.1** Pictures taken through the eyepiece objective in our DF setup, demonstrating the blue fluorescence of the refractive index matching dark field oil caused by the Xenon arc lamp.

tunneling between the NPs can occur.<sup>93</sup> Now, the spectra move back toward the NPs' initial resonances, until they come into contact. This causes a completely new plasmon mode to appear.<sup>93</sup> Thus, we believe our heterostructures with resonances blue shifted from the AuBPs' are most likely touching each other, while the structures with significantly red-shifted plasmons have exceptionally small interparticle separations. As previously mentioned, the resolution limitations of SEM may prevent direct confirmation of this idea. Therefore, we are also conducting more simulations to probe this very small gap regime.

#### 5.1.4 *Second Harmonic Generation*

We are currently investigating the SHG properties of these heterostructures. Since the electromagnetic field enhancement in the gap between coupled, plasmonic NPs increases with decreasing interparticle distance,<sup>24,25</sup> we initially hoped to make heterostructures with as little separation as possible to achieve the maximum SHG.<sup>171</sup> However, these enhancements are also largest at the structures' plasmon resonances,<sup>24,25</sup> and given our unexpected optical results, we are now very interested in characterizing the SHG capabilities of all of our systems. Making

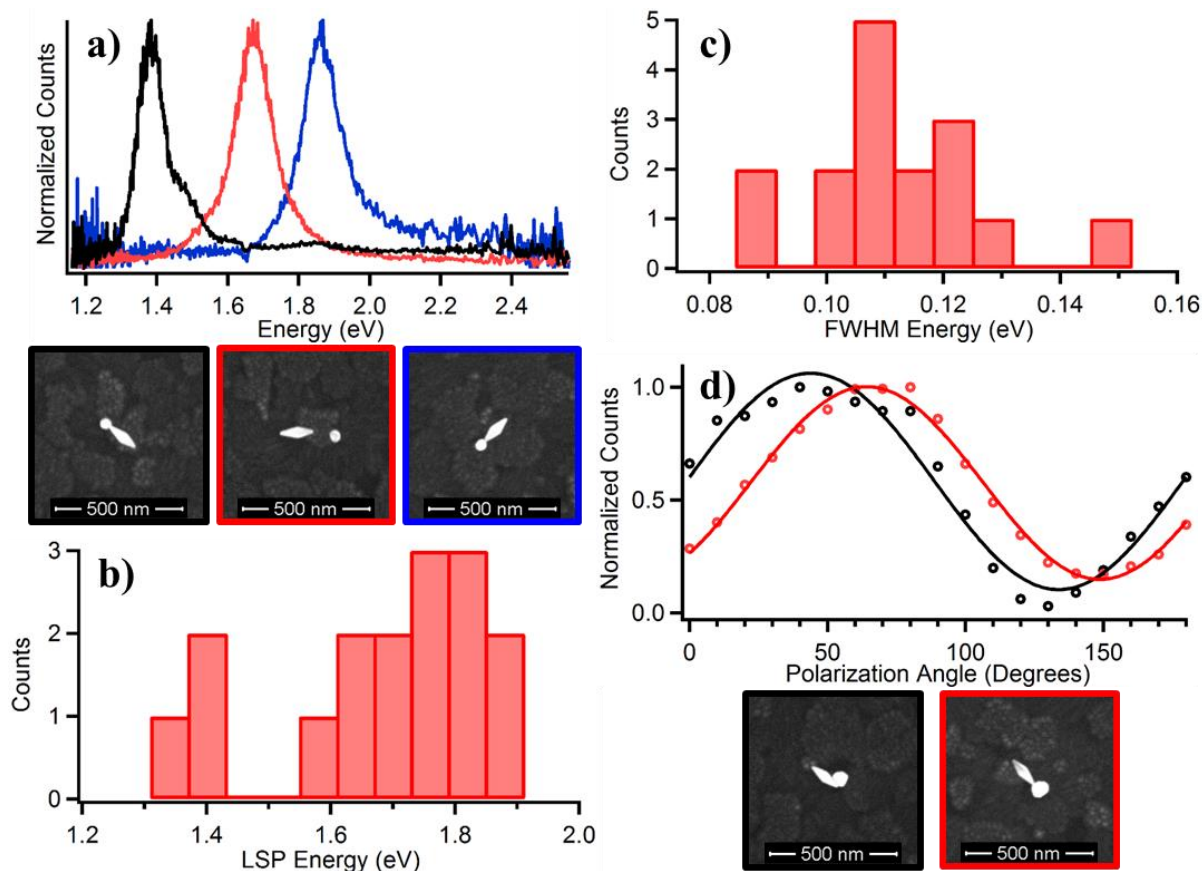


**Figure 5.1.3.2** Optical characterization of AuBP – Ag/AuNS heterostructures. a) Representative DF scattering spectra of the three kinds of structures observed, with SEM image insets color coded to the spectra. The individual AuBP resonance is  $\sim 1.65$  eV. b) and c) Histograms of the b) plasmon resonances and c) FWHM of the heterostructures (0.111 eV average). d) Representative DF scattering spectra, demonstrating the polarization dependence of the heterostructures' plasmon resonances. The SEM image insets are color coded to the spectra, and the polarization angle is set by the polarizer's orientation. All SEM images were provided by Xiaoying Liu.

these measurements has required some creativity and troubleshooting with our optical setup, as we work to ensure maximum photon efficiency at half of our excitation laser's wavelength ( $\sim 400$  nm). The setup is described in Figure 5.1.4.1.

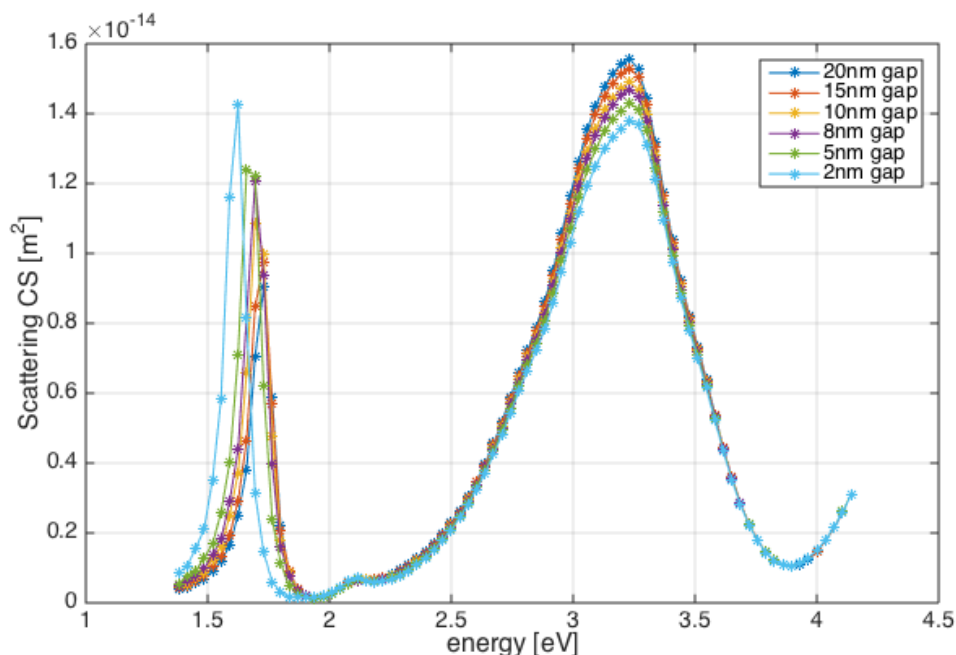


**Figure 5.1.3.3** Lumerical simulations of the AuBP – Ag/AuNS heterostructure’s plasmon resonances, as a function of decreasing interparticle separation. The AuBP LSP’s contribution is in the near-IR, and the Ag/AuNS response is located around 3.25 eV. Simulations probing the sub – 2 nm separation regime are being performed. Graph provided by Yuval Yifat.

### 5.1.5 Conclusion

As of the writing of this thesis, this collaboration has created, and theoretically and experimentally characterized, the first ever multi-metal and multi-structure plasmonic NP systems. We’ve overcome a variety of unexpected difficulties to ultimately prove the ability and versatility of this methodology to control the assembly of almost any noble metal NP. Our results open the door to making structures that were previously only the purview of lithography.<sup>175</sup> While these results are themselves exciting, we are currently working to characterize the NLO properties of these systems, hoping to demonstrate that they show significant SHG.

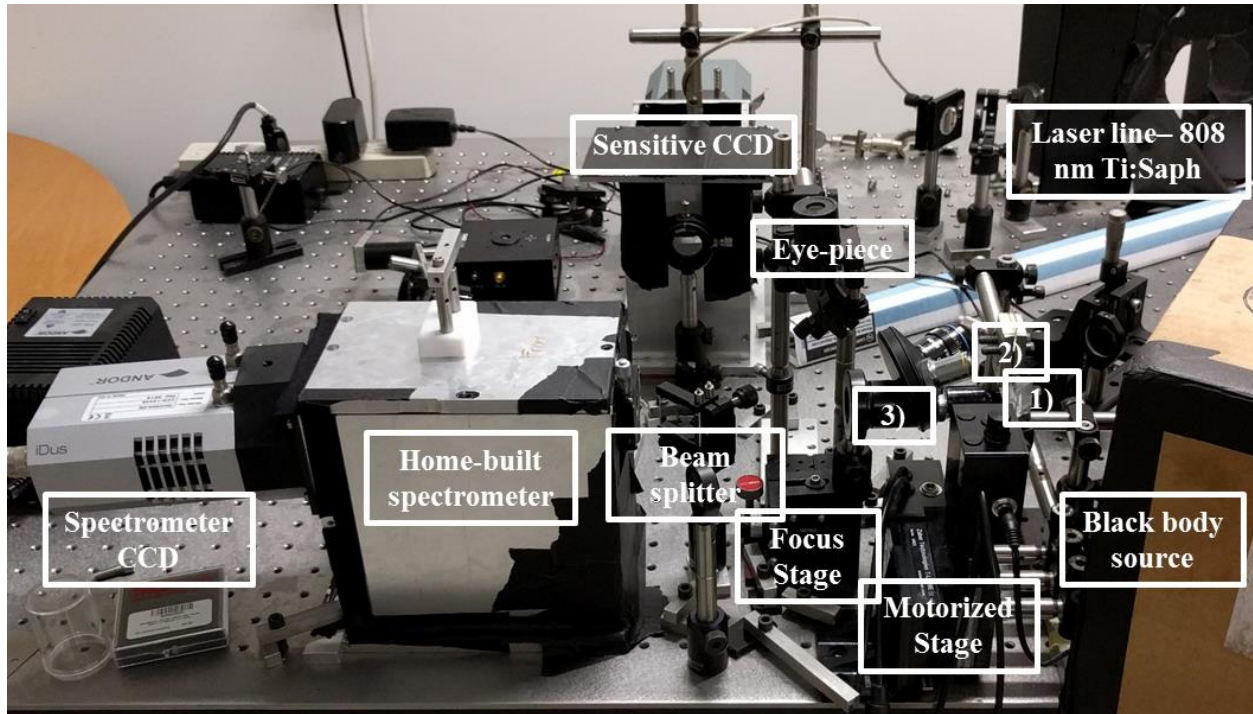


**Figure 5.1.4.1** Home built microscope system to collect DF scattering spectra, and SHG signal. 1) A prism, used so we can focus white and laser light from two different sources onto the sample. 2) The sample holder, and 3) the nose-piece and objectives. The setup is on a standard, Thor Labs optical table.

## 5.2 Gold Bipyramid – Quantum Dot Hybrid Structures with Enhanced Photoluminescence Properties

Collaborators: Kyle Gibson, Prof. Yossi Weizmann, Dr. Joe Austin, and Dr. Pedro Rodriguez

Special Thanks to: Igor Fedin, Prof. Dmitri Talapin, Dr. Pete Dahlberg, Sara Massey, Prof. Greg Engel

From Fermi's Golden Rule,

$$W_{2 \rightarrow 1} = \frac{\pi}{2} \left\{ \frac{\mu_{21} \cdot \vec{E}}{\hbar} \right\}^2 g(\omega) \quad (1)$$

where  $W$  is the transition rate,  $\mu$  is the dipole moment,  $\vec{E}$  is the electric field, and  $g(\omega)$  is the density of states, we know that the local electric field strength experienced by a fluorophore will influence its transition rates.<sup>31,32</sup> Thus, plasmonic NPs' electromagnetic field enhancements<sup>15</sup> will strongly affect the optical properties of emitters.<sup>32,184</sup> Unfortunately, the precise nature of this effect is complex, since it depends on the distance between the NP and fluorophore,<sup>15,184,185</sup> as well as the emitter's radiative ( $\gamma_r$ ) and non-radiative ( $\gamma_{nr}$ ) exciton recombination pathways:

$$W_{2 \rightarrow 1} = \left( \frac{\gamma_r}{\gamma_r + \gamma_{nr}} \right) \left( \frac{\pi}{2} \left\{ \frac{\mu_{21} \cdot \vec{E}}{\hbar} \right\}^2 g(\omega) \right) \quad (2).^{32}$$

These facts help elucidate why so many reports in the literature seem to be contradictory (only a selection are provided as references).<sup>184,186–198</sup>

Thus far, the majority of systems that demonstrated enhanced fluorescence due to emitter coupling with plasmonic NPs either involve spherical NPs,<sup>189,190,193</sup> or uncontrollable placing fluorophores near the plasmonic structure.<sup>184,186,187,192,194–196</sup> In the first case, similar structures have been reported as quenching PL,<sup>191,193,197,198</sup> and in the second, the critique that a large number of fluorophores could explain the observed PL enhancements is handled through some sort of normalization, where only the emitters within the region of ideal electromagnetic enhancement are the sources of PL events.<sup>187,192,195,196</sup>

The impetus of this project was to avoid these issues by making the ideal hybrid nanostructure involving a single plasmonic NP coupled to a single QD. By controlling the location of, and distance between, the QD and the noble metal NP, we could statistically study the electric field enhancement's effect on the QD's PL. AuBPs were picked as the plasmonic NP, since they exhibit the largest electromagnetic field enhancements of any noble metal NP,<sup>15</sup> and because the Weizmann lab was working to anisotropically coat them with polymers. If this coating could be achieved, similar to what is in the literature,<sup>75</sup> then we would be able to selectively place a QD

near a AuBP's tip, in the region of maximum electric field enhancement.<sup>15</sup> In this vein, DNA was chosen as the linking agent, due to its well defined length, and the Weizmann lab's work with DNA that coils and uncoils with changes in pH.<sup>199</sup> These strands offer a platform with which we could probe different interparticle separations with the same hybrid system, allowing us to controllably study the effect of distance on its PL properties. Fortuitously, recent advances in water solubilizing QDs also involved their functionalization with DNA, simplifying another aspect of this project.<sup>200</sup> Finally, the maximum enhancement conditions of matching the excitation laser's wavelength with the AuBP's and QD's pertinent optical properties,<sup>196</sup> could be achieved because of the tunability of these NPs' syntheses. This perfect storm of factors started this project, initially as a collaboration where I was to synthesize and water solubilize QDs, and then optically characterize the hybrid systems. Our ideal goal is depicted in Figure 5.2.1.1.

### 5.2.1 Experimental Methods

*New Materials.* Cadmium Oxide (99.99%, CdO), oleic acid (90%, OA), octadecene (90%, ODE), tellurium (99.997%, Te), octadecylphosphonic acid (97%, ODP), trioctylphosphine (90%, stored in glovebox, TOP), selenium (99.999%, Se), tetrachloroethylene ( $\geq 99\%$ , TCE), 1-decanthiol (96%, DT), 1-butanol (99.8%, anhydrous, BuOH), poly(maleic anhydride-alt-1-octadecene) ( $M_n$  30,000 – 50,000, PMAO), 11-azido-3,6,9-trioxaundecan-1-amine ( $\geq 90\%$ , stored in glovebox, N<sub>3</sub>-amine), N-(3-dimethylaminopropyl)-N'-ethylcarbodiimide hydrochloride (BioXtra, stored in freezer, EDC), N-hydroxysulfosuccinimide sodium salt ( $\geq 98\%$ , stored in glovebox, sulfo-NHS), sodium tetraborate (99.999%, stored under vacuum, NaBorate), poly(diallyldimethylammonium chloride) (very low molecular weight, 35 wt % in water, PDC), bromine ( $\geq 99.99\%$ , Br<sub>2</sub>), high purity hydrochloric acid (TraceSELECT, HCl), high purity nitric acid ( $\geq 69\%$ , TraceSELECT,

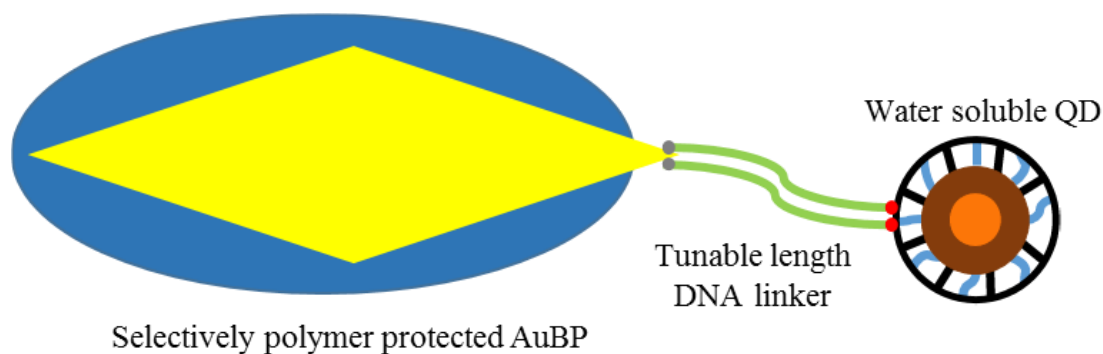


**Figure 5.2.1.1** Schematic depicting this project's ideal goal.

HNO<sub>3</sub>), and sucrose (≥99.0%) were purchased from Sigma Aldrich and used without further purification. 2-aminoethanethiol (95%, cysteamine) was purchased from Acros and used without further purification. Chloroform (0.75% EtOH as a preservative, CHCl<sub>3</sub>), glass coverslips (22 mm x 22 mm x 1 mm), and glass microscope slides were obtained from Fisher Scientific. The CHCl<sub>3</sub> was used without further purification, and the glass slides and coverslips were cleaned with piranha solution, rinsed thoroughly with NPH<sub>2</sub>O, and blown dry with N<sub>2</sub> before. All common glassware (round bottom flasks, condensers) and stir bars were cleaned in a base bath, rinsed with water, blown dry with N<sub>2</sub>, rinsed with chloroform and ethanol, and blown dry with N<sub>2</sub> again before use. Centrifuge tubes with 30 kDa membranes were purchased from Pall (microsepc), and were used as received. Hydrophillic PTFE 0.2 μm filters were bought from IC Millex and used as received. ICP-OES standards (Te: 100 μg/mL in 2% HNO<sub>3</sub> + trace HF, and Au: 100 μg/mL in 2% HCl) were bought from High Purity Standards and used as received. Polycarbonate ultracentrifuge tubes with their cap assembly were bought from Beckman Coulter and used as received. Secure-Seal Imaging Spacers (20 mm inner diameter, 0.12 mm depth) were bought from Grace Bio-labs and used as received.

*New instrumentation.* All ICP-OES experiments were performed on an Agilent Technologies 700 Series ICP-OES. The rotovap used in this study was an IKA RV 10, and borrowed from either the Weizmann or Talapin labs. The ultracentrifuge used in this report was a Beckmann LE-80, and along with the gradient mixer, was borrowed from the Engel lab. Cryo-TEM images were taken using either a FEI Titan or Spirit TEM. PL measurements were taken using a Horiba Fluorolog-3, with a 350 nm excitation wavelength.

*New Methods.* CdTe/CdSe core-shell QDs were synthesized as described elsewhere.<sup>201</sup> Cadmium oleate precursor (0.1 M, Cd(oleate)) was prepared by mixing 256.8 mg of CdO, 2.6 mL of OA, and 18 mL of ODE in a flask, degassing (heating the solution to 100 °C for 1 hour under vacuum), then cooking at 240 °C under Argon (Ar) for 30 – 120 minutes. It is important to run this reaction to completion, which is indicated by the solution being completely clear, as opposed to yellow, and to store it in under N<sub>2</sub> to prevent degradation. Lastly, this precursor turns solid at room temperature (RT), meaning it must be melted before use. Te precursor was prepared fresh before each reaction by mixing 12.8 mg of Te, 50.2 mg of ODPa, 1 mL of ODE, and 0.15 mL of TOP at 80 °C under vigorous stirring and N<sub>2</sub> for 40 – 60 minutes. CdTe QD cores were synthesized by heating 2 mL of the 0.1 M Cd(oleate) precursor with 1 mL of ODE to 280 °C under Ar, then injecting all of the Te precursor. The reaction was allowed to run for 3 – 3.5 minutes, before being quenched by cooling to RT with blown air. The colloid goes from clear red-orange to milky-orange in color as it cools, with extremely bright yellow-green PL that is observable by eye. These QDs are not cleaned prior to shell growth, and are stored under N<sub>2</sub> to ensure stability.

The selenium precursor (0.085 M, TOPSe) was made by mixing 71.0 mg of Se, 1.6 mL of TOP, and 9 mL of ODE with stirring and mild heat (~50 °C) under N<sub>2</sub>. The CdSe shell was grown on the CdTe cores by heating half of the premade CdTe QD colloid to 230 °C under Ar, then very

carefully adding alternating aliquots of the Cd(oleate) and TOPSe precursors. This is very painstaking, and generally consists of adding 2 – 3 drops of Cd(oleate), waiting 60 s, then adding 2 – 3 drops of TOPSe, waiting 60 s, and repeating. If more than the prescribed amount of either precursor is accidentally added, increase the waiting time to 4 – 5 minutes to ensure that as much precursor has reacted as possible before continuing. Aliquots are removed, diluted with CHCl<sub>3</sub>, and checked using UV/Vis and PL to monitor shell growth evolution. For the CdTe/CdSe QDs used in this study, this process takes 6 – 7 hours, and uses ~2.5 mL of each precursor. Once the QDs with the desired properties have been achieved, the reaction is cooled to RT with blown air, and the QDs precipitated by centrifuging at 3000 rpm for 15 minutes, with BuOH used as the nonsolvent. The supernatant is decanted, the pellet dried with N<sub>2</sub>, and then resuspended with TCE and stored under N<sub>2</sub>. The CdTe and CdTe/CdSe QDs are compared in Figure 5.2.1.2.

The concentration of the CdTe/CdSe QDs was determined using ICP-OES. An aliquot of the QDs was cleaned with BuOH at 3500 rpm for 10 minutes. The supernatant was discarded, and the pellet dried with N<sub>2</sub>. 3 – 5  $\mu$ L of Br<sub>2</sub> were then added to the pellet, followed by 2 mL of NPH<sub>2</sub>O and sonication. Finally, the solution was diluted to 5 mL with NPH<sub>2</sub>O. 1, 10, and 25 ppm standards were made by appropriately diluting the 100 ppm Te standard to a final volume of 5 mL in NPH<sub>2</sub>O. Because the ICP-OES has a saturation limit of 25 ppm, estimating the QD concentration assuming 100% precursor efficiency is necessary to ensure accurate results.

QDs were water solubilized similar to the method described elsewhere.<sup>200</sup> While the water solubilization procedure is the same, no matter how the QDs will be used, the PMAO must be amine functionalized if the QDs are to be coated with DNA. To this end, a 0.2 M solution of PMAO in anhydrous THF was mixed with N<sub>3</sub>-amine to functionalize 80% of its maleic moieties (this corresponds to 31.76  $\mu$ L of N<sub>3</sub>-amine per mL of 0.2 M PMAO) at 55 °C for 1 hour under

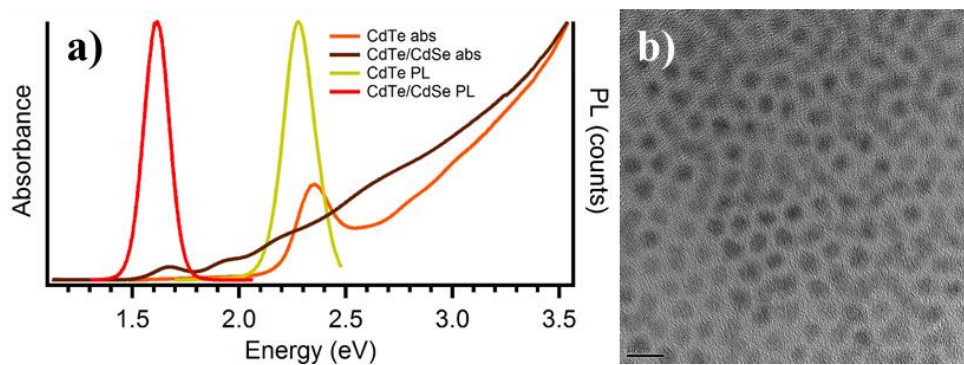


**Figure 5.2.1.2** a) Normalized UV/Vis and PL data of CdTe core and CdTe/CdSe core-shell QDs used in this report. b) TEM image of CdTe/CdSe core-shell QDs in a), which are  $4.63 \pm 0.46$  nm in diameter.

stirring and  $N_2$ . The solution was then cooled to RT overnight, still being stirred. Then, the THF was rotovapped off (RT bath, 20 rpm, ~170 mbarr of pressure for 1 hour), leaving behind a gooey, fluorescent substance. This was resuspended to its native volume with  $CHCl_3$ . For QDs not being functionalized with DNA, a 0.2 M PMAO solution in  $CHCl_3$  was made directly. An aliquot of CdTe/CdSe QDs was removed, cleaned with BuOH at 3500 rpm for 10 min, and resuspended with  $CHCl_3$ . To this was added an aliquot of the 0.2 M PMAO solution, such that the final solution volume was 20 mL, and the ratio of PMAO monomers to the surface area of the QDs was a 100 – 300x excess. Explicitly, my best results were obtained by cleaning 472  $\mu$ L of a 5  $\mu$ M CdTe/CdSe QD solution, resuspending it with 19.132 mL of  $CHCl_3$ , then adding 868  $\mu$ L of 0.2 M PMAO. The solution was heated at 70  $^{\circ}C$  for 30 – 40 minutes, then allowed to cool to RT (~2 hours). It was then rotovapped at 35  $^{\circ}C$  and 20 rpm. For the first 10 minutes, a 500 mbarr pressure was used to remove the dissolved gasses. Then, the pressure was decreased to 350 mbarr for 2 – 3 hours, followed by a further decrease to 200 mbarr for 15 minutes to dry the sample. The solid was then resuspended with a 75 mM NaBorate solution, under heated (~40  $^{\circ}C$ ) sonication for 2 – 3 hours.

To remove large aggregates, the solution was filtered using hydrophilic, PTFE syringe filters with 0.2  $\mu\text{m}$  pores. To remove the empty polymer micelles,<sup>200</sup> the solution must be ultracentrifuged. Therefore, the QDs were concentrated by centrifuging at 6000  $g$  for 10 minutes in centrifuge tubes equipped with a 30 kDa membrane, then resuspended to a final volume of 1 mL with  $\text{NPH}_2\text{O}$ . A 30% - 70% wt/wt sucrose gradient was prepared in ultracentrifuge tubes using a standard gradient mixer. This is time consuming, since so much sucrose is needed that the volume of the solid impacts the volume of the solution. Thus, the sucrose must be pre-dissolved, its volume checked, then diluted to the final volume. After this, the QDs were carefully added to the top of the gradient. This is important, because if the gradient gets mixed, this entire process is rendered useless. The QDs are then centrifuged at 30,000 rpm for 5 hours at RT. These ultracentrifugations were performed in pairs to ensure the ultracentrifuge remained balanced. Due to the extraordinary  $g$  forces exerted on them, the tubes (gradient, sample, tube, and top) must match within 0.1 g, to prevent dangerous unbalancing, and must be completely filled completely, to prevent crumpling. These tubes have a volume of 25 mL, of which I used  $\sim$ 24 mL for the sucrose gradient, and  $\sim$ 1 mL for the sample. After centrifuging, the samples were decanted, and centrifuged using the tubes equipped 30 kDa membrane to remove residual sucrose and concentrate the sample. This involved spinning the samples at 6000  $g$  and RT for 10 minutes, decanting the supernatant, diluting the solution with  $\text{NPH}_2\text{O}$ , and repeating. The samples were resuspended to a final volume of 1 mL, and an aliquot was dissolved in 3 – 5  $\mu\text{L}$  of  $\text{Br}_2$  under sonication for ICP-OES analysis, as described above. The water soluble QDs ( $\text{H}_2\text{O}$  – QDs) to be functionalized with DNA and bound to AuBPs were given to the Weizmann lab at this time. Figure 5.2.1.3 outlines the entire water solubilization process.

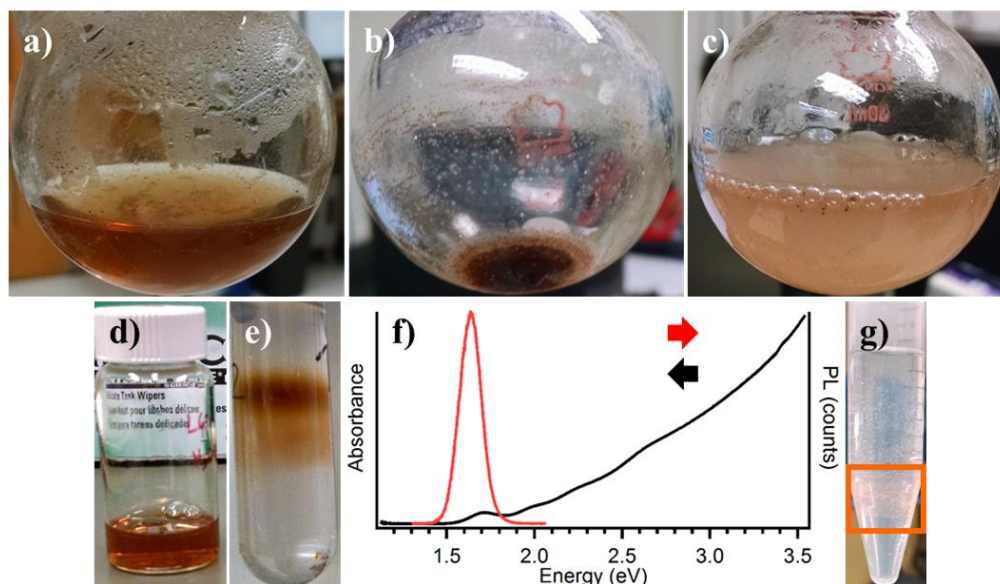


**Figure 5.2.1.3** Characterization of the QD water solubility process. a) Picture of QD-polymer mixture in  $\text{CHCl}_3$ . b) Picture of QD-polymer mixture after rotovapping. c) Picture of QD-polymer mixture after resuspension with NaBorate. d) Picture of QD – polymer mixture after 0.2  $\mu\text{m}$  filtering to remove large contaminants. e) Picture of QD polymer mixture after ultracentrifugation. The band spreading is due to either dispersity in QD size, QD aggregation during the water solubility process (precipitate at the bottom), or the sucrose gradient smearing. f) UV/Vis and PL of water solubilized QDs, unchanged from the stock solution. g) Picture of the orange precipitate, highlighted with the orange box, which occurs when CdTe/CdSe QDs are dissolved with aqua regia for ICP-OES measurements.

For liquid cell experiments, AuBPs were synthesized as described in chapter 2, then purified and PSS functionalized as described in chapter 5.1.1. Glass coverslips were functionalized with PDC as described elsewhere.<sup>50</sup> After cleaning, the coverslips were soaked in a 0.1 wt % solution of PDC for 2 hours, then rinsed with  $\text{NPH}_2\text{O}$  and blown dry with  $\text{N}_2$ . The coverslips were then soaked, face up, in a 1/50<sup>th</sup> dilution of a purified AuBP colloid for 75 – 105

seconds, then rinsed thoroughly with  $\text{NPH}_2\text{O}$ , and blown dry with  $\text{N}_2$ . To create the liquid cell, the adhesive secure-seal spacer was carefully placed on a clean glass microscope slide. It is very important, and difficult, to place this spacer uniformly on the slide to ensure that no leakage occurs. 100  $\mu\text{L}$  of an extremely dilute solution of  $\text{H}_2\text{O}$  – QDs ( $\sim 1/20,000^{\text{th}}$  dilution) was placed in this well, and the coverslip, AuBP side down, was carefully placed and pressed onto the top of the adhesive.

For my attempts to create AuBP – QD hybrids in solution, the concentration of the purified, PSS coated AuBPs was determined by removing an aliquot of the colloid, dissolving it with 500  $\mu\text{L}$  of aqua regia, then diluting it to a final volume of 5 mL with  $\text{NPH}_2\text{O}$  for ICP-OES analysis. This is done because the ICP-OES can only work with solutions that are, at most, 10% acid by volume. 1, 10, and 25 ppm Au standards were made by diluting the 100 ppm Au standard as needed for a 5 mL final volume. Having determined their concentration, the PSS coated AuBPs were soaked in a 2000x surface-area excess of cysteamine at RT for 9 hours. Explicitly, this involved soaking 200  $\mu\text{L}$  of a 230 pM AuBP solution in 18.4  $\mu\text{L}$  of a 5  $\mu\text{M}$  cysteamine solution overnight. The colloid was then centrifuged at 5000 g for 2 minutes, and its supernatant decanted to remove excess cysteamine. The pellet was resuspended to 100  $\mu\text{L}$  with  $\text{NPH}_2\text{O}$ . The  $\text{H}_2\text{O}$  – QDs were mixed with a 10,000x PMAO monomer excess of both sulfo-NHS and EDC, enough acid to reduce the solution's pH to 5, and allowed to react at 40  $^\circ\text{C}$  for 8.5 hours. Explicitly, this involved mixing 200  $\mu\text{L}$  of a 3.3  $\mu\text{M}$   $\text{H}_2\text{O}$  – QD solution with 10  $\mu\text{L}$  of a 1.53 mM HCl solution, 660  $\mu\text{L}$  of a 10 mM sulfo-NHS solution, and 660  $\mu\text{L}$  of a 10 mM EDC solution. The QDs were cleaned by centrifuging at 5000 g for 5 minutes with a centrifuge tube that had a 30 kDa membrane, then being resuspended to a final volume of 20 mL with  $\text{NPH}_2\text{O}$ . 50  $\mu\text{L}$  of the cysteamine functionalized AuBPs, and 6.97  $\mu\text{L}$  of the EDC/sulfo-NHS  $\text{H}_2\text{O}$  – QDs were mixed, and allowed to react

overnight. For UV/Vis and PL measurements, the colloid was diluted to a final volume of 500  $\mu$ L with NPH<sub>2</sub>O.

Cryo-TEM samples of all solution prepared AuBP – QD hybrids were made by Joe Austin and Pedro Rodriguez, who also took some images using a FEI Titan TEM. The cryo-TEM images I took were obtained using the FEI Spirit TEM, using its cryo-holder attachment.

### 5.2.2 Synthetic Considerations

The first problem was to find a suitable QD system for this study. This was somewhat difficult, since there are not many syntheses to make near-IR emitting QDs that match the AuBPs' plasmon resonances, and I couldn't reproduce some of the literature results.<sup>202,203</sup> After several attempts, I settled on a synthesis used by a former lab member that entailed growing a CdSe shell on a CdTe QD core.<sup>201</sup> Making the CdTe QDs was easy, and the QDs were quite stable if stored under N<sub>2</sub>. Unfortunately, growing the CdSe shell was quite painstaking, due to CdSe's ready ability to independently nucleate (Figure 5.2.2.1a). These CdSe QDs cannot be removed from the synthesis, give the colloid orange PL (~630 nm) that is visible by eye, and disrupts the shell growth because the Cd(oleate) and TOPSe precursors preferentially nucleate on them. This not only results in a more material and time being spent on this synthesis than necessary, but also renders the synthesis unusable. As was alluded to in the experimental methods, this can only be prevented by waiting long enough between adding the Cd(oleate) and TOPSe precursors, to ensure that their concentrations are kept below the CdSe nucleation limit. In addition to this, cleaning these QDs turned out to be non-trivial. Methanol and ethanol, the standard polar, non- solvents used to precipitate QDs and allow excess reactant removal, didn't work. Acetone, another such solvent, etched the QDs. After some experimentation, I found that BuOH was the only solvent that would

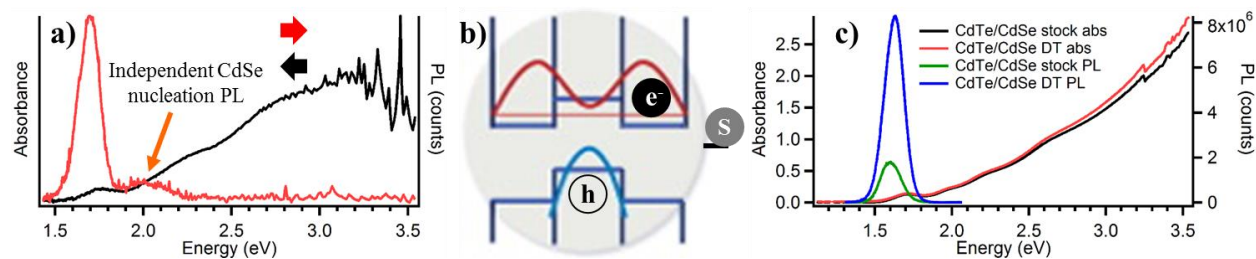


**Figure 5.2.2.1** Characterizations of CdTe/CdSe core-shell QDs. a) Demonstration of the CdSe independent nucleation during the synthesis, as seen by the PL shoulder around 2.0 eV. The data is recorded on a different instrument than the rest of the optical data in this text, hence its increased noise. b) Scheme depicting the type-II band structure of these thick CdTe/CdSe QDs, and the role of DT in increasing their PL. The black line covered by the grey sulfur atom depicts a passivated, surface trap state. c) Comparison of the UV/Vis and PL spectra of a stock CdTe/CdSe QD aliquot, and one treated with DT, demonstrating the  $\sim 4x$  PL increase. Figure 5.2.2.1b is adapted with permission from ref. 201. Copyright 2014 American Chemical Society.

consistently precipitate the colloid.

While these QDs' optical properties can be pushed into the near-IR with thicker CdSe shell growth, they exhibit relatively low PL due to their band structure (Figure 5.2.2.1b).<sup>204,205</sup> This occurs either due to the decreased overlap of the electron and hole's wavefunctions, thereby decreasing their recombination probability,<sup>201</sup> or by the electron becoming sequestered by surface trap states, decreasing the probability of radiative recombination.<sup>206</sup> Regardless, the QDs exhibited sufficient post-synthesis PL to be usable to make the AuBP – QD hybrids (Figures 5.2.1.2a, 5.2.2.1c). Then, through a fortuitous experiment, I managed to increase the QDs' PL by at least 4x (Figure 5.2.2.1c), simply by changing their capping ligands from TOP to DT. The exchange is very easy, consisting of cleaning the dots as described above, resuspending them with TCE, then

adding a significant excess of DT, followed by another cleaning and resuspension. Given a previous study in the literature,<sup>207</sup> and the belief that these QDs' low PL was predominantly caused by the lack of wavefunction overlap,<sup>201</sup> this result wasn't expected. It indicates that electron surface trap states<sup>206</sup> play a significant role in reducing these QDs' PL. Thus, the PL increase can be understood as the result of DT's electron rich sulfur atom<sup>206</sup> passivating electron surface trap states on the CdSe shell, thereby allowing more radiative recombinations (Figure 5.2.2.1b).

The next issue to address was how to water solubilize the QDs. Due to known issues with direct ligand exchanges,<sup>207,208</sup> and our desire to use DNA as a linking agent, the Mirkin lab's ability to DNA functionalize a polymer that water solubilized QDs while preserving their surfaces<sup>200</sup> seemed like the perfect solution. The methodology is actually quite easy and robust, so long as you have access to a rotovap and ultracentrifuge, and can accurately calculate your QD's concentration. I solved the equipment issue by borrowing them from other labs in the department. The concentration issue was not so easily solved, however, and was a persistent problem with this project. ICP-OES was employed to analyze the Te concentrations of aliquots of the CdTe/CdSe core-shell QDs. Since we know that the CdTe cores are ~3 nm in diameter,<sup>201</sup> CdTe's lattice constant<sup>209</sup> and the Te concentration in an aliquot can be used to fairly accurately calculate the core-shell's concentration. With their final size measured with TEM, the total QD surface area in an aliquot can be determined. This value is important, since the polymer wrapping procedure only works if the monomer concentration is >300 excess per nm<sup>2</sup> of the QD surface area to be covered.<sup>200</sup> Correctly calculating the QD concentration after water solubilization would also be very important to making the AuBP – QD hybrids.

The ICP-OES technique requires the thorough removal of organic compounds and the complete dissolution of NPs in water to give accurate measurements. For QDs, this is generally

achieved by sedimenting the colloid, then dissolving it in aqua regia. Unfortunately, aqua regia does not dissolve Te containing samples well, and instead forms an insoluble orange precipitate (Figure 5.2.1.3g). This precipitate is most likely a poly-telluride, and its presence means the measured Te concentration is much lower than is true. This renders all the concentration values too low, making the amount of polymer used for water solubilization too small, and ultimately resulting in only ~10% QD efficiency from synthesis to water solubility, when it should have been closer to ~90%.<sup>200</sup> This issue would also affect the calculation of the H<sub>2</sub>O – QD's concentration, unnecessarily complicating the AuBP – QD hybrid synthesis.

After a chance discussion, I tried using the semiconductor etch solution of Br<sub>2</sub> and methanol to dissolve my QDs. While the QDs completely dissolved, showing no orange residue, the methanol introduced enough organic contamination into the ICP-OES to keep it from performing the measurements. Luckily, 3 – 5  $\mu$ L of pure Br<sub>2</sub> could still dissolve the QDs, both before and after water solubilization, allowing accurate QD concentration calculations, and resulting in the expected water solubilization efficiency. As a safety note, Br<sub>2</sub> behaves more like chlorine than iodine. Thus, to prevent vapor inhalation issues, Br<sub>2</sub> should always be worked with in a fume hood, and all items used to handle it should be vented overnight.

### 5.2.3 AuBP – QD Hybrid Systems with Polymer Protected AuBPs and DNA

Per our synthetic protocol,<sup>200</sup> water solubilizing the QDs with N<sub>3</sub>-amine functionalized PMAO would enable them to be DNA functionalized. Then, mixing these DNA – QDs with polymer-protected AuBPs functionalized with the complementary DNA strands should create the structures shown in Figure 5.2.1.1. Unfortunately, we could not make this happen. Taking advantage of newly acquired instruments, we employed cryo-TEM to image the AuBP – QD structures *in-situ*.

We did this to prevent solvent evaporation complications, to ensure we had made the hybrids, and to gain insight into their solution phase structures, especially the interparticle separations of the AuBPs and QDs. Of the samples we made, only one may have had the AuBP – QD systems we sought (Figure 5.2.3.1b), and the rest either showed no hybrids, or structures that were attributable to random NP distribution (Figure 5.2.3.1a,c-f). Our inability to make these hybrids was further confirmed with bulk, solution-phase PL experiments that did not demonstrate a QD PL increase upon excitation at the AuBP LSP wavelength (Figure 5.2.3.1g,i), as compared bulk QD colloid's PL when excited at the same wavelength (Figure 5.2.3.1g,ii). Thus, we eventually suspended this line of research.

Before moving on, the persistent cryo-TEM sample preparation problem we encountered is worth mentioning (Figure 5.2.3.1d,i). Cryo-TEM grids contain wells meant to hold the sample covered in a thin water coating. The water is then converted into ice when the grid is submerged in liquid propane or ethane, freezing the sample's solution phase morphology. As explicitly shown in Figure 5.2.3.1d,i, neither our AuBPs nor our QDs enter the wells, instead selectively coating every other area of the grid. This hampers ice formation, and would've complicated the interpretation of our results, if we could've made the AuBP – QD structures.

#### *5.2.4 Liquid Cell AuBP – QD Systems for Enhanced Fluorescence Investigations*

In addition to making the water soluble QDs and trying to characterize the possible AuBP – QD systems, I was also modifying our home-built optical setup to so we could eventually perform single-structure DF and PL characterization of the hybrids. The setup was similar to the one described in Figure 5.1.3.4, except with a 790 nm continuous wave (CW) diode laser used as the excitation source. Given the extreme sensitivity of the AuBP resonance due to changes in its

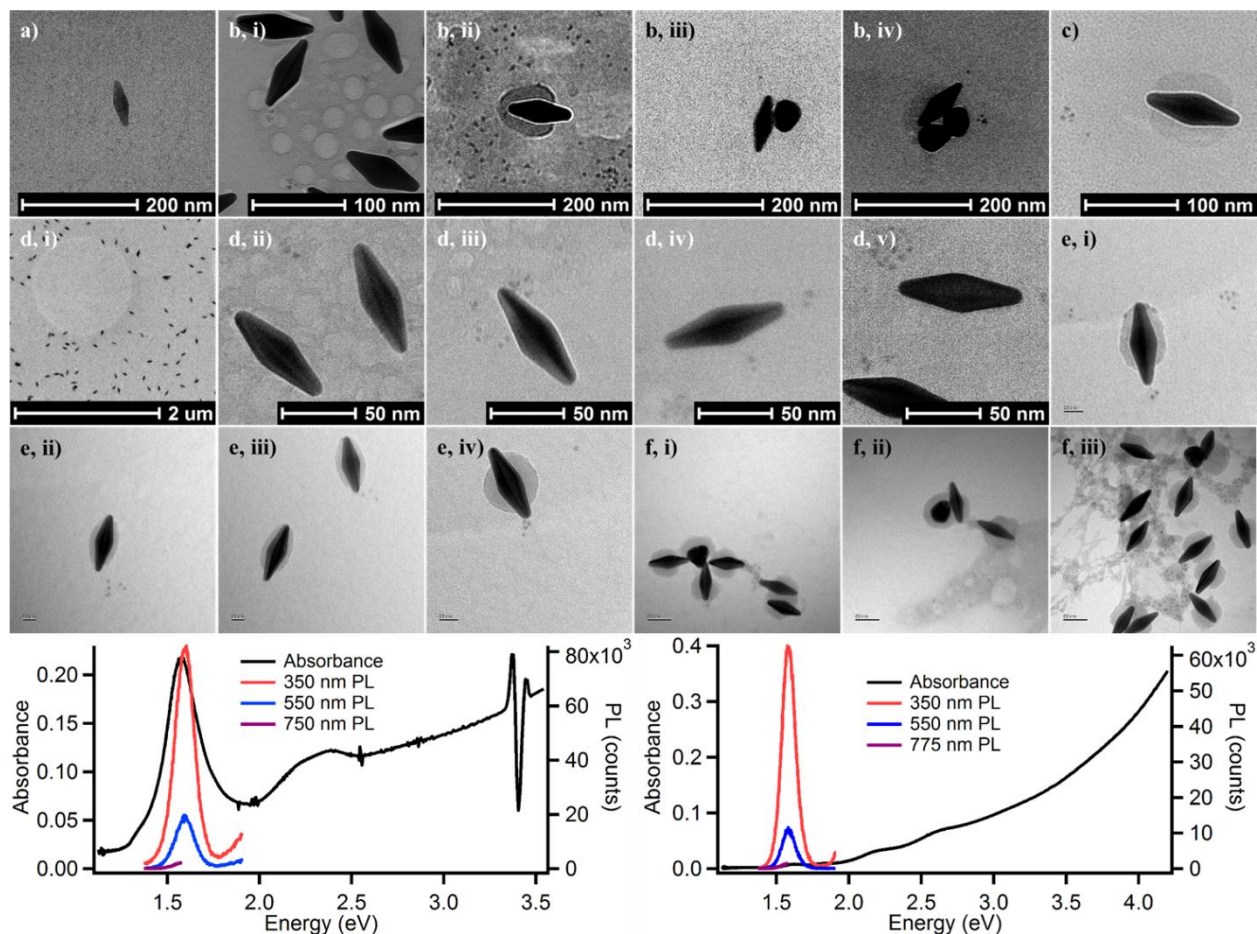


**Figure 5.2.3.1** a – f) Cryo-TEM images of several attempts to make AuBP – QD hybrid systems using polymer protected AuBPs, H<sub>2</sub>O – QDs, and DNA. g) UV/Vis and PL spectra of i) AuBP – QD hybrid system, ii) stock QD solution under different excitation wavelengths. The lack of PL intensity change when the AuBP – QD system was excited at the AuBP plasmon resonance indicated a lack of hybrid structure formation. d,i) Low magnification cryo-TEM image, demonstrating the persistent, cryo-TEM sample prep problem we encountered.

dielectric environment,<sup>50</sup> as well as previous reports in the literature,<sup>196</sup> the system was tested on thin films of AuBPs immersed in a cell of water. When it became clear that our initial attempts to make AuBP – QDs were not working, the water cell was exchanged for a cell of dilute, H<sub>2</sub>O –

QDs. The goal was to correlate the AuBP scatterer locations, as determined by white light and low-power laser excitation, with PL events induced by QDs drifting into the regions of maximum electric field enhancement around the AuBPs.<sup>196</sup> These events should turn ‘on’ and ‘off’ with time, as the QDs’ Brownian motion move them around the AuBPs.

Unfortunately, while we could correlate the AuBPs’ black-body and laser scattering locations, upon adding a long pass filter to remove the laser’s signal, we could not consistently correlate observed PL events with AuBP locations (Figure 5.2.4.1). Sometimes, no signal was observed (Figure 5.2.4.1a,iii), and in others, some events were recorded, but they either did not correlate to AuBP locations, or they did not change with time (Figure 5.2.4.1b,iii). These problems could have been caused by a wide range of issues, including the AuBPs quenching the QDs’ PL, too low of a QD concentration in the cell, the laser’s power being too low, or the introduction of the long-pass filter changing the focal distance of the setup. Without a known sample for comparison, however, determining what was wrong would be difficult.

### *5.2.5 Amide Bond Based AuBP – QD Hybrid Systems*

In a final attempt to make AuBP – QD systems in solution, I decided to employ amide bond chemistry to coat AuBPs with QDs. Given previous work,<sup>50,192,210</sup> and since amide bond reactions are well established in biochemistry,<sup>211</sup> amine functionalized AuBPs were mixed with EDC and sulfo-NHS functionalized QDs. The first attempt of this reaction seemed to yield promising results (Figure 5.2.5.1c). Unfortunately, it failed to be reproducible. Subsequent reactions characterized with both UV/Vis and cryo-TEM could not confirm AuBP – QD hybrid formation (Figure 5.2.5.1d-f). It is possible that, given the distinct temperature and pH sensitivity of these reactions,<sup>211</sup> this mechanism is still worth further investigation. It must be noted that only

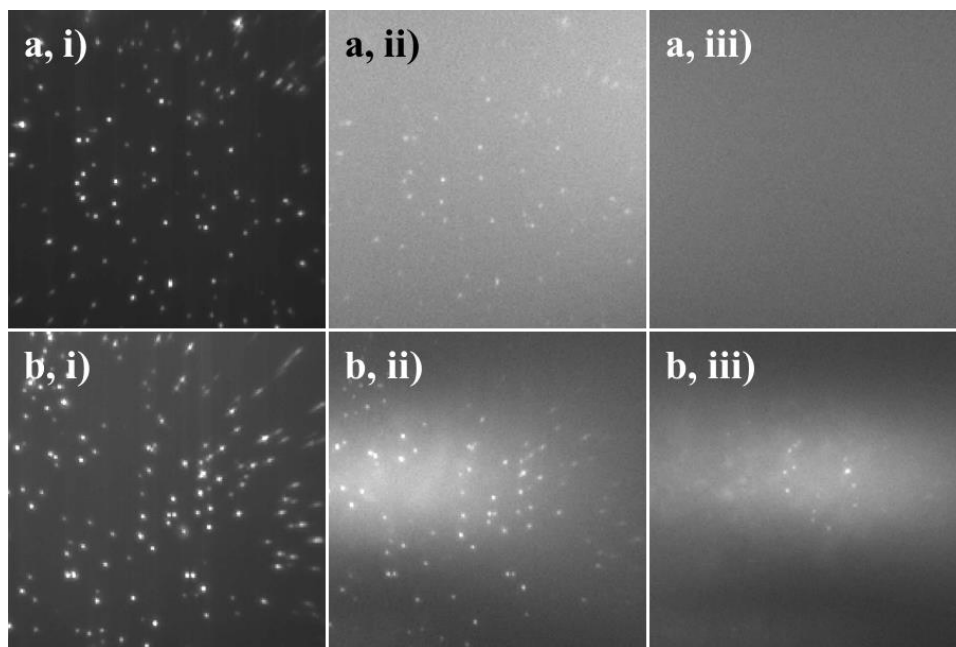


**Figure 5.2.4.1** Examples of i) DF white light scattering, ii) low power laser scattering, and iii) high power laser illumination, after the introduction of the long-pass laser filter for two different spots, a) and b), of the same BP – QD liquid cell system. b,iii) is the first frame of a movie recorded over this particular region. The spots do not change in intensity, and several do not correspond to the locations of AuBP scatterers.

polymer coated AuBPs can be used for these experiments, because CTAB, having an ammonium group and forming micelles independent of AuBPs, will interfere with amide bond formation between AuBPs and QDs.

### 5.2.6 Conclusion

Given the amount of effort exerted on this project, It is unfortunate that it did not yield the desired results. There are still many possible ways to make AuBP – QD hybrid systems, and with further refinement and investigation, the structures outlined in Figure 5.2.1.1 could be realized. The lack

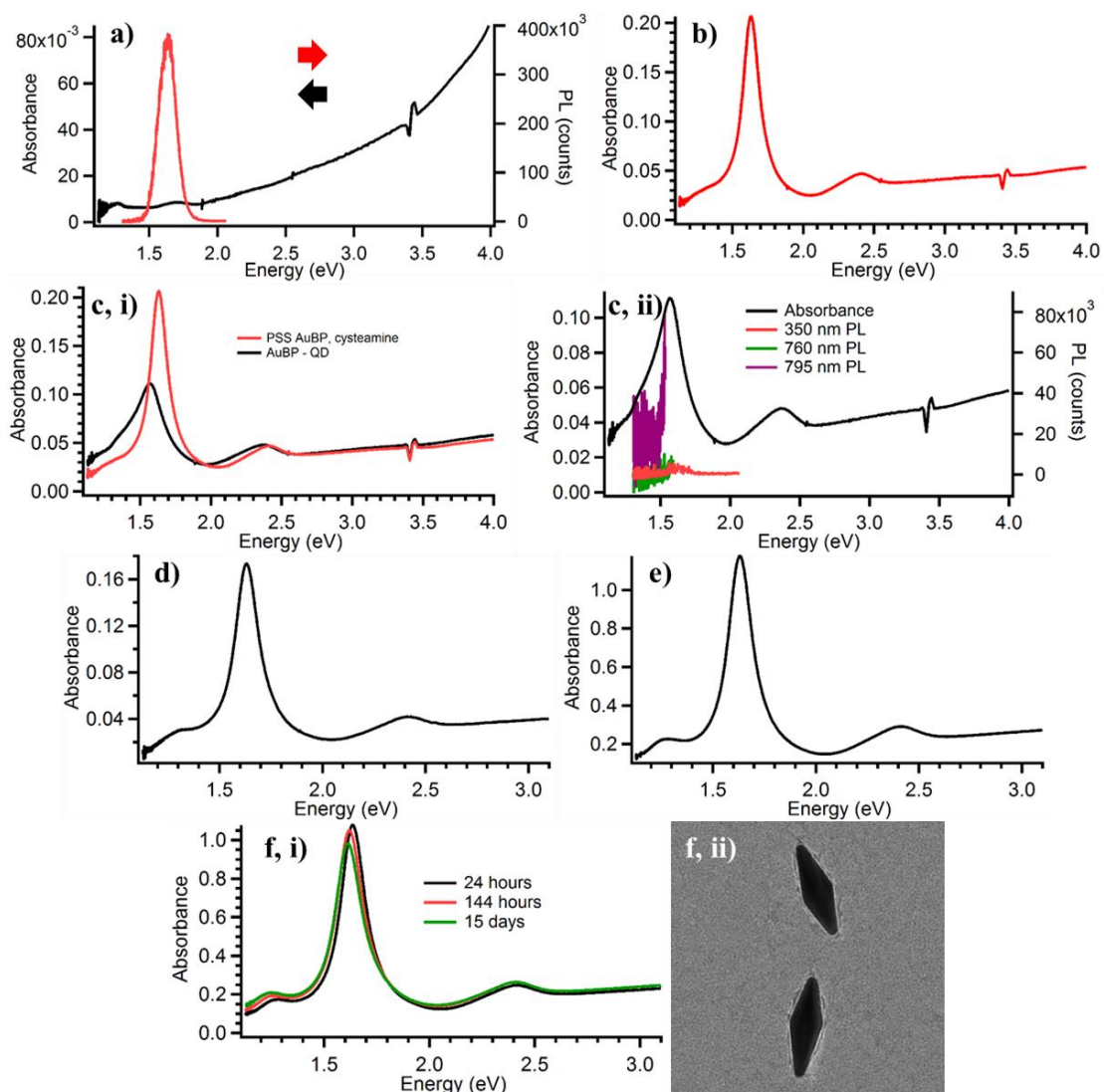


**Figure 5.2.5.1** AuBP – QD hybrid attempts using amide bond chemistry. a) UV/Vis and PL spectra of EDC/sulfo-NHS functionalized H<sub>2</sub>O – QDs. b) UV/Vis spectra of purified, PSS coated, cysteamine functionalized AuBPs. c,i) Comparison of AuBP UV/Vis spectrum in b) with the AuBP – QD system spectrum, after reacting overnight. c,ii) UV/Vis and PL spectra of the AuBP-QD hybrid structures. The PL signal of the 795 nm excitation is due to incomplete cutoff of the excitation wavelength. d), e) UV/Vis spectra of subsequent attempts to make AuBP – QD hybrids. f,i) Time resolved UV/Vis spectra of the last, amide bond AuBP – QD attempt, demonstrating minor evolution with time. f,ii) Representative cryo-TEM image of sample in f,i).

of consistent, positive results using any of these methodologies eventually encountered the barrier of time, leading to this project being suspended. However, we hope it will be revisited in the future. On a related note, given a recent publication,<sup>205</sup> the PL improvement of the type-II CdTe/CdSe QDs used in this study upon DT treatment is worth more study.

## Chapter 6. Collaborations

This chapter provides a brief commentary on the two collaborations in which I played a small but important part. The first (Chapter 6.1) resulted in my first publication and is still on-going, with another paper forthcoming. The second (Chapter 6.2) is in the submission process. I contributed to both projects as a nanoparticle expert, in terms of particle synthesis (Chapter 6.1) or characterization (Chapter 6.2). I enjoyed working on both, and look forward to their completion.

### 6.1 Viscoelastic Flows in Simple Liquids Generated by Vibrating Nanostructures<sup>33</sup>

Collaborators: Matt Pelton (first author), Debadi Chakraborty, and John E. Sader

*This paper was originally published in Physical Review Letters on December 13<sup>th</sup>, 2013, and is copyrighted by the American Physical Society. Parts of this paper are reproduced with the authors' permissions in this chapter.*

As was presented in Chapter 1, the equation of motion for a LSPR is well described by the standard formulation of a damped harmonic oscillator. This means that LSPRs dissipate energy through some mechanism. In the case of a plasmonic NP excited by a powerful enough laser, this consists of the electrons dumping energy into the NP's crystal lattice.<sup>51</sup> This results in the NP heating and expanding quickly, generating nearly coherent acoustic oscillations.<sup>33,51</sup> The study of these oscillations was hampered for a long time, due to the inherent inhomogeneity of most AuNP syntheses. These introduced inhomogeneous dephasing effects that obscured the acoustic homogeneous damping.<sup>33,51</sup> Even though the AuBP synthesis is only ~30% shape efficient, AuBPs are the most monodisperse of all colloiddally synthesized AuNPs,<sup>6,33,51</sup> and the separation in energy

between the AuBP LSP and the AuNS biproduct LSPR is large enough to allow the AuBPs' selective excitation.<sup>33,51</sup> This makes them an ideal platform for these kinds of studies. Lastly, AuBPs can be polymer coated,<sup>50</sup> completely removing free CTAB from the colloid. This allows the NPs to be resuspended in different solvents, and prevents complications due to the presence of excess surfactant ligands.<sup>33</sup>

Our lab previously studied how the acoustic vibrations changed the AuBP LSP.<sup>51</sup> This project sought to explore how the solvent environment affected the damping of these vibrations, especially in highly viscous simple liquids.<sup>33</sup> AuBPs were again used as the NP probes, and were my contribution to this project. AuBPs were synthesized as described in Chapter 2, not purified, PSS functionalized as described in Chapter 5, and resuspended in NPH<sub>2</sub>O (Figure 6.1.1a).<sup>33</sup> Prof. Pelton made the high viscosity water-glycerol mixtures and performed the experiments, with Debadi Chakraborty and Prof. Sader performing the theoretical calculations.<sup>33</sup> By monitoring the frequency shifts of the AuBP LSPs in solutions with increasing viscosity over time, we successfully investigated the viscoelastic flow regime of simple liquids for the very first time.<sup>33</sup>

Since what we observed should be generalizable for all nanoscale liquid-structure interactions,<sup>33</sup> the on-going work seeks to explore more simple liquids, as well as investigate the temperature dependence of this phenomenon. Thus, the AuBPs are being suspended in pure ethylene glycol too (Sigma Aldrich, anhydrous, 99.8%, EG) (Figure 6.1.1b). This necessitates some extra steps in the preparation process, since PSS coated AuBPs cannot be directly resuspended in pure EG from NPH<sub>2</sub>O. Trying to do this causes the colloid to turn a deep blue/purple in color, indicating that the AuBPs have aggregated. Unfortunately, this process is irreversible. Therefore, after functionalizing with PSS, AuBPs that will be transferred into EG are resuspended to 5.6 mL with NPH<sub>2</sub>O, to which 4 mL of 0.1 wt % PSS and 2.4 mL of EG are

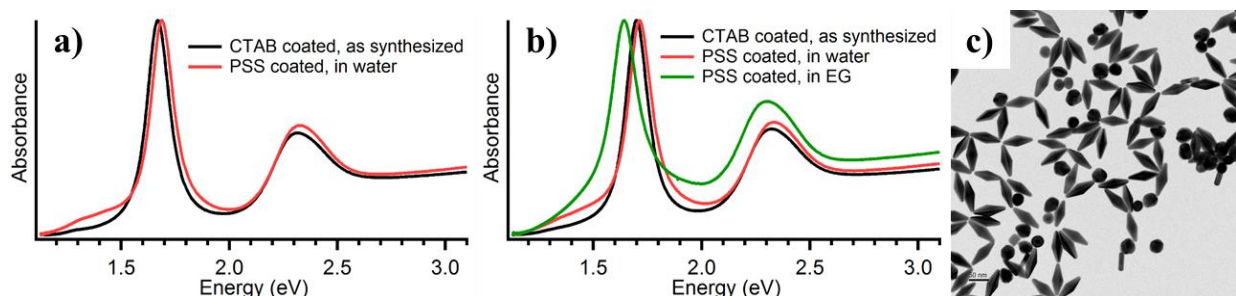


**Figure 6.1.1** a) and b) UV/Vis spectra of AuBP colloids as synthesized, PSS functionalized, and being in EG. The plasmon resonance shifts are as expected. c) Representative TEM image of the colloid in a), after PSS functionalization.

added, making a 12 mL, 20% v:v EG solution. The solution was mixed, soaked overnight (15 – 19 hours), and then centrifuged at 5500  $g$  at RT for 60 minutes. The supernatant was then decanted, and the pellet resuspended with 500  $\mu\text{L}$  – 1 mL of pure EG before characterization. As an experimental note, due to very large difference in dielectric constants between water and EG, significantly ‘blue’ AuBPs (i.e., with as-synthesized LSPs close to 700 nm) AuBPs must be used for these experiments. The group of Prof. Pelton at the University of Maryland, Baltimore County is currently studying these NPs.

## 6.2 Scalable Ligand-Mediated Transport Synthesis of Perovskite Nanocrystals with Resolved Ultrafast Intraband Relaxation and Exciton Coherences<sup>34</sup>

Collaborators: Lili Wang (first author), Nicholas E. Williams, John P. Otto, Dugan Hayes, Ryan E. Wood, and Gregory S. Engel

*This paper is currently in the submission process at ACS Nano.*

Recent interest in bulk perovskites has been driven by their impressive photovoltaic efficiencies.<sup>212</sup> As is now the case with semiconductors, demonstrations of the bulk material's utility has generated interest in QDs of that material.<sup>213-215</sup> Unfortunately, all perovskite QDs are very unstable, existing at best for only a few hours, and most did not exhibit high quantum yields (QY).<sup>216</sup>

This project corrected both of these deficiencies, creating methylammonium perovskite QDs that are stable for months, anion exchangeable between bromide (Br) and iodide (I), and have QYs approaching 97%.<sup>34</sup> My contribution to this project was to characterize these NPs, by taking TEM images and performing energy dispersive x-ray (EDX) elemental analyses (Figure 6.2.1). This turned out to be slightly difficult, due to how sensitive perovskite QDs are to polar solvents.<sup>34</sup> Thus, the colloids could not be cleaned (see Chapter 5.2) before imaging to remove excess organic ligands, causing large amounts of carbon to be swiftly deposited onto the grids.<sup>183</sup> We eventually overcame this problem by significantly diluting the QD solutions before imaging, then performing multiple depositions to increase the particle density. Besides taking some of the first TEM images of these perovskite NPs, my EDX data provided a definitive comparison of the Br:I ratio in the two hybrid QD systems Lili synthesized. This paper is currently submitted to ACS Nano.

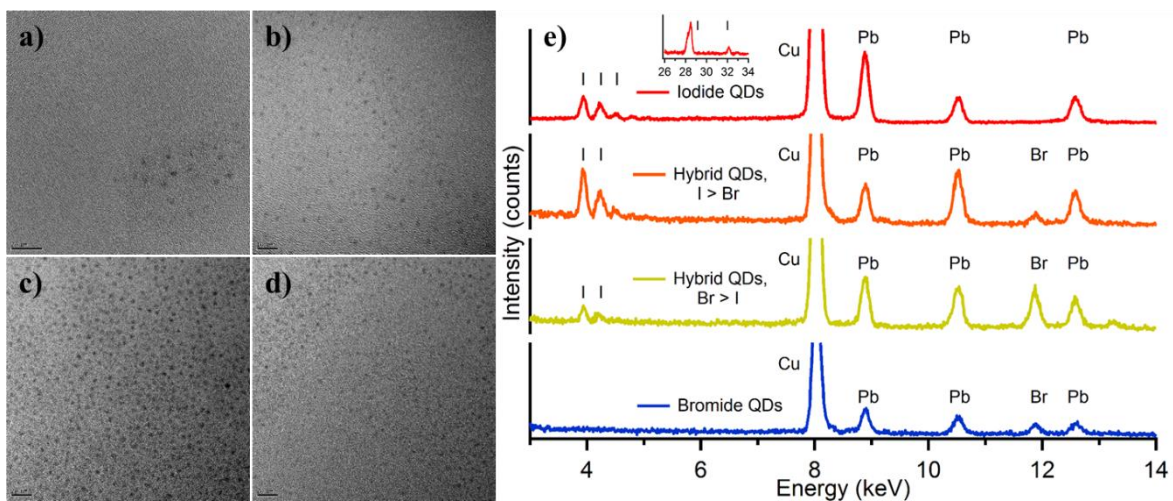


**Figure 6.2.1** Characterization of the perovskite QDs in this study. TEM images of a) Br QDs, b) hybrid QDs, with more Br than I, c) hybrid QDs, with more I than Br, d) I QDs. e) EDX data of the QDs, demonstrating the change in Br and I concentrations between the QD types. The inset shows the characteristic I peaks in the 26 – 34 keV regime.

## Chapter 7. Conclusion and Outlook

This manuscript is the summary of the vast quantity of work I've performed over the course of my PhD. While the research had a consistent theme, the theme was broad enough that it led me into fields fairly far from classic colloidal NP synthesis and characterization. From this, I gained valuable insight into advantages physics, biology, and other fields of chemistry can offer the NP community, especially as it relates to the controlled assembly of plasmonic, noble metal NPs.

In Chapter 1, I introduced the history and theory of plasmonic NPs, and discussed the motivation for my research. Although some synthesis and characterization of new noble metal NPs is still done,<sup>10</sup> to actually benefit from these NPs interesting optoelectronic properties and increase their utility requires macroscopic control of their nanoscale assembly.<sup>20,22</sup> In Chapters 2 and 5.2, I presented projects that sought to controllably assemble AuBPs in solution, creating novel structures with enhanced optical properties. The dimerization of AuBPs was not only their first ever realization,<sup>20</sup> the methodology it used was easily transferable to any anisotropic AuNP system. This project elucidated the factors that needed to be controlled when solution-phase assembling AuBPs, helping me rationally design experiments to make AuBP – QD structures.

A great many routes still exist to make these hybrids, and with further study, the original concept in Figure 5.2.1.1 is an achievable reality.

In Chapters 3 and 5.1, I presented work on the controlled assembly of AuNRs and AuBPs on polymer substrates. By precisely controlling the placement of these anisotropic particles, we harnessed their electromagnetic field enhancements,<sup>15</sup> and studied their SERS<sup>22</sup> and SHG properties. The methodologies used in both projects let us make macroscopic arrays of our particles, and can be readily extended to other types of NPs and geometries. My attempt to scale

up the work of Chapter 3 is presented in Chapter 4, with an explanation of how I stumbled into studying diblock copolymer thin films. Upon discovering new surface morphologies, I investigated how and why they occurred, ultimately developing a deeper understanding of copolymer film swelling, and how to align colloidal AuNPs with such substrates. Creating useful films of noble metal NPs is harder than making films of QDs due to the very different mechanisms that make each particle type interesting. These three projects demonstrate the rich polymer chemistries available that can be exploited to assemble plasmonic NPs on substrates, offering new ways with which to apply noble metal NPs.

The collaborations of Chapter 6 did not fit the theme my thesis. However, they utilized some of the knowledge I gained while working on the rest of my projects, and serve to further emphasize the multidisciplinary nature of colloidal nanomaterials research. In Chapter 6.1, AuBPs I synthesized were, and are being, used to investigate the mechanical properties of their environments.<sup>33</sup> In Chapter 6.2, my knowledge of NP characterization helped the Engel lab study their incredibly stable and bright perovskite NPs.<sup>34</sup> In the first case, my AuBPs were used to probe the viscoelastic, non-Newtonian fluid dynamic regime in simple liquids, and in the second, my expertise enabled some of the first images these NPs to be made, as well as directly demonstrating changes in their compositions.

Although the title of my thesis is *The Solution and Substrate Assembly of Noble Metal Nanoparticles*, it might be more correct to if it were *The Interactions of Noble Metal Nanoparticle Ligands with Substrates and Other Particles* instead. With the maturation of the colloidal nanomaterials field, scientists from other disciplines have been attracted to it. This includes chemists with backgrounds classically described as ‘inorganic’ or ‘organic,’ and they bring with them knowledge of techniques and reactions that have not been previously applied to colloidal

NPs. While this knowledge may need modifications before being directly applied to NPs,<sup>217,218</sup> they can provide colloidal NP researchers with new opportunities to learn about our systems, especially with respect to NP surface chemistries.<sup>219</sup>

A better understanding of the ligands coating colloidal, noble metal NPs could be a broad direction of future research for this project. It would allow us to better manipulate the NPs, thereby improving their assembly and integration into different systems, and could even open up new applications. More immediately, many possible projects could follow directly from the work presented in this thesis. The most obvious is to continue to work to make the AuBP – QD hybrid systems (Chapter 5.2). There are many other possible methods to create such structures, and future refinements on the techniques presented here could still yield the ideal system. Another potential project would extend the end-to-end alignment of AuNRs in Chapter 3 to AuBPs. Building from unpublished work in our lab, as well as recent advances in the literature,<sup>220,221</sup> silver coated AuBPs of different lengths could be deposited on the PS-*b*-PMMA substrates, followed by the selective removal of silver,<sup>222</sup> leaving behind regularly spaced AuBPs. Similarly, our collaboration with the Nealey lab (Chapter 5.1) could be expanded to investigate structures involving other noble metal NP types, yielding a huge diversity of with controlled interparticle separations, orientations, and type and number of NPs. With this, we would challenge the lithographic monopoly lithography on such structures, and produce them at a new size regime. Cryo-TEM studies of the AuBP dimerization process in Chapter 2 could also be performed. This would remove structural artifacts that occur due to solvent drying on a substrate, and allow us to more easily study how the assembly process evolves with time.

A great many other possible avenues of research exist as well. DNA origami could be used to control the placement of AuBPs on surfaces, as well as to create hybrid structures with tunable

distances involving fluorophores.<sup>223</sup> Research based on noble metal NPs with plasmon resonances in the near-IR<sup>10</sup> could yield colloidal NPs that we could use to enhance the absorption efficiencies in some of our infrared detectors. Alternatively, pushing the syntheses of anisotropic NPs could yield structures ideal for telecommunication applications. Likewise, the AuBP seed synthesis could be systematically investigated to improve the AuBPs' shape yield. One such report should exist, but hasn't been published as of the writing of this thesis. While post-synthetic purification of the AuBP colloids<sup>9</sup> has increased their utility, the quirks of the various procedures make them difficult to duplicate. Controlling the AuBP seed synthesis would improve the AuBP shape yield, dramatically increasing their efficacy.

My work on plasmonic NP assembly has barely touched the possibilities that exist for these particles. Further tailoring of these NPs the surface chemistries could yield structures with fascinating optical and electronic properties, as well as allowing their integration into devices. Directing the solution or substrate self-assembly of noble metal NPs will continue to be a fruitful area of research, as the implications of these NPs' properties find interest in other fields and potential applications.

## References

- (1) Wagner, F. E.; Haslbeck, S.; Stievano, L.; Calogero, S.; Pankhurst, Q. a; Martinek, K. P. Before Striking Gold in Gold-Ruby Glass. *Nature* **2000**, *407* (6805), 691–692.
- (2) Tweney, R. D. Discovering Discovery: How Faraday Found the First Metallic Colloid. *Perspect. Sci.* **2006**, *14* (1), 97–121.
- (3) Jana, N. R.; Gearheart, L.; Murphy, C. J. Wet Chemical Synthesis of High Aspect Ratio Cylindrical Gold Nanorods. *J. Phys. Chem. B* **2001**, *105* (19), 4065–4067.
- (4) Suh, K. Y.; Kim, Y. S.; Lee, H. H.; Jana, N. R.; Gearheart, L.; Murphy, C. J. Seed-Mediated Growth Approach for Shape-Controlled Synthesis of Spheroidal and Rod-like Gold Nanoparticles Using a Surfactant Template. *Adv. Mater.* **2001**, *13* (18), 1389–1393.
- (5) Nikoobakht, B.; El-Sayed, M. A. Preparation and Growth Mechanism of Gold Nanorods (NRs) Using Seed-Mediated Growth Method. *Chem. Mater.* **2003**, *15* (10), 1957–1962.
- (6) Liu, M.; Guyot-Sionnest, P. Mechanism of Silver(I)-Assisted Growth of Gold Nanorods and Bipyramids. *J. Phys. Chem. B* **2005**, *109*, 22192–22200.
- (7) Weiner, R. G.; DeSantis, C. J.; Cardoso, M. B. T.; Skrabalak, S. E. Diffusion and Seed Shape: Intertwined Parameters in the Synthesis of Branched Metal Nanostructures. *ACS Nano* **2014**, *8* (8), 8625–8635.
- (8) Chandra, K.; Culver, K. S. B.; Werner, S. E.; Lee, R. C.; Odom, T. W. Manipulating the Anisotropic Structure of Gold Nanostars Using Good's Buffers. *Chem. Mater.* **2016**, *28* (18), 6763–6769.
- (9) Lee, J.-H.; Gibson, K. J.; Chen, G.; Weizmann, Y. Bipyramid-Templated Synthesis of Monodisperse Anisotropic Gold Nanocrystals. *Nat. Commun.* **2015**, *6* (May), 7571.
- (10) Mayer, M.; Scarabelli, L.; March, K.; Altantzis, T.; Tebbe, M.; Kociak, M.; Bals, S.; de Abajo, F. J. G.; Fery, A.; Liz-Marzán, L. M. Controlled Living Nanowire Growth: Precise Control over the Morphology and Optical Properties of AgAuAg Bimetallic Nanowires. *Nano Lett.* **2015**, *15* (8), 5427–5437.
- (11) Li, N.; Zhao, P.; Astruc, D. Anisotropic Gold Nanoparticles: Synthesis, Properties, Applications, and Toxicity. *Angew. Chemie Int. Ed.* **2014**, *53* (7), 1756–1789.
- (12) Liu; Guyot-Sionnest, P. Synthesis and Optical Characterization of Au/Ag Core/Shell Nanorods. *J. Phys. Chem. B* **2004**, *108* (19), 5882–5888.
- (13) Hu, J.-W.; Li, J.-F.; Ren, B.; Wu, D.-Y.; Sun, S.-G.; Tian, Z.-Q. Palladium-Coated Gold Nanoparticles with a Controlled Shell Thickness Used as Surface-Enhanced Raman Scattering Substrate. *J. Phys. Chem. C* **2007**, *111* (3), 1105–1112.
- (14) Ye, X.; Jin, L.; Caglayan, H.; Chen, J.; Xing, G.; Zheng, C.; Doan-Nguyen, V.; Kang, Y.; Engheta, N.; Kagan, C. R.; Murray, C. B. Improved Size-Tunable Synthesis of Monodisperse Gold Nanorods through the Use of Aromatic Additives. *ACS Nano* **2012**, *6* (3), 2804–2817.
- (15) Liu, M.; Guyot-Sionnest, P.; Lee, T. W.; Gray, S. K. Optical Properties of Rodlike and

- Bipyramidal Gold Nanoparticles from Three-Dimensional Computations. *Phys. Rev. B - Condens. Matter Mater. Phys.* **2007**, *76* (23), 1–10.
- (16) Dreaden, E. C.; Alkilany, A. M.; Huang, X.; Murphy, C. J.; El-Sayed, M. A. The Golden Age: Gold Nanoparticles for Biomedicine. *Chem. Soc. Rev.* **2012**, *Advance*.
  - (17) Huang, X.; Neretina, S.; El-Sayed, M. A. Gold Nanorods: From Synthesis and Properties to Biological and Biomedical Applications. *Adv. Mater.* **2009**, *21* (48), 4880–4910.
  - (18) Qian, X.-M.; Nie, S. M. Single-Molecule and Single-Nanoparticle SERS: From Fundamental Mechanisms to Biomedical Applications. *Chem. Soc. Rev.* **2008**, *37* (5), 912–920.
  - (19) Glotzer, S. C.; Solomon, M. J. Anisotropy of Building Blocks and Their Assembly into Complex Structures. *Nat. Mater.* **2007**, *6* (7), 557–562.
  - (20) Malachosky, E. W.; Guyot-Sionnest, P. Gold Bipyramid Nanoparticle Dimers. *J. Phys. Chem. C* **2014**, *118* (12), 6405–6412.
  - (21) Liu, Q.; Cui, Y.; Gardner, D.; Li, X.; He, S.; Smalyukh, I. I. Self-Alignment of Plasmonic Gold Nanorods in Reconfigurable Anisotropic Fluids for Tunable Bulk Metamaterial Applications. *Nano Lett.* **2010**, *10* (4), 1347–1353.
  - (22) Tong, Q.; Malachosky, E. W.; Raybin, J.; Guyot-Sionnest, P.; Sibener, S. J. End-to-End Alignment of Gold Nanorods on Topographically Enhanced, Cylinder Forming Diblock Copolymer Templates and Their Surface Enhanced Raman Scattering Properties. *J. Phys. Chem. C* **2014**, *118* (33), 19259–19265.
  - (23) Peng, B.; Li, G.; Li, D.; Dodson, S.; Zhang, Q.; Zhang, J.; Lee, Y. H.; Demir, H. V.; Yi Ling, X.; Xiong, Q. Vertically Aligned Gold Nanorod Monolayer on Arbitrary Substrates: Self-Assembly and Femtomolar Detection of Food Contaminants. *ACS Nano* **2013**, *7* (7), 5993–6000.
  - (24) Slaughter, L. S.; Wu, Y.; Willingham, B. A.; Nordlander, P.; Link, S. Effects of Symmetry Breaking and Conductive Contact on the Plasmon Couplings in Gold Nanorod Dimers. *ACS Nano* **2010**, *8*, 4657–4666.
  - (25) Shao, L.; Woo, K. C.; Chen, H.; Jin, Z.; Wang, J.; Lin, H.-Q. Angle- and Energy-Resolved Plasmon Couplings in Gold Nanorod Dimers. *ACS Nano* **2010**, *3053*, 3062.
  - (26) Sivun, D.; Vidal, C.; Munkhbat, B.; Arnold, N.; Klar, T. A.; Hrelescu, C. Anticorrelation of Photoluminescence from Gold Nanoparticle Dimers with Hot-Spot Intensity. *Nano Lett.* **2016**.
  - (27) Ross, M. B.; Ku, J. C.; Vaccarezza, V. M.; Schatz, G. C.; Mirkin, C. A. Nanoscale Form Dictates Mesoscale Function in Plasmonic DNA–nanoparticle Superlattices. *Nat Nano* **2015**, *10* (5), 453–458.
  - (28) Jain K., P.; Huang, W.; El-Sayed, M. A. On the Universal Scaling Behavior of the Distance Decay of Plasmon Coupling in Metal Nanoparticle Pairs: A Plasmon Ruler Equation. *Nano Lett.* **2007**, *7*, 2080–2088.

- (29) Wang, Y.; Deprince III, A. E.; Gray, S. K.; Lin, X.-M.; Pelton, M. Solvent-Mediated End-to-End Assembly of Gold Nanorods. *J. Phys. Chem. Lett.* **2010**, *1*, 2692–2698.
- (30) Burrows, N. D.; Vartanian, A. M.; Abadeer, N. S.; Grzincic, E. M.; Jacob, L. M.; Lin, W.; Li, J.; Dennison, J. M.; Hinman, J. G.; Murphy, C. J. Anisotropic Nanoparticles and Anisotropic Surface Chemistry. *J. Phys. Chem. Lett.* **2016**, *7* (4), 632–641.
- (31) McQuarrie, D. A. *Quantum Chemistry*, Second.; University Science Books: Sausalito, California, 2008.
- (32) Giannini, V.; Fernández-Domínguez, A. I.; Heck, S. C.; Maier, S. A. Plasmonic Nanoantennas: Fundamentals and Their Use in Controlling the Radiative Properties of Nanoemitters. *Chem. Rev.* **2011**, *111* (6), 3888–3912.
- (33) Pelton, M.; Chakraborty, D.; Malachosky, E.; Guyot-Sionnest, P.; Sader, J. E. Viscoelastic Flows in Simple Liquids Generated by Vibrating Nanostructures. *Phys. Rev. Lett.* **2013**, *111* (24), 244502.
- (34) Wang, L.; Williams, N. E.; Malachosky, E. W.; Otto, J. P.; Hayes, D.; Wood, R. E.; Guyot-Sionnest, P.; Engel, G. S. Scalable Ligand-Mediated Transport Synthesis of Perovskite Nanocrystals with Resolved Ultrafast Intraband Relaxation and Exciton Coherences.
- (35) Maier, S. A. *Plasmonics: Fundamentals and Applications*; Springer US: Boston, MA, 2007.
- (36) El-Sayed, M.; Link, S. Optical Spectroscopy of Surface Plasmons in Metal Nanoparticles. In *Semiconductor and Metal Nanocrystals*; Optical Science and Engineering; CRC Press, 2003.
- (37) Mie, G. Contributions on the Optics of Turbid Media, Particularly Colloidal Metal Solutions. *Ann. Phys.* **1908**, *25*, 377–445.
- (38) Gans, R. Über Die Form Ultramikroskopischer Goldteilchen. *R. Ann. Phys.* **1912**, *342*, 881.
- (39) Eustis, S.; El-Sayed, M. A. Why Gold Nanoparticles Are More Precious than Pretty Gold: Noble Metal Surface Plasmon Resonance and Its Enhancement of the Radiative and Nonradiative Properties of Nanocrystals of Different Shapes. *Chem. Soc. Rev.* **2006**, *35* (3), 209–217.
- (40) Kühn, S.; Håkanson, U.; Rogobete, L.; Sandoghdar, V. Enhancement of Single-Molecule Fluorescence Using a Gold Nanoparticle as an Optical Nanoantenna. *Phys. Rev. Lett.* **2006**, *97* (1), 1–4.
- (41) Damm, C.; Segets, D.; Yang, G.; Vieweg, B. F.; Spiecker, E.; Peukert, W. Shape Transformation Mechanism of Silver Nanorods in Aqueous Solution. *Small* **2011**, *7* (1), 147–156.
- (42) Zhu, H.; Zhang, C.; Yin, Y. Novel Synthesis of Copper Nanoparticles: Influence of the Synthesis Conditions on the Particle Size. *Nanotechnology* **2005**, *16* (12), 3079.
- (43) Prunier, H.; Ricolleau, C.; Nelayah, J.; Wang, G.; Alloyeau, D. Original Anisotropic Growth Mode of Copper Nanorods by Vapor Phase Deposition. *Cryst. Growth Des.* **2014**, *14* (12), 6350–6356.

- (44) Jakab, A.; Rosman, C.; Khalavka, Y.; Becker, J.; Trügler, A.; Hohenester, U.; Sönnichsen, C. Highly Sensitive Plasmonic Silver Nanorods. *ACS Nano* **2011**, *5* (9), 6880–6885.
- (45) Jana, N. R.; Gearheart, L.; Murphy, C. J. Wet Chemical Synthesis of Silver Nanorods and Nanowires of Controllable Aspect Ratio. *Chem. Commun.* **2001**, No. 7, 617–618.
- (46) Mott, D.; Galkowski, J.; Wang, L.; Luo, J.; Zhong, C. J. Synthesis of Size-Controlled and Shaped Copper Nanoparticles. *Langmuir* **2007**, *23* (10), 5740–5745.
- (47) Luo, M.; Ruditskiy, A.; Peng, H.-C.; Tao, J.; Figueroa-Cosme, L.; He, Z.; Xia, Y. Penta-Twinned Copper Nanorods: Facile Synthesis via Seed-Mediated Growth and Their Tunable Plasmonic Properties. *Adv. Funct. Mater.* **2016**, *26* (8), 1209–1216.
- (48) Liu, M.; Lee, T.-W.; Gray, K. S.; Guyot-Sionnest, P.; Pelton, M. Excitation of Dark Plasmon in Metal Nanoparticles by a Localized Emitter. *PRL* **2009**, *102*, 107401–107404.
- (49) Liu, M.; Pelton, M.; Guyot-Sionnest, P. Reduced Damping of Surface Plasmons at Low Temperatures. *Phys. Rev. B* **2009**, *79*, 35415–35418.
- (50) Burgin, J.; Liu, M.; Guyot-Sionnest, P. Dielectric Sensing with Deposited Gold Bipyramids. *J. Phys. Chem. C* **2008**, *112* (49), 19279–19282.
- (51) Pelton, M.; Sader, J. E.; Burgin, J.; Liu, M.; Guyot-Sionnest, P.; Gosztola, D. Damping of Acoustic Vibrations in Gold Nanoparticles. *Nat. Nanotechnol.* **2009**, *4*, 492–495.
- (52) Toussaint, K. C.; Liu, M.; Pelton, M.; Pesic, J.; Guffey, M. J.; Guyot-Sionnest, P.; Scherer, N. F. Plasmon Resonance-Based Optical Trapping of Single and Multiple Au Nanoparticles. *Opt. Express* **2007**, *15* (19), 12017–12029.
- (53) Chen, H.; Shao, L.; Li, Q.; Wang, J. Gold Nanorods and Their Plasmonic Properties. *Chem. Soc. Rev.* **2013**, *42* (7), 2679–2724.
- (54) Gou, L.; Murphy, C. J. Fine-Tuning the Shape of Gold Nanorods. *Chem. Mater.* **2005**, *17* (14), 3668–3672.
- (55) Johnson, C. J.; Dujardin, E.; Davis, S. A.; Murphy, C. J.; Mann, S. Growth and Form of Gold Nanorods Prepared by Seed-Mediated, Surfactant-Directed Synthesis. *J. Mater. Chem.* **2002**, *12*, 1765–1770.
- (56) Smith, D. K.; Miller, N. R.; Korgel, B. A. Iodide in CTAB Prevents Gold Nanorod Formation. *Langmuir* **2009**, *25* (16), 9518–9524.
- (57) Ye, X.; Gao, Y.; Chen, J.; Reifsnnyder, D. C.; Zheng, C.; Murray, C. B. Seeded Growth of Monodisperse Gold Nanorods Using Bromide-Free Surfactant Mixtures. *Nano Lett.* **2013**, *13* (5), 2163–2171.
- (58) Kou, X.; Zhang, S.; Tsung, C.-K.; Yeung, M. H.; Shi, Q.; Stucky, G. D.; Sun, L.; Wang, J.; Yan, C. Growth of Gold Nanorods and Bipyramids Using CTEAB Surfactant. *J. Phys. Chem. B* **2006**, *110* (33), 16377–16383.
- (59) Orendorff, C. J.; Hankins, P. L.; Murphy, C. J. pH-Triggered Assembly of Gold Nanorods. *Langmuir* **2005**, *21*, 2022–2026.

- (60) Kawamura, G.; Yang, Y.; Nogami, M. End-to-End Assembly of CTAB-Stabilized Gold Nanorods by Citrate Anions. *J. Phys. Chem. C* **2008**, *112*, 10632–10636.
- (61) Joseph, S. T. S.; Ipe, B. I.; Pramod, P.; Thomas, K. G. Gold Nanorods to Nanochains: Mechanistic Investigations on Their Longitudinal Assembly Using  $\omega$ -Alkanedithiols and Interplasmon Coupling. *J. Phys. Chem. B* **2006**, *110*, 150–157.
- (62) Zhu, Z.; Liu, W.; Li, Z.; Han, B.; Zhou, Y.; Gao, Y.; Tang, Z. Manipulation of Collective Optical Activity in One-Dimensional Plasmonic Assembly. *ACS Nano* **2012**, *6*, 2326–2335.
- (63) Thomas, K. G.; Barazzouk, S.; Ipe, B. I.; Joseph, S. T. S.; Kamat, P. V. Uniaxial Plasmon Coupling through Longitudinal Self-Assembly of Gold Nanorods. *J. Phys. Chem. B* **2004**, *108*, 13066–13068.
- (64) Zhang, S. S.; Kou, X.; Yang, Z.; Shi, Q.; Stucky, G. D.; Sun, L.; Wang, J.; Yan, C. Nanonecklaces Assembled from Gold Rods, Spheres, and Bipyramids. *Chem. Commun.* **2007**, No. 18, 1816–1818.
- (65) Sethi, M.; Joung, G.; Knecht, M. R. Linear Assembly of Au Nanorods Using Biomimetic Ligands. *Langmuir* **2009**, *25*, 1572–1581.
- (66) Selvakannan, P. R.; Dumas, E.; Dumur, F.; Pechoux, C.; Beaunier, P.; Etcheberry, A.; Secheresse, F.; Remita, H.; Mayer, C. R. Coordination Chemistry Approach for the End-to-End Assembly of Gold Nanorods. *J. Colloid Interface Sci.* **2010**, *349*, 93–97.
- (67) Fava, D.; Nie, Z.; Winnik, M. A.; Kumacheva, E. Evolution of Self-Assembled Structures of Polymer-Terminated Gold Nanorods in Selective Solvents. *Adv. Mater.* **2008**, *20*, 4318–4322.
- (68) Correa-Duarte, M. A.; Perez-Juste, J.; Sanchez-Iglesias, A.; Giersig, M.; Liz-Marzan, L. M. Aligning Au Nanorods by Using Carbon Nanotubes as Templates. *Angew. Chem. Int. Ed.* **2005**, *44*, 4375–4378.
- (69) Park, H.-S.; Agarwal, A.; Kotov, N. A.; Lavrentovich, O. D. Controllable Side-by-Side and End-to-End Assembly of Au Nanorods by Lyotropic Chromic Materials. *Langmuir* **2008**, *24*, 13833–13837.
- (70) Pramod, P.; Thomas, K. G. Plasmon Coupling in Dimers of Au Nanorods. *Adv. Mater.* **2008**, *20*, 4300–4305.
- (71) Nie, Z.; Fava, D.; Kumacheva, E.; Zou, S.; Walker, G. C.; Rubinstein, M. Self-Assembly of Metal-Polymer Analogues of Amphiphilic Triblock Copolymers. *Nat. Mater.* **2007**, *6*, 609–614.
- (72) Caswell, K. K.; Wilson, J. N.; Bunz, U. H. F.; Murphy, C. J. Preferential End-to-End Assembly of Gold Nanorods by Biotin–Streptavidin Connectors. *J. Am. Chem. Soc.* **2003**, *125* (46), 13914–13915.
- (73) Sethi, M.; Joung, G.; Knecht, M. R. Stability and Electrostatic Assembly of Au Nanorods for Use in Biological Assays. *Langmuir* **2009**, *25* (1), 317–325.
- (74) Funston, A. M.; Novo, C.; Davis, T. J.; Mulvaney, P. Plasmon Coupling of Gold Nanorods

- at Short Distances and in Different Geometries. *Nano Lett.* **2009**, *9*, 1651–1658.
- (75) Tan, L. H.; Xing, S.; Chen, T.; Chen, G.; Huang, X.; Zhang, H.; Chen, H. Fabrication of Polymer Nanocavities with Tailored Openings. *ACS Nano* **2009**, *3* (11), 3469–3474.
- (76) Thorkelsson, K.; Nelson, J. H.; Alivisatos, A. P.; Xu, T. End-to-End Alignment of Nanorods in Thin Films. *Nano Lett.* **2013**, *13* (10), 4908–4913.
- (77) Nikoobakht, B.; Wang, Z. L.; El-Sayed, M. A. Self-Assembly of Gold Nanorods. *J. Phys. Chem. B* **2000**, *104* (36), 8635–8640.
- (78) Sudeep, P. K.; Joseph, S. T. S.; Thomas, K. G. Selective Detection of Cysteine and Glutathione Using Gold Nanorods. *J. Am. Chem. Soc.* **2005**, *127*, 6516–6517.
- (79) Kou, X.; Ni, W.; Tsung, C.-K.; Chan, K.; Lin, H.-Q.; Stucky, G. D.; Wang, J. Growth of Gold Bipyramids with Improved Yield and Their Curvature-Directed Oxidation. *Small* **2007**, *3* (12), 2103–2113.
- (80) Yoo, H.; Jang, M. H. Size-Controlled Synthesis of Gold Bipyramids Using an Aqueous Mixture of CTAC and Salicylate Anions as the Soft Template. *Nanoscale* **2013**, *5* (15), 6708–6712.
- (81) Merrill, N. A.; Sethi, M.; Knecht, M. R. Structural and Equilibrium Effects of the Surface Passivant on the Stability of Au Nanorods. *ACS Appl. Mater. Interfaces* **2013**, *5* (16), 7906–7914.
- (82) Lin, Z.; Cai, J. J.; Scriven, L. E.; Davis, H. T. Spherical-to-Wormlike Micelle Transition in CTAB Solutions. *J. Phys. Chem.* **1994**, *98* (23), 5984–5993.
- (83) Hassan, P. A.; Yakhmi, J. V. Growth of Cationic Micelles in the Presence of Organic Additives. *Langmuir* **2000**, *16* (18), 7187–7191.
- (84) Aswal, V. K.; Goyal, P. S.; Thiagarajan, P. Small-Angle Neutron-Scattering and Viscosity Studies of CTAB/NaSal Viscoelastic Micellar Solutions. *J. Phys. Chem. B* **1998**, *102* (14), 2469–2473.
- (85) Lassiter, J. B.; Azipurua, J.; Hernandez, L. I.; Brandt, D. W.; Romero, I.; Lal, S.; Hafner, J. H.; Nordlander, P.; Halas, N. J. Close Encounters between Two Nanoshells. *Nano Lett.* **2008**, *8*, 1212–1218.
- (86) Prodan, E.; Radloff, C.; Halas, N. J.; Nordlander, P. A Hybridization Model for the Plasmon Response of Complex Nanostructures. *Science (80-. )*. **2003**, *302*, 419–422.
- (87) Willingham, B.; Brandl, D. W.; Nordlander, P. Plasmon Hybridization in Nanorod Dimers. *Appl. Phys. B* **2008**, *93*, 209–216.
- (88) Prodan, E.; Nordlander, P. Plasmon Hybridization in Spherical Nanoparticles. *J. Chem. Phys.* **2004**, *120*, 5444–5454.
- (89) Tabor, C.; Haute, D. Van; El-Sayed, M. A. Effect of Orientation on Plasmonic Coupling between Gold Nanorods. *ACS Nano* **2009**, *3*, 3670–3678.
- (90) Nordlander, P.; Oubre, C.; Prodan, E.; Li, K.; Stockman, M. I. Plasmon Hybridization in

- Nanoparticle Dimers. *Nano Lett.* **2004**, *4* (5), 899–903.
- (91) Jain, P. K.; El-Sayed, M. A. Surface Plasmon Coupling and Its Universal Size Scaling in Metal Nanostructures of Complex Geometry: Elongated Particle Pairs and Nanosphere Trimers. *J. Phys. Chem. C* **2008**, *112* (13), 4954–4960.
- (92) Woo, K. C.; Shao, L.; Chen, H.; Liang, Y.; Wang, J.; Lin, H.-Q. Universal Scaling and Fano Resonance in the Plasmon Coupling between Gold Nanorods. *ACS Nano* **2011**, *5* (7), 5976–5986.
- (93) Atay, T.; Song, J.-H.; Nurmikko, A. V. Strongly Interacting Plasmon Nanoparticle Pairs: From Dipole–Dipole Interaction to Conductively Coupled Regime. *Nano Lett.* **2004**, *4* (9), 1627–1631.
- (94) Kim, D.-S.; Heo, J.; Ahn, S.-H.; Han, S. W.; Yun, W. S.; Kim, Z. H. Real-Space Mapping of the Strongly Coupled Plasmons of Nanoparticle Dimers. *Nano Lett.* **2009**, *9* (10), 3619–3625.
- (95) Slaughter, L. S.; Chang, W.-S.; Link, S. Characterizing Plasmons in Nanoparticles and Their Assemblies with Single Particle Spectroscopy. *J. Phys. Chem. Lett.* **2011**, *2*, 2015–2023.
- (96) Lombardi, A.; Loumagne, M.; Crut, A.; Maiolo, P.; Fatti, N. Del; Vallee, F.; Spuch-Calvar, M.; Burgin, J.; Majimel, J.; Treguer-Delapierre, M. Surface Plasmon Resonance Properties of Single Elongated Nanoobjects: Gold Nano-Bipyramids and Nanorods. *Langmuir* **2012**, *28*, 9027–9033.
- (97) Matsui, I. Nanoparticles for Electronic Device Applications: A Brief Review. *J. Chem. Eng. JAPAN* **2005**, *38* (8), 535–546.
- (98) Stebe, K. J.; Lewandowski, E.; Ghosh, M. Oriented Assembly of Metamaterials. *Sci.* **2009**, *325* (5937), 159–160.
- (99) Gass, J.; Poddar, P.; Almand, J.; Srinath, S.; Srikanth, H. Superparamagnetic Polymer Nanocomposites with Uniform Fe<sub>3</sub>O<sub>4</sub> Nanoparticle Dispersions. *Adv. Funct. Mater.* **2006**, *16* (1), 71–75.
- (100) Nie, Z.; Petukhova, A.; Kumacheva, E. Properties and Emerging Applications of Self-Assembled Structures Made from Inorganic Nanoparticles. *Nat. Nanotechnol.* **2010**, *5* (1), 15–25.
- (101) Stiles, P. L.; Dieringer, J. A.; Shah, N. C.; Van Duyne, R. P. Surface-Enhanced Raman Spectroscopy. *Annu. Rev. Anal. Chem.* **2008**, *1* (1), 601–626.
- (102) Vigdeman, L.; Khanal, B. P.; Zubarev, E. R. Functional Gold Nanorods: Synthesis, Self-Assembly, and Sensing Applications. *Adv. Mater.* **2012**, *24* (36), 4811–4841.
- (103) Grande, M.; Bianco, G. V.; Vincenti, M. A.; Stomeo, T.; de Ceglia, D.; De Vittorio, M.; Petruzzelli, V.; Scalora, M.; Bruno, G.; D’Orazio, A. Experimental Surface-Enhanced Raman Scattering Response of Two-Dimensional Finite Arrays of Gold Nanopatches. *Appl. Phys. Lett.* **2012**, *101* (11).

- (104) Chirumamilla, M.; Toma, A.; Gopalakrishnan, A.; Das, G.; Zaccaria, R. P.; Krahne, R.; Rondanina, E.; Leoncini, M.; Liberale, C.; De Angelis, F.; Di Fabrizio, E. 3D Nanostar Dimers with a Sub-10-Nm Gap for Single-/Few-Molecule Surface-Enhanced Raman Scattering. *Adv. Mater.* **2014**, *26* (15), 2353–2358.
- (105) D'Andrea, C.; Fazio, B.; Gucciardi, P. G.; Giordano, M. C.; Martella, C.; Chiappe, D.; Toma, A.; de Mongeot, F.; Tantussi, F.; Vasanthakumar, P.; Fuso, F.; Allegrini, M. SERS Enhancement and Field Confinement in Nanosensors Based on Self-Organized Gold Nanowires Produced by Ion-Beam Sputtering. *J. Phys. Chem. C* **0** (0), null.
- (106) Nepal, D.; Onses, M. S.; Park, K.; Jespersen, M.; Thode, C. J.; Nealey, P. F.; Vaia, R. A. Control over Position, Orientation, and Spacing of Arrays of Gold Nanorods Using Chemically Nanopatterned Surfaces and Tailored Particle–Particle–Surface Interactions. *ACS Nano* **2012**, *6* (6), 5693–5701.
- (107) Kuemin, C.; Nowack, L.; Bozano, L.; Spencer, N. D.; Wolf, H. Oriented Assembly of Gold Nanorods on the Single-Particle Level. *Adv. Funct. Mater.* **2012**, *22* (4), 702–708.
- (108) Adams, S. M.; Campione, S.; Caldwell, J. D.; Bezares, F. J.; Culbertson, J. C.; Capolino, F.; Ragan, R. Non-Lithographic SERS Substrates: Tailoring Surface Chemistry for Au Nanoparticle Cluster Assembly. *Small* **2012**, *8* (14), 2239–2249.
- (109) Orendorff, C. J.; Gole, A.; Sau, T. K.; Murphy, C. J. Surface-Enhanced Raman Spectroscopy of Self-Assembled Monolayers: Sandwich Architecture and Nanoparticle Shape Dependence. *Anal. Chem.* **2005**, *77* (10), 3261–3266.
- (110) Kraus, T.; Malaquin, L.; Schmid, H.; Riess, W.; Spencer, N. D.; Wolf, H. Nanoparticle Printing with Single-Particle Resolution. *Nat Nano* **2007**, *2* (9), 570–576.
- (111) Liu, Z.; Huang, H.; He, T. Large-Area 2D Gold Nanorod Arrays Assembled on Block Copolymer Templates. *Small* **2013**, *9* (4), 505–510.
- (112) Zhou, X.; Zhou, Y.; Ku, J. C.; Zhang, C.; Mirkin, C. A. Capillary Force-Driven, Large-Area Alignment of Multi-Segmented Nanowires. *ACS Nano* **2014**, *8* (2), 1511–1516.
- (113) Xiao, J.; Li, Z.; Ye, X.; Ma, Y.; Qi, L. Self-Assembly of Gold Nanorods into Vertically Aligned, Rectangular Microplates with a Supercrystalline Structure. *Nanoscale* **2014**, *6* (2), 996–1004.
- (114) Gordon, M. J.; Peyrade, D. Separation of Colloidal Nanoparticles Using Capillary Immersion Forces. *Appl. Phys. Lett.* **2006**, *89* (5).
- (115) Thai, T.; Zheng, Y.; Ng, S. H.; Mudie, S.; Altissimo, M.; Bach, U. Self-Assembly of Vertically Aligned Gold Nanorod Arrays on Patterned Substrates. *Angew. Chemie Int. Ed.* **2012**, *51* (35), 8732–8735.
- (116) Kawamura, G.; Yang, Y.; Nogami, M. Facile Assembling of Gold Nanorods with Large Aspect Ratio and Their Surface-Enhanced Raman Scattering Properties. *Appl. Phys. Lett.* **2007**, *90* (26).
- (117) Fontana, J.; Livenere, J.; Bezares, F. J.; Caldwell, J. D.; Rendell, R.; Ratna, B. R. Large Surface-Enhanced Raman Scattering from Self-Assembled Gold Nanosphere Monolayers.

*Appl. Phys. Lett.* **2013**, *102* (20).

- (118) Alvarez-Puebla, R. A.; Agarwal, A.; Manna, P.; Khanal, B. P.; Aldeanueva-Potel, P.; Carbo-Argibay, E.; Pazos-Perez, N.; Vigderman, L.; Zubarev, E. R.; Kotov, N. A.; Liz-Marzan, L. M. Gold Nanorods 3D-Supercrystals as Surface Enhanced Raman Scattering Spectroscopy Substrates for the Rapid Detection of Scrambled Prions. *Proc. Natl. Acad. Sci.* **2011**, *108* (20), 8157–8161.
- (119) Pérez-Juste, J.; Liz-Marzán, L. M.; Carnie, S.; Chan, D. Y. C.; Mulvaney, P. Electric-Field-Directed Growth of Gold Nanorods in Aqueous Surfactant Solutions. *Adv. Funct. Mater.* **2004**, *14* (6), 571–579.
- (120) Vigderman, L.; Zubarev, E. R. High-Yield Synthesis of Gold Nanorods with Longitudinal SPR Peak Greater than 1200 Nm Using Hydroquinone as a Reducing Agent. *Chem. Mater.* **2013**, *25* (8), 1450–1457.
- (121) Zhu, Y.; Kuang, H.; Xu, L.; Ma, W.; Peng, C.; Hua, Y.; Wang, L.; Xu, C. Gold Nanorod Assembly Based Approach to Toxin Detection by SERS. *J. Mater. Chem.* **2012**, *22* (6), 2387–2391.
- (122) Zhong, L.; Zhou, X.; Bao, S.; Shi, Y.; Wang, Y.; Hong, S.; Huang, Y.; Wang, X.; Xie, Z.; Zhang, Q. Rational Design and SERS Properties of Side-by-Side{,} End-to-End and End-to-Side Assemblies of Au Nanorods. *J. Mater. Chem.* **2011**, *21* (38), 14448–14455.
- (123) Sundrani, D.; Darling, S. B.; Sibener, S. J. Guiding Polymers to Perfection: Macroscopic Alignment of Nanoscale Domains. *Nano Lett.* **2004**, *4* (2), 273–276.
- (124) Ouk Kim, S.; Solak, H. H.; Stoykovich, M. P.; Ferrier, N. J.; de Pablo, J. J.; Nealey, P. F. Epitaxial Self-Assembly of Block Copolymers on Lithographically Defined Nanopatterned Substrates. *Nature* **2003**, *424* (6947), 411–414.
- (125) Sundrani, D.; Darling, S. B.; Sibener, S. J. Hierarchical Assembly and Compliance of Aligned Nanoscale Polymer Cylinders in Confinement. *Langmuir* **2004**, *20* (12), 5091–5099.
- (126) Tong, Q.; Sibener, S. J. Visualization of Individual Defect Mobility and Annihilation within Cylinder-Forming Diblock Copolymer Thin Films on Nanopatterned Substrates. *Macromolecules* **2013**, *46* (21), 8538–8544.
- (127) Kao, J.; Thorkelsson, K.; Bai, P.; Rancatore, B. J.; Xu, T. Toward Functional Nanocomposites: Taking the Best of Nanoparticles{,} Polymers{,} and Small Molecules. *Chem. Soc. Rev.* **2013**, *42* (7), 2654–2678.
- (128) Deshmukh, R. D.; Liu, Y.; Composto, R. J. Two-Dimensional Confinement of Nanorods in Block Copolymer Domains. *Nano Lett.* **2007**, *7* (12), 3662–3668.
- (129) Darling, S. B.; Yufa, N. A.; Cisse, A. L.; Bader, S. D.; Sibener, S. J. Self-Organization of FePt Nanoparticles on Photochemically Modified Diblock Copolymer Templates. *Adv. Mater.* **2005**, *17* (20), 2446–2450.
- (130) Yufa, N.; Fronk, S.; Darling, S. B.; Divan, R.; Lopes, W.; Sibener, S. J. Modifying Metal-Polymer Nanostructures Using UV Exposure. *Soft Matter* **2009**, *5* (8), 1683–1686.

- (131) Son, J. G.; Bae, W. K.; Kang, K. H.; Nealey, P. F.; Char, K.; Kang, H.; Nealey, P. F.; Char, K. Placement Control of Nanomaterial Arrays on the Surface-Reconstructed Block Copolymer Thin Films. *ACS Nano* **2009**, *3* (12), 3927–3934.
- (132) Caldwell, J. D.; Glembocki, O.; Bezares, F. J.; Bassim, N. D.; Rendell, R. W.; Feygelson, M.; Ukaegbu, M.; Kasica, R.; Shirey, L.; Hosten, C. Plasmonic Nanopillar Arrays for Large-Area, High-Enhancement Surface-Enhanced Raman Scattering Sensors. *ACS Nano* **2011**, *5* (5), 4046–4055.
- (133) Liu, Z.; Qiao, J.; Niu, Z.; Wang, Q. Natural Supramolecular Building Blocks: From Virus Coat Proteins to Viral Nanoparticles. *Chem. Soc. Rev.* **2012**, *41* (18), 6178–6194.
- (134) Chan, D. Y. C.; jr., J. D. H.; White, L. R. The Interaction of Colloidal Particles Collected at Fluid Interfaces. *J. Colloid Interface Sci.* **1981**, *79* (2), 410–418.
- (135) Kralchevsky, P. A.; Paunov, V. N.; Ivanov, I. B.; Nagayama, K. Capillary Meniscus Interaction between Colloidal Particles Attached to a Liquid—fluid Interface. *J. Colloid Interface Sci.* **1992**, *151* (1), 79–94.
- (136) Kralchevsky, P. A.; Paunov, V. N.; Denkov, N. D.; Ivanov, I. B.; Nagayama, K. Energetical and Force Approaches to the Capillary Interactions between Particles Attached to a Liquid-Fluid Interface. *J. Colloid Interface Sci.* **1993**, *155* (2), 420–437.
- (137) Kralchevsky, P. A.; Nagayama, K. Capillary Forces between Colloidal Particles. *Langmuir* **1994**, *10* (1), 23–36.
- (138) Xu, Z.-C.; Shen, C.-M.; Xiao, C.-W.; Yang, T.-Z.; Chen, S.-T.; Li, H.-L.; Gao, H.-J. Fabrication of Gold Nanorod Self-Assemblies from Rod and Sphere Mixtures via Shape Self-Selective Behavior. *Chem. Phys. Lett.* **2006**, *432* (1–3), 222–225.
- (139) Mathur, A.; Brown, A.-D.; Erlebacher, J. Self-Ordering of Colloidal Particles in Shallow Nanoscale Surface Corrugations. *Langmuir* **2006**, *22* (2), 582–589.
- (140) Meena, S. K.; Sulpizi, M. Understanding the Microscopic Origin of Gold Nanoparticle Anisotropic Growth from Molecular Dynamics Simulations. *Langmuir* **2013**, *29* (48), 14954–14961.
- (141) Cui, Y.; Björk, M. T.; Liddle, J. A.; Sönnichsen, C.; Boussert, B.; Alivisatos, A. P. Integration of Colloidal Nanocrystals into Lithographically Patterned Devices. *Nano Lett.* **2004**, *4* (6), 1093–1098.
- (142) McLellan, J. M.; Li, Z.-Y.; Siekkinen, A. R.; Xia, Y. The SERS Activity of a Supported Ag Nanocube Strongly Depends on Its Orientation Relative to Laser Polarization. *Nano Lett.* **2007**, *7* (4), 1013–1017.
- (143) Camargo, P. H. C.; Rycenga, M.; Au, L.; Xia, Y. Isolating and Probing the Hot Spot Formed between Two Silver Nanocubes. *Angew. Chemie Int. Ed.* **2009**, *48* (12), 2180–2184.
- (144) Wei, H.; Xu, H. Hot Spots in Different Metal Nanostructures for Plasmon-Enhanced Raman Spectroscopy. *Nanoscale* **2013**, *5* (22), 10794–10805.
- (145) Daniel, M.-C.; Astruc, D. Gold Nanoparticles: Assembly, Supramolecular Chemistry,

- Quantum-Size-Related Properties, and Applications toward Biology, Catalysis, and Nanotechnology. *Chem. Rev.* **2004**, *104* (1), 293–346.
- (146) Hanske, C.; Tebbe, M.; Kuttner, C.; Bieber, V.; Tsukruk, V. V.; Chanana, M.; König, T. A. F.; Fery, A.; Ko, T. A. F.; Fery, A. Strongly Coupled Plasmonic Modes on Macroscopic Areas via Template-Assisted Colloidal Self-Assembly. *Nano Lett.* **2014**, *14* (12), 6863–6871.
- (147) Tebbe, M.; Mayer, M.; Glatz, B. a.; Hanske, C.; Probst, P. T.; Mueller, M. B.; Karg, M.; Chanana, M.; König, T.; Kuttner, C.; Fery, A. Optically Anisotropic Substrates via Wrinkle-Assisted Convective Assembly of Gold Nanorods on Macroscopic Areas. *Faraday Discuss.* **2014**, *49* (0), 1–18.
- (148) Nandan, B.; Bhoje Gowd, E.; Bigall, N. C.; Eychmüller, A.; Formanek, P.; Simon, P.; Stamm, M. Arrays of Inorganic Nanodots and Nanowires Using Nanotemplates Based on Switchable Block Copolymer Supramolecular Assemblies. *Adv. Funct. Mater.* **2009**, *19* (17), 2805–2811.
- (149) Bhoje Gowd, E.; Nandan, B.; Vyas, M. K.; Bigall, N. C.; Eychmüller, A.; Schlörb, H.; Stamm, M. Highly Ordered Palladium Nanodots and Nanowires from Switchable Block Copolymer Thin Films. *Nanotechnology* **2009**, *20* (41), 415302.
- (150) Son, J. G.; Bae, W. K.; Kang, K. H.; Nealey, P. F.; Char, K. Placement Control of Nanomaterial Block Copolymer Thin Films. *ACS Nano* **2009**, *3* (12), 3927–3934.
- (151) Angelescu, D. E.; Waller, J. H.; Register, R. A.; Chaikin, P. M. Shear-Induced Alignment in Thin Films of Spherical Nanodomains. *Adv. Mater.* **2005**, *17* (15), 1878–1881.
- (152) Kim, S. Y.; Gwyther, J.; Manners, I.; Chaikin, P. M.; Register, R. A. Metal-Containing Block Copolymer Thin Films Yield Wire Grid Polarizers with High Aspect Ratio. *Adv. Mater.* **2014**, *26* (5), 791–795.
- (153) Zhang, X.; Harris, K. D.; Wu, N. L. Y.; Murphy, J. N.; Buriak, J. M. Fast Assembly of Ordered Block Microwave Annealing. **2010**, *4* (11), 7021–7029.
- (154) Singh, G.; Yager, K. G.; Berry, B.; Kim, H. C.; Karim, A. Dynamic Thermal Field-Induced Gradient Soft-Shear for Highly Oriented Block Copolymer Thin Films. *ACS Nano* **2012**, *6* (11), 10335–10342.
- (155) Luo, M.; Scott, D. M.; Epps, T. H. Writing Highly Ordered Macroscopic Patterns in Cylindrical Block Polymer Thin Films via Raster Solvent Vapor Annealing and Soft Shear. *ACS Macro Lett.* **2015**, *4* (5), 516–520.
- (156) Majewski, P. W.; Rahman, A.; Black, C. T.; Yager, K. G. Arbitrary Lattice Symmetries via Block Copolymer Nanomeshes. *Nat. Commun.* **2015**, *6* (May), 7448.
- (157) *Polymer Handbook*, 4th ed.; Brandrup, J.; Immergut, E. H.; Grulke, E. A.; Abe, A.; Bloch, D. R., Ed.; Wiley: New York, 1999.
- (158) Wang, Y.; Li, F. An Emerging Pore-Making Strategy: Confined Swelling-Induced Pore Generation in Block Copolymer Materials. *Adv. Mater.* **2011**, *23* (19), 2134–2148.

- (159) Chai, J.; Wang, D.; Fan, X. N.; Buriak, J. M. Assembly of Aligned Linear Metallic Patterns on Silicon. *Nat. Nanotechnol.* **2007**, *2* (8), 500–506.
- (160) Quere, D.; di Meglio, J.-M.; Brochard-Wyart, F. Spreading of Liquids on Highly Curved Surfaces. *Science* (80-. ). **1990**, *249* (4974), 1256–1260.
- (161) Yin, J.; Yao, X.; Liou, J.-Y. Y.; Sun, W.; Sun, Y.-S. Sen; Wang, Y. Membranes with Highly Ordered Straight Nanopores by Selective Swelling of Fast Perpendicularly Aligned Block Copolymers. *ACS Nano* **2013**, *7* (11), 9961–9974.
- (162) Chen, Z.; He, C.; Li, F.; Tong, L.; Liao, X.; Wang, Y. Responsive Micellar Films of Amphiphilic Block Copolymer Micelles: Control on Micelle Opening and Closing. *Langmuir* **2010**, *26* (11), 8869–8874.
- (163) Shultz, M. J.; Vu, T. H. Hydrogen Bonding between Water and Tetrahydrofuran Relevant to Clathrate Formation. *J. Phys. Chem. B* **2015**, *119* (29), 9167–9172.
- (164) Albert, J. N. L.; Epps, T. H. Self-Assembly of Block Copolymer Thin Films. *Mater. Today* **2010**, *13* (6), 24–33.
- (165) Arichi, S.; Matsuura, H. Studies of Poly-2-Vinylpyridine. II. Solubilities in Various Solvents. *Bull. Chem. Soc. Jpn.* **1966**, *251* (1950), 434–439.
- (166) Riddick, J. A.; Bunger, W. B.; Sakano, T. K. *Organic Solvents: Physical Properties and Methods of Purification*; Techniques of Chemistry; Wiley, 1986.
- (167) Serjeant, E. P.; Dempsey, B.; of Pure, I. U.; on Electrochemical Data, A. C. C. *Ionisation Constants of Organic Acids in Aqueous Solution*; IUPAC chemical data series; Pergamon Press, 1979.
- (168) Tantavichet, N.; Pritzker, M. D.; Burns, C. M. Proton Uptake by poly(2-Vinylpyridine) Coatings. *J. Appl. Polym. Sci.* **2001**, *81* (6), 1493–1497.
- (169) Pujari, S.; Keaton, M. a.; Chaikin, P. M.; Register, R. a. Alignment of Perpendicular Lamellae in Block Copolymer Thin Films by Shearing. *Soft Matter* **2012**, *8* (19), 5358.
- (170) Kauranen, M.; Zayats, A. V. Nonlinear Plasmonics. *Nat Phot.* **2012**, *6* (11), 737–748.
- (171) Butet, J.; Brevet, P.-F.; Martin, O. J. F. Optical Second Harmonic Generation in Plasmonic Nanostructures: From Fundamental Principles to Advanced Applications. *ACS Nano* **2015**, *9* (11), 10545–10562.
- (172) Aouani, H.; Rahmani, M.; Navarro-Cía, M.; Maier, S. a. Third-Harmonic-Upconversion Enhancement from a Single Semiconductor Nanoparticle Coupled to a Plasmonic Antenna. *Nat. Nanotechnol.* **2014**, *9* (4), 290–294.
- (173) Liu, S.-D.; Leong, E. S. P.; Li, G.-C.; Hou, Y.; Deng, J.; Teng, J. H.; Ong, H. C.; Lei, D. Y. Polarization-Independent Multiple Fano Resonances in Plasmonic Nonamers for Multimode-Matching Enhanced Multiband Second-Harmonic Generation. *ACS Nano* **2016**, *10* (1), 1442–1453.
- (174) Hubert, C.; Billot, L.; Adam, P. M.; Bachelot, R.; Royer, P.; Grand, J.; Gindre, D.; Dorkenoo, K. D.; Fort, A. Role of Surface Plasmon in Second Harmonic Generation from

- Gold Nanorods. *Appl. Phys. Lett.* **2007**, *90* (18), 88–91.
- (175) Yu, N.; Genevet, P.; Kats, M. a; Aieta, F.; Tetteien, J.-P.; Capasso, F.; Gaburro, Z. Light Propagation with Phase Discontinuities Reflection and Refraction. *Science* (80-. ). **2011**, *334* (October), 333–337.
- (176) Biswas, S.; Liu, X.; Jarrett, J. W.; Brown, D.; Pustovit, V.; Urbas, A.; Kenneth L. Knappenberger, J.; Nealey, P. F.; Vaia, R. A.; Knappenberger, K. L.; Nealey, P. F.; Vaia, R. A. Nonlinear Chiro-Optical Amplification by Plasmonic Nanolens Arrays Formed via Directed Assembly of Gold Nanoparticles. *Nano Lett.* **2015**, *15* (3), 1836–1842.
- (177) Liu, X.; Biswas, S.; Jarrett, J. W.; Poutrina, E.; Urbas, A.; Knappenberger, K. L.; Vaia, R. A.; Nealey, P. F. Deterministic Construction of Plasmonic Heterostructures in Well-Organized Arrays for Nanophotonic Materials. *Adv. Mater.* **2015**, *27* (45), 7314–7319.
- (178) Jarrett, J. W.; Zhao, T.; Johnson, J. S.; Liu, X.; Nealey, P. F.; Vaia, R. A.; Knappenberger, K. L. Plasmon-Mediated Two-Photon Photoluminescence-Detected Circular Dichroism in Gold Nanosphere Assemblies. *J. Phys. Chem. Lett.* **2016**, *7* (5), 765–770.
- (179) Li, H.; Xia, H.; Wang, D.; Tao, X. Simple Synthesis of Monodisperse, Quasi-Spherical, Citrate-Stabilized Silver Nanocrystals in Water. *Langmuir* **2013**, *29* (16), 5074–5079.
- (180) Li, Q.; Zhuo, X.; Li, S.; Ruan, Q.; Xu, Q. H.; Wang, J. Production of Monodisperse Gold Nanobipyramids with Number Percentages Approaching 100% and Evaluation of Their Plasmonic Properties. *Adv. Opt. Mater.* **2015**, *3* (6), 801–812.
- (181) Park, K.; Koerner, H.; Vaia, R. A. Depletion-Induced Shape and Size Selection of Gold Nanoparticles. *Nano Lett.* **2010**, *10* (4), 1433–1439.
- (182) Tabor, C.; Murali, R.; Mahmoud; El-Sayed, M. A. On the Use of Plasmonic Nanoparticle Pairs as a Plasmon Ruler: The Dependence of the near-Field Dipole Plasmon Coupling on Nanoparticle Size and Shape. *J. Phys. Chem. A* **2009**, *113* (10), 1946–1953.
- (183) Egerton, R. F.; Li, P.; Malac, M. Radiation Damage in the TEM and SEM. *Micron* **2004**, *35* (6), 399–409.
- (184) Nepal, D.; Drummy, L. F.; Biswas, S.; Park, K.; Vaia, R. A. Large Scale Solution Assembly of Quantum Dot-Gold Nanorod Architectures with Plasmon Enhanced Fluorescence. *ACS Nano* **2013**, *7* (10), 9064–9074.
- (185) Liu, X.; Yue, Q.; Yan, T.; Li, J.; Yan, W.; Ma, J.; Zhao, C.; Zhang, X. Competition between Local Field Enhancement and Nonradiative Resonant Energy Transfer in the Linear Absorption of a Semiconductor Quantum Dot Coupled to a Metal Nanoparticle. *J. Phys. Chem. C* **2016**, *120* (32), 18220–18227.
- (186) Hoang, T. B.; Akselrod, G. M.; Mikkelsen, M. H. Ultrafast Room-Temperature Single Photon Emission from Quantum Dots Coupled to Plasmonic Nanocavities. *Nano Lett.* **2016**, *16* (1), 270–275.
- (187) Smith, D. R.; Mikkelsen, M. H. Control of Radiative Processes Using Tunable Plasmonic Nanopatch Antennas. *Nano Lett.* **2014**, *14*, 4797.

- (188) Akselrod, G. M.; Argyropoulos, C.; Hoang, T. B.; Ciraci, C.; Fang, C.; Huang, J.; Smith, D. R.; Mikkelsen, M. H. Probing the Mechanisms of Large Purcell Enhancement in Plasmonic Nanoantennas. *Nat. Photonics* **2014**, *8* (11), 835–840.
- (189) Kulakovich, O.; Strekal, N.; Yaroshevich, A.; Maskevich, S.; Gaponenko, S.; Nabiev, I.; Woggon, U.; Artemyev, M. Enhanced Luminescence of CdSe Quantum Dots on Gold Colloids. *Nano Lett.* **2002**, *2* (12), 1449–1452.
- (190) Cohen-Hoshen, E.; Bryant, G. W.; Pinkas, I.; Sperling, J.; Bar-Joseph, I. Exciton-Plasmon Interactions in Quantum Dot-Gold Nanoparticle Structures. *Nano Lett.* **2012**.
- (191) Reineck, P.; Gómez, D.; Ng, S. H.; Karg, M.; Bell, T.; Mulvaney, P.; Bach, U. Distance and Wavelength Dependent Quenching of Molecular Fluorescence by Au@SiO<sub>2</sub> Core-Shell Nanoparticles. *ACS Nano* **2013**, *7* (8), 6636–6648.
- (192) Abadeer, N. S.; Brennan, M. R.; Wilson, W. L.; Murphy, C. J. Distance and Plasmon Wavelength Dependent Fluorescence of Molecules Bound to Silica-Coated Gold Nanorods. *ACS Nano* **2014**, *8* (8), 8392–8406.
- (193) Viste, P.; Plain, J.; Jaffiol, R.; Vial, A.; Adam, P. M.; Royer, P. Enhancement and Quenching Regimes in Metal-Semiconductor Hybrid Optical Nanosources. *ACS Nano* **2010**, *4* (2), 759–764.
- (194) Pompa, P. P.; Martiradonna, L.; Torre, a Della; Sala, F. Della; Manna, L.; De Vittorio, M.; Calabi, F.; Cingolani, R.; Rinaldi, R. Metal-Enhanced Fluorescence of Colloidal Nanocrystals with Nanoscale Control. *Nat. Nanotechnol.* **2006**, *1* (2), 126–130.
- (195) Kinkhabwala, A.; Yu, Z.; Fan, S.; Avlasevich, Y.; Müllen, K.; Moerner, W. E. Large Single-Molecule Fluorescence Enhancements Produced by a Bowtie Nanoantenna. *Nat. Photonics* **2009**, *3* (11), 654–657.
- (196) Khatua, S.; Paulo, P. M. R.; Yuan, H.; Gupta, A.; Zijlstra, P.; Orrit, M. Resonant Plasmonic Enhancement of Single-Molecule Fluorescence by Individual Gold Nanorods. *ACS Nano* **2014**, *8* (5), 4440–4449.
- (197) Gueroui, Z.; Libchaber, A. Single-Molecule Measurements of Gold-Quenched Quantum Dots. *Phys. Rev. Lett.* **2004**, *93* (16), 1–4.
- (198) Xue, C.; Xue, Y.; Dai, L.; Urbas, A.; Li, Q. Size- and Shape-Dependent Fluorescence Quenching of Gold Nanoparticles on Perylene Dye. *Adv. Opt. Mater.* **2013**, *1* (8), 581–587.
- (199) Chen, G.; Liu, D.; He, C.; Gannett, T. R.; Lin, W.; Weizmann, Y. Enzymatic Synthesis of Periodic DNA Nanoribbons for Intracellular pH Sensing and Gene Silencing. *J. Am. Chem. Soc.* **2015**, *137* (11), 3844–3851.
- (200) Zhang, C.; Macfarlane, R. J.; Young, K. L.; Choi, C. H. J.; Hao, L.; Auyeung, E.; Liu, G.; Zhou, X.; Mirkin, C. A. A General Approach to DNA-Programmable Atom Equivalents. *Nat Mater* **2013**, *12* (8), 741–746.
- (201) Qin, W.; Liu, H.; Guyot-Sionnest, P. Small Bright Charged Colloidal Quantum Dots. *ACS Nano* **2014**, *8* (1), 283–291.

- (202) Pons, T.; Pic, E.; Lequeux, N.; Cassette, E.; Bezdetnaya, L.; Guillemin, F.; Marchal, F.; Dubertret, B. Cadmium-Free CuInS<sub>2</sub>/ZnS Quantum Dots for Sentinel Lymph Node Imaging with Reduced Toxicity. *ACS Nano* **2010**, *4* (5), 2531–2538.
- (203) Peterson, J. J.; Krauss, T. D. Fluorescence Spectroscopy of Single Lead Sulfide Quantum Dots. *Nano Lett.* **2006**, *6* (3), 510–514.
- (204) Kim, S.; Fisher, B.; Eisler, H. J.; Bawendi, M. Type-II Quantum Dots: CdTe/CdSe(core/shell) and CdSe/ZnTe(core/shell) Heterostructures. *J. Am. Chem. Soc.* **2003**, *125* (38), 11466–11467.
- (205) Tyrakowski, C. M.; Shamirian, A.; Rowland, C. E.; Shen, H.; Das, A.; Schaller, R. D.; Snee, P. T. Bright Type II Quantum Dots. *Chem. Mater.* **2015**, *27* (21), 7276–7281.
- (206) Hohng, S.; Ha, T. Near-Complete Suppression of Quantum Dot Blinking in Ambient Conditions. *J. Am. Chem. Soc.* **2004**, *126* (5), 1324–1325.
- (207) Munro, A. M.; Ginger, D. S. Photoluminescence Quenching of Single CdSe Nanocrystals by Ligand Adsorption. *Nano Lett.* **2008**, *8* (8), 2585–2590.
- (208) Lingley, Z.; Lu, S.; Madhukar, A. A High Quantum Efficiency Preserving Approach to Ligand Exchange on Lead Sulfide Quantum Dots and Interdot Resonant Energy Transfer. *Nano Lett.* **2011**, *11*, 2887–2891.
- (209) Wyckoff, R. W. G. *Crystal Structures*, 2nd ed.; Wiley: New York, 1963.
- (210) DeVries, G. A.; Brunnbauer, M.; Hu, Y.; Jackson, A. M.; Long, B.; Neltner, B. T.; Uzun, O.; Wunsch, B. H.; Stellacci, F. Divalent Metal Nanoparticles. *Science* (80-. ). **2007**, *315* (5810), 358 LP-361.
- (211) Hermanson, G. T. Chapter 1 - Introduction to Bioconjugation BT - Bioconjugate Techniques (Third Edition); Academic Press: Boston, 2013; pp 351–386.
- (212) Park, N. G. Perovskite Solar Cells: An Emerging Photovoltaic Technology. *Mater. Today* **2015**, *18* (2), 65–72.
- (213) Schmidt, L. C.; Pertegas, A.; Gonzalez-Carrero, S.; Malinkiewicz, O.; Agouram, S.; Espallargas, G. M.; Bolink, H. J.; Galian, R. E.; Perez-Prieto, J. Nontemplate Synthesis of CH<sub>3</sub>NH<sub>3</sub>PbBr<sub>3</sub> Perovskite Nanoparticles. *J. Am. Chem. Soc.* **2014**, *136*, 850–853.
- (214) Protesescu, L.; Yakunin, S.; Bodnarchuk, M. I.; Krieg, F.; Caputo, R.; Hendon, C. H.; Yang, R. X.; Walsh, A.; Kovalenko, M. V. Nanocrystals of Cesium Lead Halide Perovskites (CsPbX<sub>3</sub>, X = Cl, Br, and I): Novel Optoelectronic Materials Showing Bright Emission with Wide Color Gamut. *Nano Lett.* **2015**, *15* (6), 3692–3696.
- (215) Kovalenko, M. V. Opportunities and Challenges for Quantum Dot Photovoltaics. *Nat. Nanotechnol.* **2015**, *10* (12), 994–997.
- (216) Luo, B.; Pu, Y. C.; Lindley, S. A.; Yang, Y.; Lu, L.; Li, Y.; Li, X.; Zhang, J. Z. Organolead Halide Perovskite Nanocrystals: Branched Capping Ligands Control Crystal Size and Stability. *Angew. Chemie - Int. Ed.* **2016**, *55* (31), 8864–8868.
- (217) Marbella, L. E.; Millstone, J. E. NMR Techniques for Noble Metal Nanoparticles. *Chem.*

*Mater.* **2015**, *27* (8), 2721–2739.

- (218) Zherebetsky, D.; Scheele, M.; Zhang, Y.; Bronstein, N.; Thompson, C.; Britt, D.; Salmeron, M.; Alivisatos, P.; Wang, L.-W. Hydroxylation of the Surface of PbS Nanocrystals Passivated with Oleic Acid. *Sci.* **2014**, *344* (6190), 1380–1384.
- (219) Piveteau, L.; Ong, T.-C.; Rossini, A. J.; Emsley, L.; Copéret, C.; Kovalenko, M. V. Structure of Colloidal Quantum Dots from Dynamic Nuclear Polarization Surface Enhanced NMR Spectroscopy. *J. Am. Chem. Soc.* **2015**, *137* (43), 13964–13971.
- (220) Zhuo, X.; Zhu, X.; Li, Q.; Yang, Z.; Wang, J. Gold Nanobipyramid-Directed Growth of Length-Variable Silver Nanorods with Multipolar Plasmon Resonances. *ACS Nano* **2015**, *9* (7), 7523–7535.
- (221) Zhu, X. Z.; Zhuo, X.; Li, Q.; Yang, Z.; Wang, J. F. Gold Nanobipyramid-Supported Silver Nanostructures with Narrow Plasmon Linewidths and Improved Chemical Stability. *Adv. Funct. Mater.* **2016**, *26* (3), 341–352.
- (222) Guo, X.; Zhang, Q.; Sun, Y.; Zhao, Q.; Yang, J. Lateral Etching of Core–Shell Au@Metal Nanorods to Metal-Tipped Au Nanorods with Improved Catalytic Activity. *ACS Nano* **2012**, *6* (2), 1165–1175.
- (223) Pellegrotti, J. V.; Acuna, G. P.; Puchkova, A.; Holzmeister, P.; Gietl, A.; Lalkens, B.; Stefani, F. D.; Tinnefeld, P. Controlled Reduction of Photobleaching in DNA Origami-Gold Nanoparticle Hybrids. *Nano Lett.* **2014**, *14* (5), 2831–2836.